E 3/90

An Optical Study of the Flow Start-Up Process in Four Convergent-Divergent Nozzles

Heinz Reichenbach , EMI

Klaus O. Opalka , BRL

Fraunhofer-Gesellschaft

E 3/90

An Optical Study of the Flow Start-Up Process in Four Convergent-Divergent Nozzles

Heinz Reichenbach , EMI
Klaus O. Opalka, BRL

March 1990

Research Contract # DAJA45-89-C-0019

TABLE OF CONTENTS

LIST OF ILLUSTRATIONS

1. INTRODUCTION

Large blast simulators (LBS) are specialized shock tunnels for generating decaying blast waves such as are associated with nuclear explosions. Blast Simulators employ convergent-divergent nozzles at the driver exit to retard the outflow of the high-pressure driver gas and generate long flow durations. It is known that the gas behind a shock traveling down a shock tunnel can be expanded to high flow Mach numbers by passing it through convergent-divergent nozzles. Such convergent-divergent nozzles have been extensively investigated, both in theory and experiment, and a summary of these efforts is presented, e. g., in Reference 1.* However, in all of these studies the diaphragm which separates the high-pressure from the low-pressure region, was located upstream of the nozzle under investigation so that a well formed shock entered the nozzle from the upstream side. The LBS nozzle design differs from the nozzle design used in previous studies in that it has the flow-initiating diaphragm mounted in the throat of the nozzle itself. When the diaphragm is ruptured, a shock forms and travels downstream into the divergent section, while a rarefaction fan travels upstream into the convergent section. No previous experimental research is known for this problem.

Therefore, a shock tube test was proposed in which the diaphragm separating the high-pressure driver from the low-pressure driven section was mounted in the throat of a convergent-divergent nozzle which formed the transition from the driver to the driven section of the shock tube. The diaphragm was located at the upstream edge of the viewing window of high-quality optical glas through wich shadowgraph and schlieren records could be taken. The optical measurements were supplemented by measurements of the static pressure at three locations downstream from the nozzles. The objectives of this investigation were (a) to obtain optical records of the shock formation in the convergent-divergent nozzle immediately after rupturing the diaphragm, (b) to determine the influence of the cone angle and length of a divergent nozzle on the pressure signature in the expansion region behind the nozzle and (c) to facilitate comparisons with one-, and two-dimensional hydrocode computations. The test set-up and the results of this experimental study are presented in this report and the most significant findings are discussed.

References are listed at the end of the report.

2. BACKGROUND

The U.S. Army has proposed the construction of a test facility for simulating ideal blast waves, large enough to test full-sized military equipment in order to meet its growing need for blast and thermal survivability testing. The US Army Ballistic Research Laboratory (BRL) was assigned the lead role in the R&D of this project. Subsequently, the BRL developed a concept of such a facility, referred to as large-scale blast and thermal simulator (LB/TS), over the past eight years. The proposed U.S. LB/TS is suitable to simulate both thermal and blast effects of nuclear explosions over a wide variety of shock overpressures and weapon yields without generating nuclear radiation effects. The simulator would be used to conduct blast and thermal survivability testing on full-scale military equipment, like trucks and helicopters, and to perform research into nuclear blast phenomenology.

2.1 LB/TS Concept.

A large-scale blast and thermal simulator is basically a shock tunnel whose cross-sectional area varies along its length. Straight shock tubes do not produce the flow durations which are observed in decaying blast waves. To obtain long flow durations comparable to those of decaying blast waves the outflow of the driver gas has to be retarded. This is effected by converging the flow area at the exit of the driver, so that the driver takes the shape of a bottle. Furthermore, a single driver is technically impractical because of the size of the facility and the required supply pressures in the driver. A number of smaller drivers has to be employed to accomodate the necessary initial test conditions.

The U.S. LB/TS concept is described in detail in the References[2-4] and illustrated in Figure 1. Blast waves will be simulated by releasing compressed gas from several high-pressure steel driver tubes into a large expansion tunnel constructed of prestressed concrete. The gas exits the drivers through convergent-divergent nozzles. Diaphragms are mounted in the throats of these nozzles (the bottle neck). The thermal simulation will be effected through aluminum/oxygen combustion near the target. The test section for the targets is located in the expansion tunnel, about seven diameters downstream from the exit of the driver nozzles. The test section has a semi-circular cross-section with a 10m radius. This size is deemed necessary to avoid blocking of the flow about the target.

2.2 LB/TS Design Studies.

The BRL-Q1D code[5] was used to perform computational studies for determining the design parameters of the projected facility. Parametric studies were initiated to answer questions about the necessary size and the expected performance of such a facility simulating the required range of blast waves. The scope of the computational studies encompassed pressure ratios from 4 to 200 across the diaphragm for unheated driver gas (T_4 = 288.15 K and γ = 1.4) in association with the operating envelope for the planned U.S. LB/TS. Standard atmopsheric conditions were assumed as ambient and in the expansion tunnel (1) for all computational simulations. Table I presents the test conditions which were selected for the parametric BRL-Q1D computations. From the initial test conditions, the simulated blast wave in the test section of the LB/TS expansion tunnel was defined with reference to shock strength, duration and static and dynamic impulse. For the pupose of this study, the initial throat shock P_{Ts} was determined by iteratively solving the basic shock tube equation, $P_4/P_1 = f\,(P_{T2}/P_1)$.

TABLE I. LB/TS INITIAL TEST CONDITIONS
P_1 = 101.325 kPa; T_1 = 288.15 K

TEST SECTION							
p_s, psi	2.0	5.0	10.0	15.0	20.0	25.0	35.0
p_s, kPa	13.79	34.47	68.95	103.4	137.9	172.4	241.3
DRIVER							
P_4/P_1	4	14	38	55	80	110	188
P_4, MPa	0.4053	1.419	3.850	5.573	8.106	11.145	19.050
THROAT							
P_{T2}/P_1	1.929	3.256	4.689	5.288	5.974	6.575	7.652
p_{Ts}, kPa	94.11	228.6	373.8	434.5	504.4	565.0	674.0

Initially, the U.S. design studies were based on the Large Blast Simulator (LBS) at the Centre d'Etudes de Gramat (CEG), France. However, it soon became clear that a much larger facility was needed in order to accommodate the full range of anticipated targets. A broader range of shock overpressures and weapon yields was required to cover the test conditions specified in the operating envelope. The results of our computational studies with the BRL-Q1D code show that a full-scale blast/thermal simulation facility can be designed and that driver heating, an active RWE, and computer-controlled throat

valves should be used to optimize control and operation of the facility.

Experimental efforts were initiated at the same time, but test results became available only much later because the construction of the model facility consumed much time. To date, small-scale experiments with heated driver gas have been completed, and the results have been used to validate the computational results. Small-scale RWE and throat-valve models are being built for the experimental validation of the computational predictions. Also, a 1/6-scale test bed using a throat valve and an active RWE is in the design stage and, when built, will be used for validating the concepts to be used in the full-scale U.S. LB/TS design. Some questions remain, however, about the usefulness of divergent nozzles which are used, e.g., in the LBS at the CEG in France.

2.3 Nozzle Flow Phenomena.

The drivers of the planned U.S. LB/TS as well as of the French LBS facility have the diaphragm which separates the high-pressure from the low-pressure region mounted in the throat of a convergent-divergent nozzle. When the diaphragm is ruptured, a shock travels downstream into the divergent section, while a rarefaction fan travels upstream into the convergent section. The time from the rupturing of the diaphragm to the establishment of a quasisteady flow pattern in the nozzle is defined as the starting process of the nozzle. No previous experimental research is known for either the starting process, or the quasisteady flow phase.

The CEG-LBS nozzles seem to present certain problems. Figure 2 presents an experimental and a computational pressure history of a 42 kPa/10 kT blast wave. It is argued that the pressure spike that appears at the front of the blast wave in the experimental as well as in the computational pressure history is caused by the divergent nozzles. This argument is supported by computational results[2] which indicate that the greater the cone half angle of the divergent nozzle, the smaller is the spike at the shock front. It is argued also that the divergent nozzles increase the thrust of the rocket motor which is formed by the driver-nozzle combination, on the reaction pier. Therefore, eliminating the divergent nozzles would have a double advantage on the design and the performance of the U.S. LB/TS reducing the thrust on the pier as the drivers empty, as well as eliminating the spike at the front of the simulated blast wave.

On the other hand, results of small-scale pilot experiments seem to indicate that there are pressure losses connected with the introduction of a large area discontinuity at the exit of the nozzle throat which are lessened when divergent nozzles are used. Therefore, the use of divergent nozzles cannot be easily dismissed. However, if divergent nozzles are included in the US LB/TS design the nozzle length becomes a critical material parameter which itself depends of the cone half angle chosen for the nozzle design. Amann has shown in his experiments[1] that the start-up time is shortest when the cone half angle of the divergent nozzle is largest, however his research was limited to cone half angles of 5° - 15° and it is not known whether the trend continues at the higher angles. Information is also needed on the effect of the cone half angle on the established flow after the start-up is completed.

The BRL 1D-, and 2D-flow computations agree with earlier theoretical and experimental research that a recompression shock forms in the nozzles and either stays there for moderate diaphragm pressure ratios, or is swept down the expansion tunnel for diaphragm pressure ratios above 40. An experimental comparison is needed for these computations which illustrates the flow formation process and shows the pressure and density distribution in the nozzle. It is expected that the present experimental effort would be somewhat analogous to the work done in Reference 1, although it is neither expected to yield identical results nor to answer all the questions posed.

3. EXPERIMENTAL APPARATUS

The experimental apparatus at the EMI consists of a shock tube which was specially modified for use in this study, a 24-spark Cranz-Schardin camera and shadowgraph arrangement and electronic control and recording equipment.

3.1 EMI Shock Tube

The existing EMI shock tube has a circular cross-section with an inner diameter of 20 cm in its most used configuration. The driver section is 180 cm long, the driven section measures 888 cm (Figure 3). Cellulose Acetate sheets (Ultraphan) have proven to be a good diaphragm material because it becomes brittle when it is stretched and has a high breaking velocity. The shock tube has a rectangular test chamber with a cross-section of 40 mm x 110 mm located 721 cm downstream from the driver section. The test chamber is followed by a 157 cm long extension to the closed end. The side walls of the test

chamber are formed by plane parallel windows (200 mm x 110 mm) of high quality optical glass to facilitate optical investigations of the shock wave propagation (Figure 4). An inlet channel of the same shape and cross-section as the test chamber and formed of polished aluminum plates protrudes upstream into the axisymmetric driven section. A rectangular section is cut out of the arriving shock wave of circular shape by the sharp inlet edges of the channel walls (cooky cutter principle).

The existing shock tube had to be modified in order to carry out the special task presented by this project. The modifications include a new driver pressure chamber which could be mounted inside the inlet channel and the various model parts for the divergent nozzles. The new driver pressure chamber includes the convergent section and that part of the throat of the nozzle which lies upstream of the diaphragm (Figure 5). The inner cross-section of the driver is 64 mm x 30 mm; it converges to a cross-section of 16 mm x 30 mm at the diaphragm. The length of the driver pressure chamber was chosen to 1000 mm in order to delay the arrival of reflections from the end wall. The diaphragms are composed of two Ultraphan sheets, each 0.1 mm thick, with an ignition wire of 0.08 mm diameter sandwiched in between them. With this construct, the diaphragm can be bursted at an exactly predetermined moment in time by exploding the wire with an electric impulse. The diaphragm section is shown in Figure 6a.

The test objectives require to locate and mount the diaphragm in, or near, the test section window of our shock tube in such a way that the view of the downstream region of the throat and divergent nozzle is only minimally obstructed. The lengths of the various divergent nozzle configurations make it necessary to relocate the models in the test section window so that optical records may be taken of all waves of interest from one to three diameters downstream from the diaphragm. This requirement makes it necessary to locate the diaphragm either at, or at a multiple of 1 to 3 times one half of the window length (100 mm) upstream from, the left edge of the test section window. These window locations are labeled B, C and D in Figure 5. The location A was not used in this experimental effort.

3.2 Nozzle Configurations

Four divergent-nozzle models were fabricated, differing in the lay-out of the divergent section as shown in Figure 5. All dimensions are scaled proportionately to the area ratios of the convergent-divergent nozzles used in the French LBS. The four nozzle configurations are characterized as follows.

a) A convergent-divergent nozzle with the area and length ratios and the cone half angle of the nozzles used in the CEG-LBS (Inserts 1, 2 and 5).

b) An extended convergent-divergent nozzle with the area and length ratios of the Q1D-computational CEG-LBS model, i.e., the 7 CEC-LBS nozzles combined into one nozzle. The divergent section has a cone half angle of 16° and its length is extended to the full height of the expansion tunnel (Inserts 1,2 and 4).

c) An extended convergent-divergent nozzle with a divergent 45° cone half angle. The divergent nozzle extends to the full height of the expansion tunnel (Insert 1,2 and 3).

d) A convergent nozzle and throat section with the area ratios of the CEG-LBS but without the divergent section, also referred to as the 90° divergent nozzle (Inserts 1 and 2).

Pictures of the divergent nozzle models are shown in Figures 6b thru 6e.

3.3 Instrumentation

A 24-frame Cranz-Schardin spark camera and shadow/schlieren system was the principal tool for the optical study (Figure 7). The sparks from 24 point sources are focussed onto 24 objective lenses of the camera by means of a concave mirror. At the moment a spark is generated, it is projected onto the film through the very objective lense onto which the image of the spark was copied. The advantage of this procedure is that there are no moving parts aligning the path of the light rays. Therefore, the optical resolution is determined essentially by the aperture of the objective lenses. Parallax may present a disadvantage in some cases. However, the effect of parallax is minimal in the present set-up where a concave mirror with a long focal length (f = 350 cm) is used in conjunction with a test section of shallow depth (4 cm).

The shadow method is well suited for the visualization of shock waves. For this method to work well, a point source of light is required. In our case, the light source has a diameter of less than 1 mm. Furthermore, the objective lenses are not focussed on the center plane of the test chamber but on a reference plane typically at a distance of 40 cm from the center plane of the test chamber. The density gradients in the flow are made visible by the schlieren method. The Toepler structure using sharp knife edges was found to yield the best results. In the following experiments, both methods

were combined and in this way, clear images were obtained of the shock waves as well as of the density gradients.

Other equipment used included the trigger gauges and electronic delay units for the timing of the Cranz-Schardin camera and several 12-bit transient recorders. Kistler quarz pressure gages of type 603B were used to sense the static pressure. They have a characteristic frequency response of approximately 500 kHz. Electrical filters with a maximum frequency response of 180 kHz were installed between the pressure gauge and the charge amplifier in order to prevent an overshoot of the signal.

3.4 Test Conditions and Procedure

The four model configurations were tested at seven driver pressure levels, namely at P_{41} = 4, 14, 38, 55, 80, 110 and 188. To test the functionality of the modified shock tube and to get a feel for the starting process of the various nozzles, the models were tested at the lowest specified driver pressure level (P_{41}=4) first. Tests then continued with the next highest driver pressure level (P_{41}=14). The test was prepared by mounting the desired model configuration and the diaphragm. The shock tube was then closed, the Cranz-Schardin camera and the pressure recorders were readied and all electrical connections were tested. The firing and recording controls were activated in the darkened room, and the recording film holder was opened before the driver was pressurized. The specified operating pressure was 1300 kPa (13 bar) over atmospheric pressure, except for the lowest driver pressure ratio where the driver pressure was 300 kPa (3 bars) over atmospheric pressure. Then the driven section was evacuated as necessary until the desired driver pressure ratio was established.

The rupturing of the diaphragm was initiated with an electric pulse of 10-20 kV to explode the wire embedded between the two Ultraphan layers. The same pulse triggered the camera and the other recording equipment after some preset delay time. The principle of the electronic control circuit for the experimental process can be seen in Figure 8. The preset delay time between the ignition pulse and the first spark pulse to the Cranz-Schardin camera was measured by a time counter. Some interference from the strong trigger pulse was suffered on the recording equipment and a few pressure records were lost. A test log was kept to record the initial test and ambient conditions, including the trigger times and the spark frequency for the Cranz-Schardin camera and for the pressure recorders. The delay time between the bursting of the diaphragm and the first spark of the camera was additionally measured by a time counter.

4. EXPERIMENTAL RESULTS AND DISCUSSION

With each test shot, twenty-four shadowgraphs or schlieren pictures were recorded on film by the Cranz-Schardin camera at constant time intervals. The time intervals were estimated from the expected shock and particle velocities based on an analytical solution of the shock tube problem applied to the throat channel of the nozzles for each of the specified driver-pressure ratios, and bracketed by the associated sound velocity expected in the expansion tunnel downstream from the nozzles. A set of records was forwarded to the U.S. Army BRL and the evaluated optical records are presented in Appendix A.

The static pressure was recorded at three available gage locations in the tunnel ceiling, 270 mm, 760 mm and 889 mm downstream from the center of the test section window. The pressure was recorded at all seven driver-pressure ratios for the 90°, 45° and 16° divergent half nozzles in the model position B only. A set of the pressure records was forwarded to the U.S. Army BRL.

4.1 16° Divergent Half Nozzle

The 16° divergent half nozzle is suited best for an explanation of the flow start-up phenomena because the available viewing area (400 mm) is most satisfactory of all configurations. A sample sequence of shadowgraphs for the 16° divergent half nozzle at a driver-pressure ratio of 14 (Code N16/014) is shown in Figure 9. Two test shots were put together to present the whole half nozzle, shot # 13260 covers the first 200 mm (Position B) behind the diaphragm and shot # 13264 covers the range from 200-400 mm (Position C) behind the diaphragm location. The heavy vertical line halfway through the nozzle indicates that the viewing range of the two photographs needed to record the flow throughout the entire half nozzle at a particular point in time did not overlap. Flow phenomena like the incident shock, the contact surface, regions of flow separation and a system of 3 recompression shocks can be seen developing and moving past the observation area. The low pressure case was chosen because all the flow phenomena of interest remain inside the viewing area until the start-up process of the nozzle is completed.

The flow phenomena of interest were traced from the photographs and are shown in Figure 10. They are described in the following paragraphs. The **incident shock** begins to form immediately after the flow is initiated by bursting the diaphragm. Since the diaphragm breaks into fragments of uneven sizes, the opening process is

asymmetrical and causes an uneven flow progress across the height of the throat. Initially, the shock consists of a system of 2-3 curved shocks (106 μs) that reflect from the ceiling or the floor of the throat channel and gradually combine into one shock (206 μs). This formation period takes about 400 μs, by which time the shock has progressed well into the divergent section of the half nozzle (406 μs). A shock reflection is generated at the ceiling of the half nozzle exit (822 μs) which proceeds across the flow area and is itself reflected later on at the floor plate of the expansion channel.

The **contact surface** between the expanding driver gas and the gas in the low-pressure region of the divergent half nozzle follows the incident shock at close range. It can be easily detected because the associated flow turbulence it brings with it changes the background in the photographs (Figure 9). Because of the turbulence, the contact front is very rugged. Often, darker strings perpendicular to the flow direction can be detected in the turbulent region behind the contact front. It is surmised that these strings may represent compression waves which at later times are condensed into a recompression shock. Once the contact surface has entered the divergent section of the half nozzle, a variety of phenomena begin to occur simultaneously.

Throat shocks appear inside the throat channel in an interplay between boundary-layer growth and flow acceleration (406 μs and later). As many as 5 shocks have been observed temporarily. Two of these warrant special mention because of their general presence for all test conditions. The narrowest crossection exists at the diaphragm location. Once the flow reaches sonic condition in this crossection, it expands supersonically upon exiting into the throat channel and a standing X-type shock appears between 10-15 mm downstream from the diaphragm location (606 μs). A second stationary shock appears in the throat channel at about 50-60 mm downstream from the diaphragm location and remains there throughout the start-up process of the nozzle (822 μs and later).

At the exit of the throat channel, an **expansion fan** begins to develop at the corner which the throat channel forms with the divergent section (822 μs and later). Inside the divergent half nozzle, a **recompression shock** begins to form (606 μs). This shock develops into a bottle shock spawning a second shock ahead of itself (1.322 ms). The second shock develops into a bottle shock also, spawning a third shock ahead of itself in the process (1.822 ms). Extensive **flow separation regions** at both, ceiling and floor of the divergent half nozzle develop during this process. The start-up process of the nozzle comes to completion when this **system of bottle-type recompression shocks**

becomes stationary either inside the nozzle, as in the present case shown in Figures 9 and 10 (2.322 ms), or downstream from the divergent nozzle for high driver-pressure ratios, as suggested in Figures 11 and 12.

The high driver-pressure case (N16/188), shown in Figures 11 and 12 shows the same development as the low driver-pressure case except that the start-up process is accelerated and the system of bottle shocks moves out of the divergent nozzle into the expansion channel where it can no longer be observed. Because this case was photographed in a vacuum of 74 mbar, it was much more difficult to read, and the described features of the start-up process were not consistently discernible in the pictures. Also, the fragments of the diaphragm frequently obscured the picture in this case. From a comparison of the low-, and the high-pressure cases at late times it can be learned that the flow separation point moves downstream with the system of bottle shocks as the driver-pressure ratio increases and the flow separation regions get smaller.

Perhaps the biggest surprise in these photographs is the discovery of the asymmetric flow through the divergent half nozzle. It was the intention of the experimenters to obtain one half of a symmetrical flow pattern above the center axis of the nozzle. This was accomplished for the flow ahead of and up the contact surface. Behind the contact surface, however, a boundary-layer build-up along the floor plate eventually causes separation of the flow. The flow then seeks its own path by turning and more or less following the centerline of the half nozzle.

The shadowgraphs and schlieren pictures were evaluated by measuring the distances of these various flow phenomena from a reference point in the photograph with the help of a digitizing pad that was controlled by a Zenith PC. The measured distances of the flow phenomena with reference to the diaphragm location (X = 0) were then recorded as functions of time beginning with the bursting of the diaphragm (t = 0). From these records, x-t diagrams were generated on an Alliant FX/1 computer using PVI[6] software. The x-t diagrams for the two examples (N16/014 and N16/188) are shown in Figures 13. The data points for position C were matched with the data points for position B by adding a time differential to the 24 recorded spark times so that the data points for the incident shock in position C (200-400 mm) would continue on a straight line drawn through the data points for the incident shock in position B (0-200 mm).

Figure 13a presents the data for case N16/014. The distance from the diaphragm location, X, of the described flow phenomena is plotted as a function of the elapsed time from the burst of the diaphragm, t. From the diagram, one can learn that the velocities of the incident shock and of the contact surface become constant after a short acceleration period. After about 2 ms, the system of 3 bottle-type recompression shocks and the throat shocks have become stationary, also. The start-up process of the nozzle is now complete. At later times the process will reverse itself until the driver section has emptied and the pressure in the tube has equalized. Figure 13b shows that the start-up process of the nozzle in the high driver-pressure case (N16/188) is not yet complete at the time (1.07 ms) the system of recompression shocks has moved into the expansion channel downstream from the nozzle exit escaping further observation.

4.2 90° Half Nozzle

The 90° half nozzle is a nozzle without a divergent section. This configuration is especially interesting to the project engineer because the elimination of the divergent nozzles from the LB/TS design would save a great deal of material cost. An example of the flow start-up process in the 90° half nozzle is presented in Figure 14. Figure 14a shows a sequence of selected shadowgraphs for the lowest driver-pressure ratio tested, $P_{41} = 4$ (Code N90/004). The interesting phenomenon of this case is the big vortex developing to fill the big corner area behind and above the exit form the throat channel while the flow continues straight ahead in a channel the heigth of the throat along the floor of the expansion tunnel. Recompression shocks can be seen in the throat and in the flow channel behind the throat exit where the flow begins to turn.

Figure 14b shows selected shadowgraphs for the start-up process at a driver-pressure ratio of $P_{41} = 80$ (Code N90/080). The early development of a bottle shock (434 µs) seems to be disrupted by the reflection of the incident shock from the ceiling and the floor (674 µs) as well as by the passage of the diaphragm fragments (794 µs). With their disappearance from view, the system of bottle-type recompression shocks which was visible in the 16° half nozzle, has moved past the viewing area as well.

The x-t diagrams for the cases N90/004 and N90/080 are presented in Figure 15. From the x-t diagram in Figure 15a, we can deduce that the flow start-up process in the low-pressure case is complete after 2.5 ms. The x-t diagram shown in Figure 15b lets us know that the time period of the test is appropriate for the short viewing field of the test section window but does not cover the whole period of the start-up

process of the nozzle.

The most significant flow feature of the 90° half nozzle is that the flow forms its own divergent section once the local disturbances caused by the shock reflections from the ceiling and the floor have died down (Figure 14b - 914 μs). The flow expansion angle was determined by reading and averaging the maximum and minimum angles of the flow expansion fan in the shadowgraphs and schlieren pictures (e.g., Figure 14b - (1.159 μs). This flow expansion angle is plotted versus the driver-pressure ratio for the 90° half nozzle in Figure 16. It was expected that the expansion angle would monotonously increase with the driver pressure; however, Figure 16 shows a maximum for the flow expansion angle at a driver-pressure ratio of P_{41} = 110 and a slightly lesser angle at the highest driver-pressure ratio, P_{41} = 188.

4.3 45° Divergent Half Nozzle

The flow start-up process in the 45° half nozzle is illustrated in Figure 17. For this configuration, a viewing area of 300 mm was available which allowed us to observe the start-up flow phenomena for a longer period of time than for the 90° half nozzle. The shadowgraph sequence in Figure 17a shows that a recompression shock has formed at 440 μs, and a bottle shock has formed before the diaphragm fragments enter the divergent part of the half nozzle (680 μs). The throat shocks are clearly visible at 683 μs and at the later times. At 1.103 ms, the fragments disrupt the bottle shock which recovers as the fragments leave the scene (1.523 ms) and becomes stationary within the viewing area. The x-t diagram shown in Figure 17b confirms that the start-up process of the nozzle is completed at about 1.5 ms.

In the 45° divergent half nozzle, flow separation occurs at the two lowest driver-pressure levels tested, i.e., P_{41} = 4 and P_{41} = 14. At the higher driver-pressure levels, flow separation occurs early in the start-up process at the exit of the throat channel. As the start-up process continues, the separation point moves upward along the ceiling of the nozzle toward the divergent nozzle exit. At the end of the start-up process of the nozzle, the separation point becomes stationary and the flow stays attached to the ceiling of the nozzle up to this point. At the separation point near the corner of the nozzle exit, the flow separates creating a dead-water region to negotiate the corner. The flow separation angle is shown in Figure 18. The function shows a maximum for the driver-pressure ratio P_{41} = 55 and slightly smaller separation angles for the higher pressure ratios. It is noted that this is **not** the same angle as the flow expansion angle shown in Figure 16 for the 90° half nozzle.

The start-up process of the nozzle was defined in chapter 2.3 as the time from the rupturing of the diaphragm to the establishment of a quasisteady flow pattern in the nozzle. This flow start-up period could be determined from the x-t diagrams for the 45° half nozzle as a function of the driver-pressure ratio and is shown in Figure 19. For the other three nozzle configuration, the flow start-up period could not be determined because the recording-time periods of the tests were insufficient.

4.4 Pressure Records

Most of the pressure records show two, and sometimes three, shocks arriving at the gage positions, 270 mm, 860 mm and 989 mm downstream from the diaphragm location, in short succession of each other (about 10-40 microseconds apart). Pressure spikes at the shock front, as they were observed in the CEG-LBS pressure histories and in the BRL-Q1D computations, were not found in the present pressure records. This is probably due to the low area ratio of the driven section to the throat channel which is only 7.5 compared to 28 for the CEG-LBS.

Initially, the first, second and third pressure peaks were recorded with their respective arrival times at each of the three gages. The shock strength, P_{21}, was determined and plotted versus the driver-pressure ratio, P_{41}. A 2nd-degree least-squares polynomial curve fit was used to smooth the data. The comparison of the shock-strength recovery between the three half nozzles for the first and second pressure peaks proved inconclusive, however, and the plots were not included in this report. Consequently, it was decided to determine the height of the pressure plateau behind the incident shock.

The height of the pressure plateau was determined from the pressure records by inspection. This judgement proved somewhat subjective because of the considerable fluctuations of the pressure traces; however, this method was more successful. Figure 20 presents three pressure time histories for the 16° half nozzle at a low, a medium and a high driver-pressure ratio. In one third of the records the pressure plateau agreed with the first pressure peak (Figure 20b), in the second third it coincided with the second pressure peak (Figure 20a) and in the last third of the records it fell in between the two pressure peaks (Figure 20c). The pressure plateau was then nondimensionalized in the same manner as the shock peaks and plotted versus the driver-pressure ratio. As before, a 2nd-degree least-squares polynomial was fitted to the data points.

The results shown in Figure 21 indicate that a small pressure loss is associated with increasing the divergent half nozzle angle. The results for gage # 1 (Figure 21a), closest to the nozzle exits, are ambiguous, since the 45° half nozzle shows a better pressure recovery than either the 90° and the 16° half nozzles, both of which show a nearly identical pressure recovery. But at distances further away from the nozzle exits, at gages # 2 (Figure 21b) and # 3 (Figure 21c), the trend becomes better defined. The curve fits of the shock strength at gage # 2 suggest that the 16° divergent half nozzle yields an increase in the shock strength of 8.1% over the shock strength obtained without a divergent nozzle (i.e., the 90° half nozzle) at the highest driver-pressure ratio (P_{41} = 188). The results at gage # 3 seem to indicate an increase in the shock strength of 12.5%. Small-scale experiments carried out at the BRL indicate an increase in the shock strength of 10% for a 6° divergent nozzle over the entire range of driver-pressure ratio.

An estimate of the uncertainties of the results was attempted by comparing the data points from gages # 2 with those from gage # 3. The records indicate that the pressure loss is negligible as the shock travels over the distance between the two gages (129 mm). The relative differences in the measurements of the shock pressure, $\delta P_{2,3} = (P_2 - P_3)/P_3$, may therefore be used to determine the experimental uncertainties. The mean of the differences was determined to $\bar{x}$ = 2.9% with a standard deviation σ_{n-1} = 2.6%. This result implies that the loss in shock strength recovery between the 16° and the 90° half nozzles of about 10% is statistically significant and therefore real.

5. CONCLUSION

Four convergent/divergent nozzle configurations were successfully tested at seven driver-pressure ratios to study their flow start-up process. However, the viewing area for the 6° divergent half nozzle and the 90° half nozzle downstream from the nozzle exit was too limited and additional optical test records are desirable for a comparative study of the flow start-up process downstream from the exits of the 90° and 6° half nozzles.

The shadowgraphs and schlieren pictures produced in the optical flow experiments have revealed that

a) the flow is very sensitive to local disturbances, e.g., flow asymmetries caused by the breaking of the diaphragm, diaphragm fragments and boundary-layer build-up,

b) a system of recompression shocks is generated by the flow in the throat channel and in the divergent section of the half nozzle,

c) the start-up process of the nozzle ranges from 2.4 ms at the lowest pressure level (P_{41} = 4) to 0.9 ms at the highest pressure level (P_{41} = 188), for the 45° nozzle.

d) the 90° nozzle effectively forms a divergent section by establishing its flow expansion angle in response to the particular driver pressure ratio,

e) the strong reflections of the incident shock at the exit corner of the 45° and 90° half nozzles interfere with the flow start-up process of these nozzles.

The static pressure was recorded for three nozzle configurations, i.e., the 16°, 45° and 90° divergent half nozzles. The pressure records indicate that

f) a loss in shock strength of about 10% is associated with the 90° half nozzle as compared to the shock strength of the 16° divergent half nozzle at the highest driver pressure ratio,

g) due to the low expansion ratio, no pressure spikes were observed at the incident shock front such as were found in the experimental CEG-SSGG pressure histories or in the BRL-Q1D computations.

REFERENCES

[1] Amann, H.-O., "Vorgaenge beim Start einer ebenen Reflexionsduese" Bericht Nr. 9/68, Ernst-Mach-Institut, Freiburg i. Br., Eckerstrasse 4, 1968.

[2] Opalka, K. O., "Large Blast and Thermal Simulator Advanced Concept Driver Design by Computational Fluid Dynamics", BRL-TR-3026, US Army Ballistic Research Laboratory, Aberdeen Proving Ground, Maryland 21005, August 1989.

[3] Opalka, K. O. and Pearson, R. J., "Real Time Flow Control in Large Blast/Thermal Simulators", Proceedings of the 1988 Army Science Conference, Ft. Monroe, Hampton Va., 25-28 October 1988.

[4] Opalka, K. O., "Large Blast-Wave Simulators (LBS) With Cold-Gas Drivers: Computational Design Studies", BRL-TR-2786, US Army Ballistic Research Laboratory, Aberdeen Proving Ground, Maryland 21005, March 1987.

[5] Opalka, K. O. and Mark, A., "The BRL-Q1D Code: A Tool for the Numerical Simulation of Flows in Shock Tubes with Variable Cross-Sectional Areas," BRL-TR 2763, US Army Ballistic Research Laboratory, Aberdeen Proving Ground, Maryland 21005, October 1986.

[6] "Picsure User's Guide", Copywright by Precision Visuals, Inc., 6260 Lookout Road, Boulder, Colorado 80301, USA

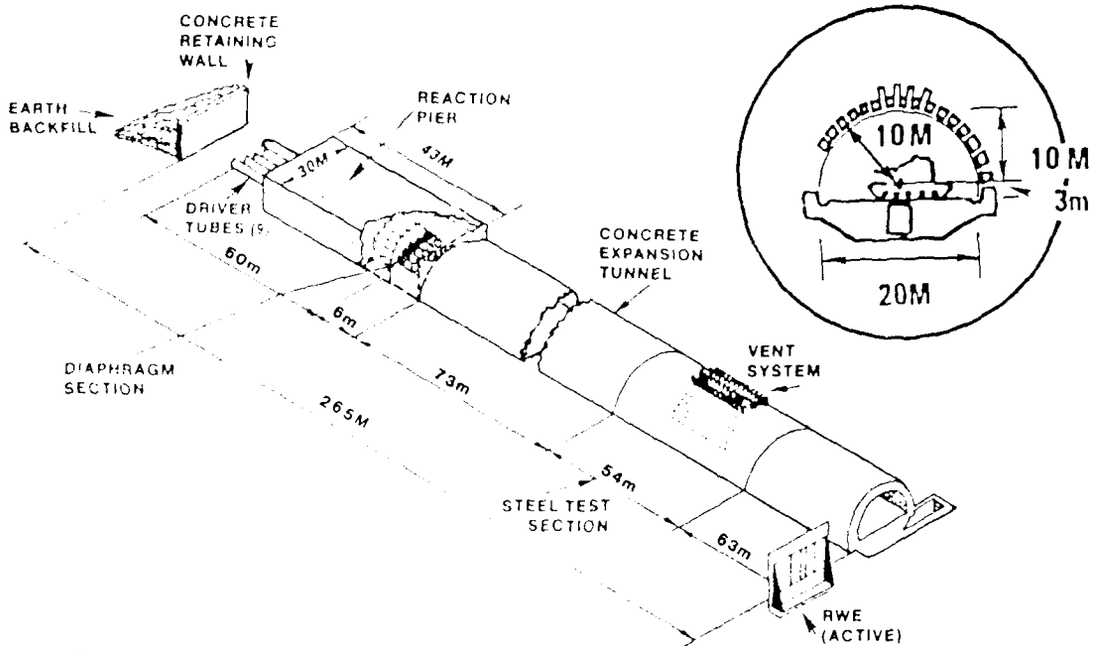

(a) Layout of U.S. Facility

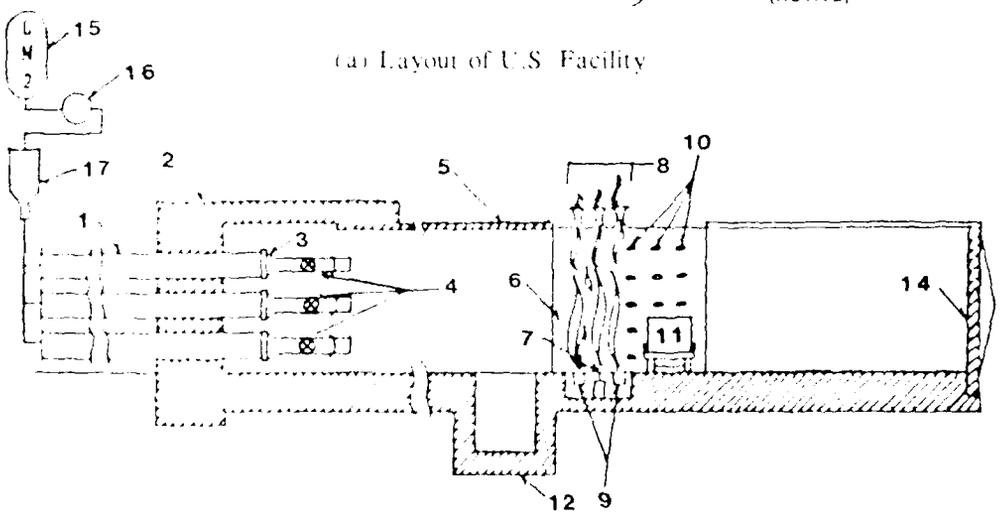

LEGEND

1 - Steel Driver Tubes	9 - Air Curtain Plenum
2 - Concrete Reaction Pier	10 - Instrumentation and Light Ports
3 - Converging Nozzles	11 - Test Target
4 - Throat Valves and Diaphragms	12 - Soil Tank
5 - Concrete Expansion Tunnel	14 - Rarefaction Wave Eliminator
6 - Steel Test Section	15 - Liquid Nitrogen Storage
7 - Thermal Radiation Sources	16 - Cryogenic Pumps
8 - Combustion Products Ejectors	17 - Pebble-Bed Superheaters

(b) The LB/TS Concept

Figure 1: The U.S. Large Blast and Thermal Simulation Facility

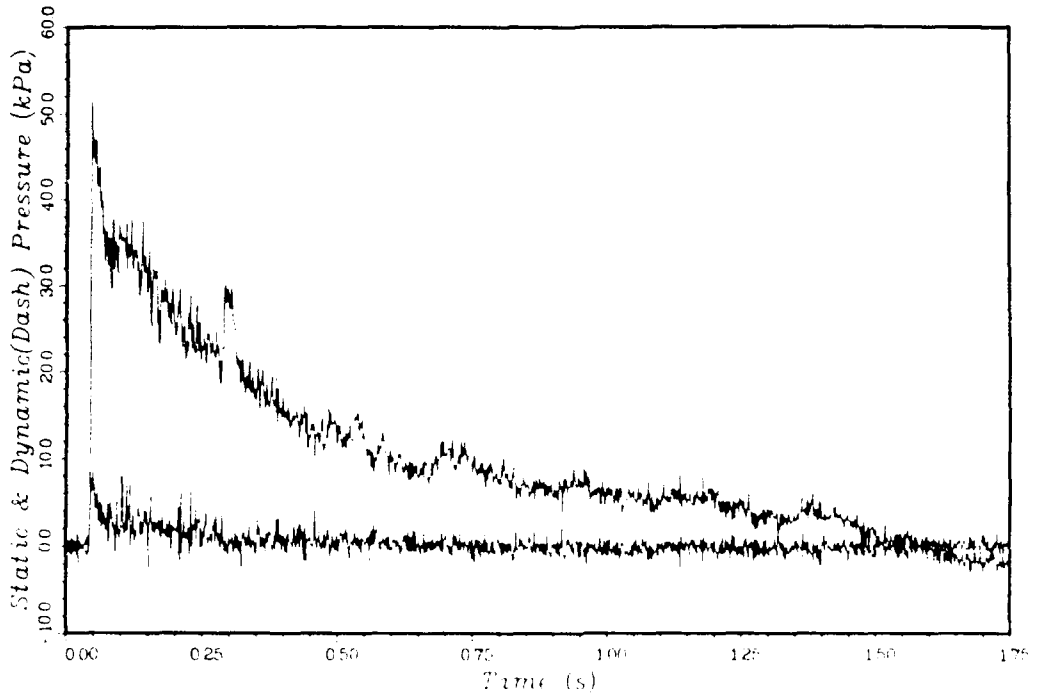

(a) Experimental Record (CEG-SSGG)

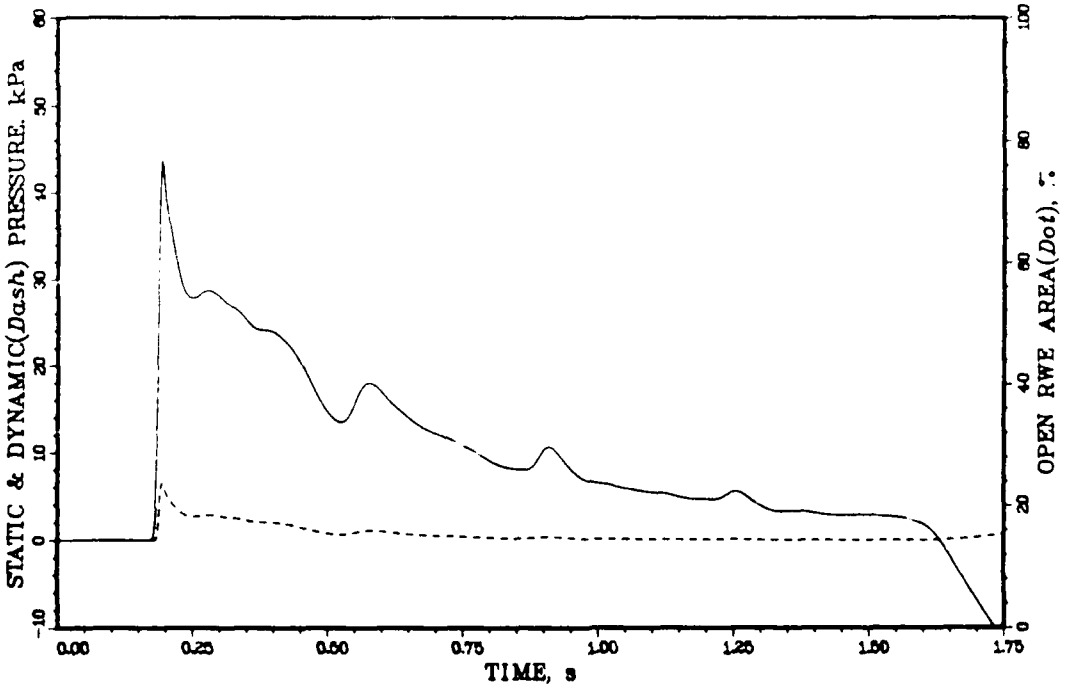

(b) Computational Record (BRL-Q1D)

Figure 2: Experimental and Computational Pressure History for a 42 kPa/10 kT Blast Wave.

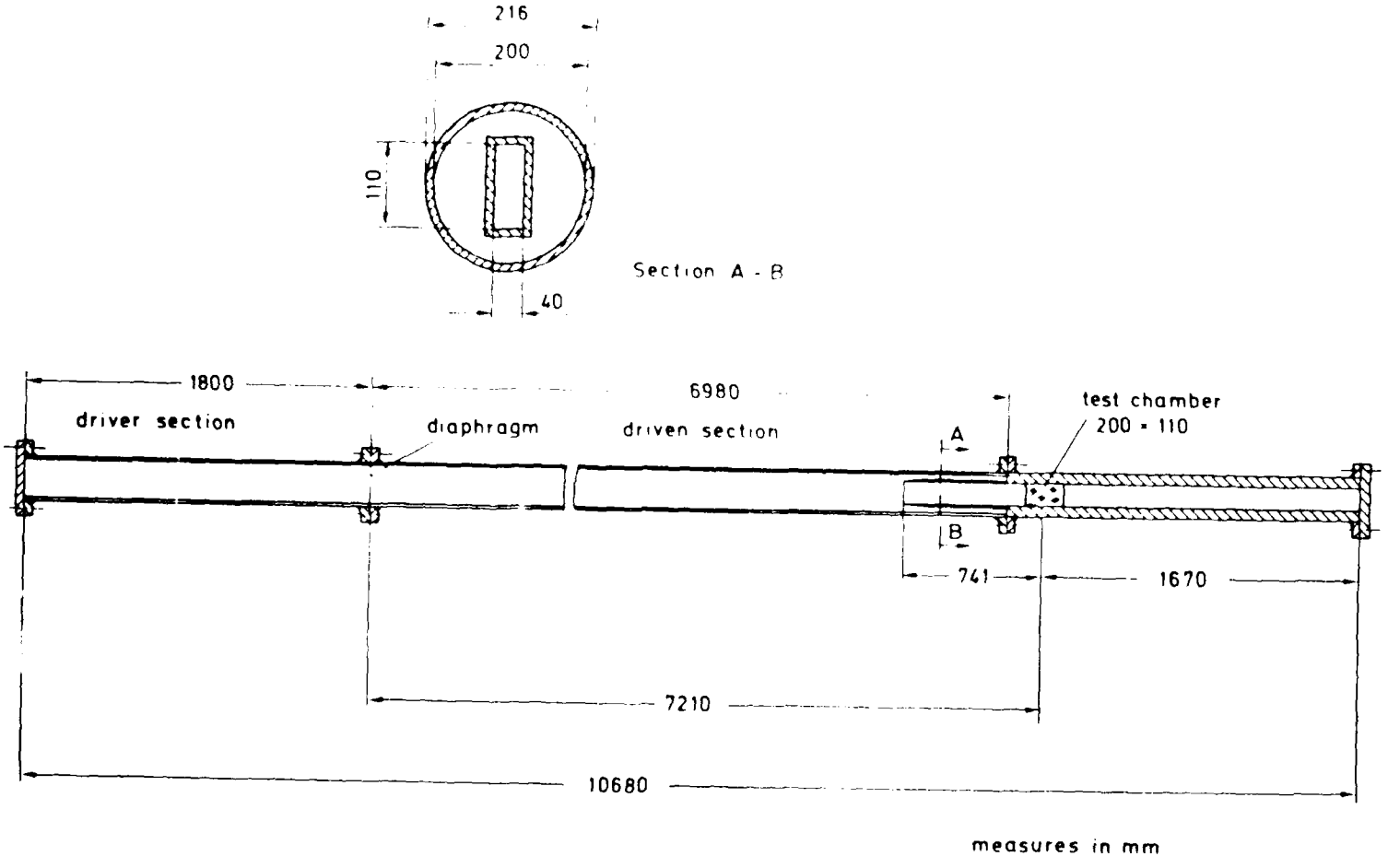

Figure 3: EMI 200mm Shock Tube

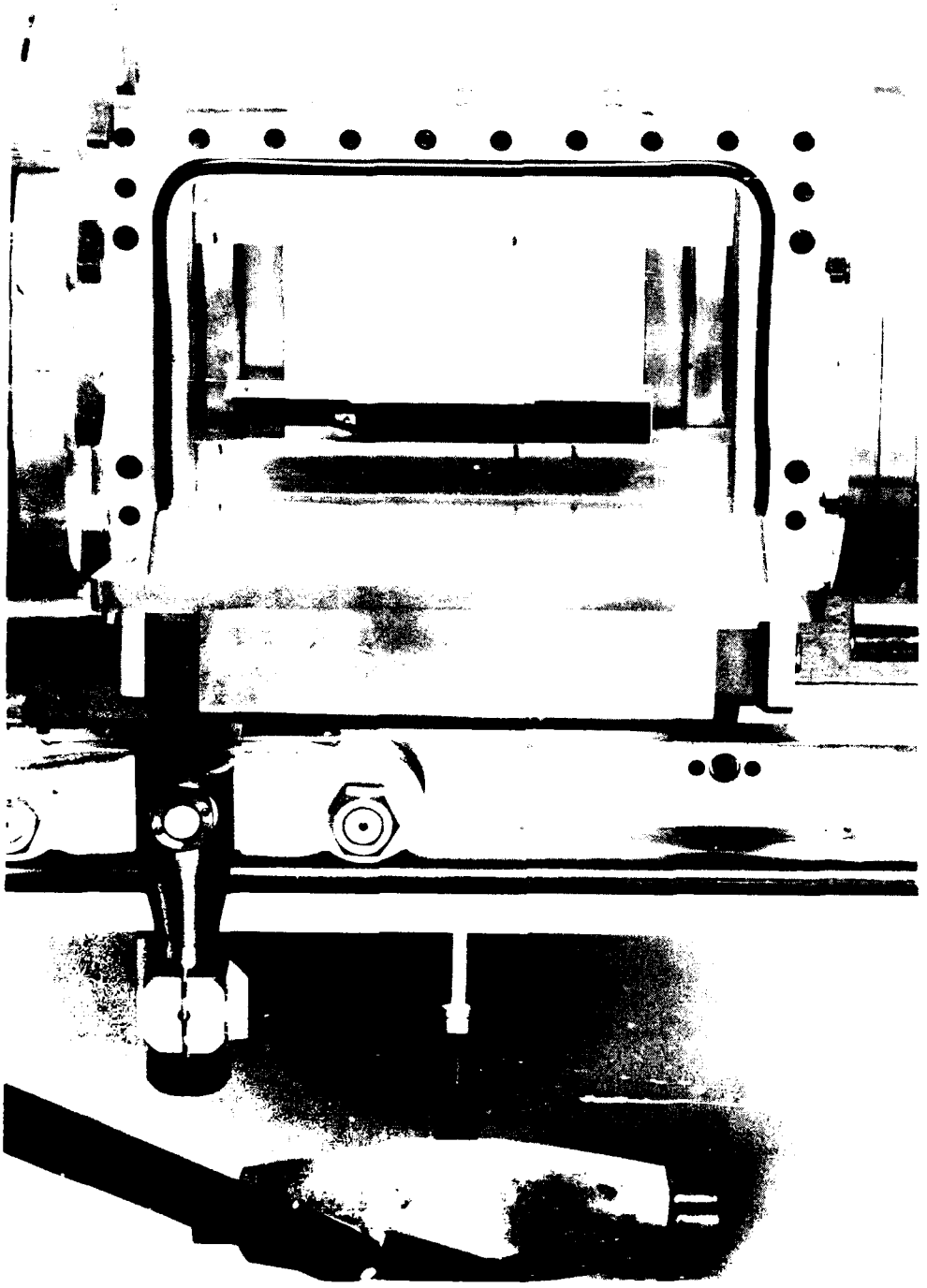

Figure 4: Optical Test Chamber

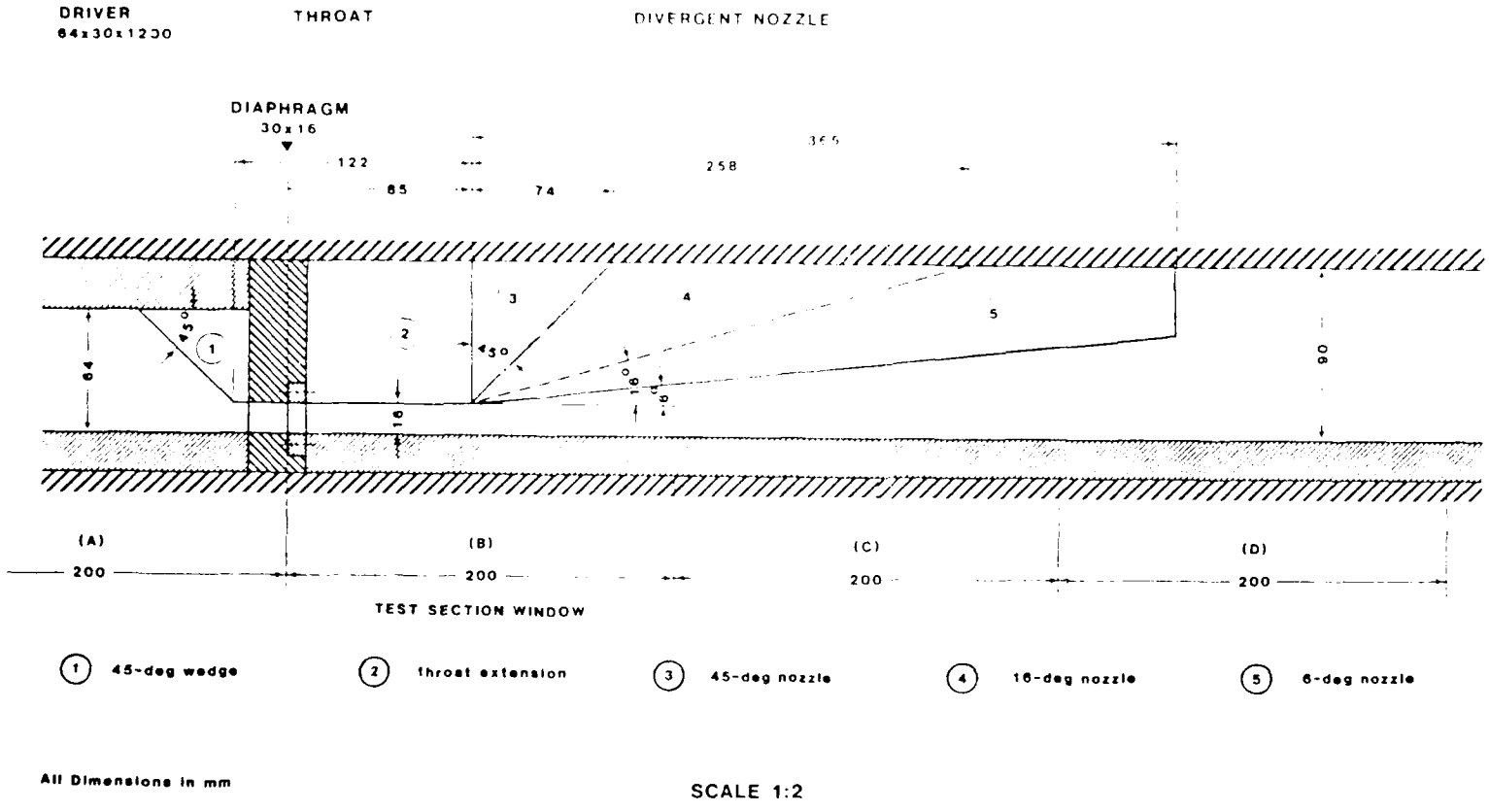

Figure 5: 2D EMI Half-Nozzle Design

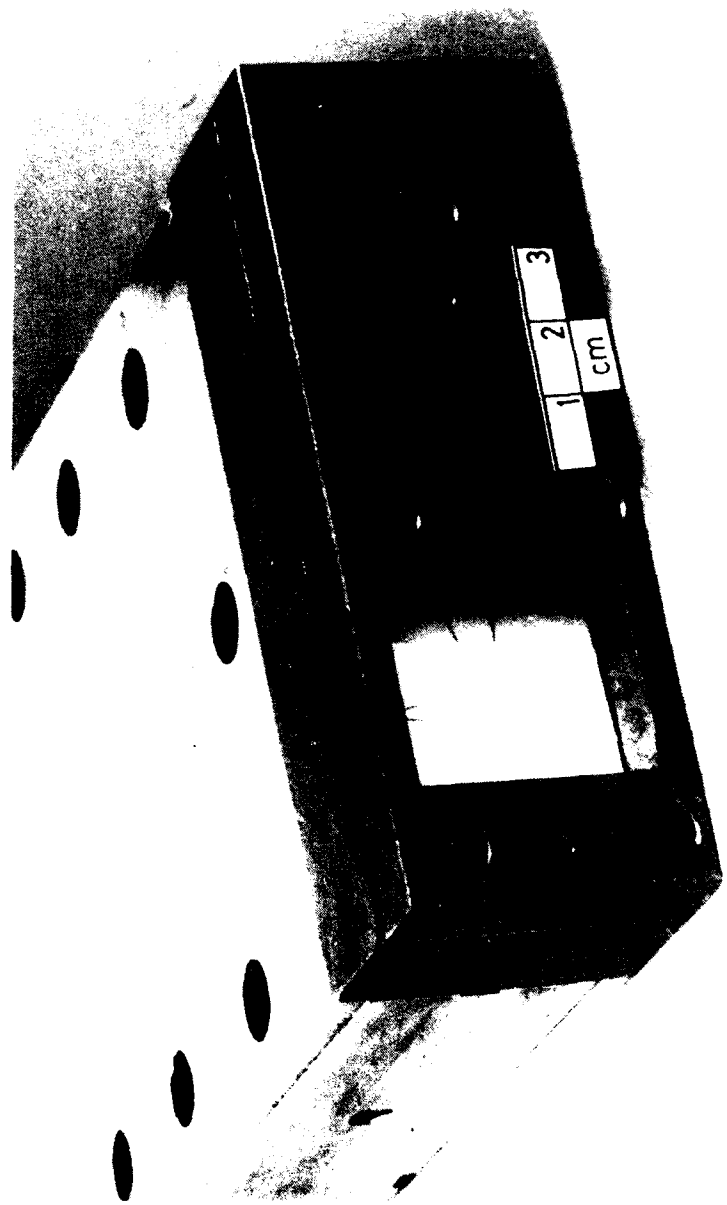

(a) Diaphragm Section

Figure 6: Models of the Divergent Nozzle Configurations

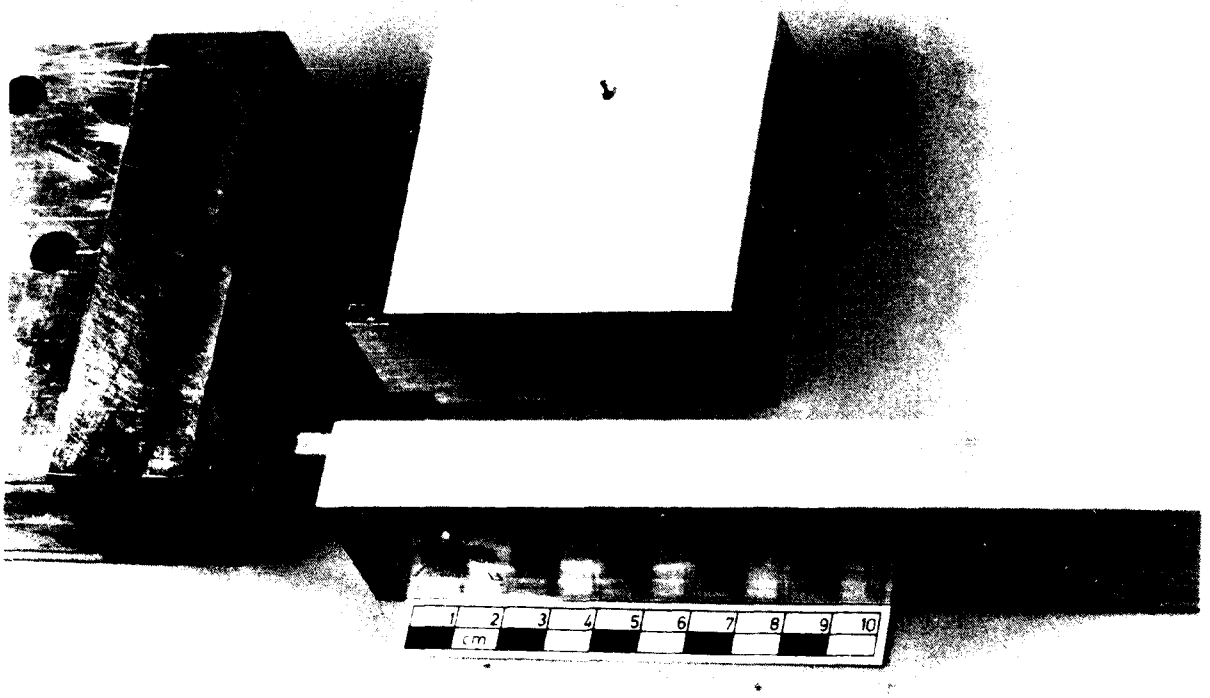

(b) 90° Nozzle

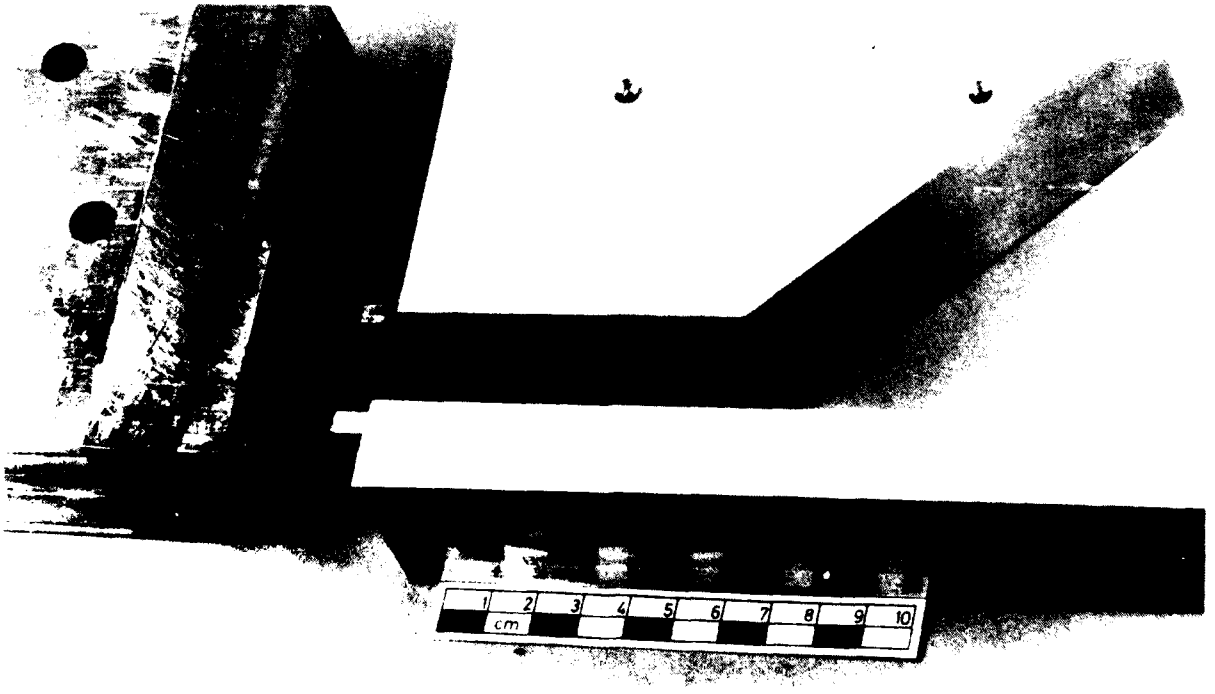

(c) 45° Nozzle

Figure 6: (continued)

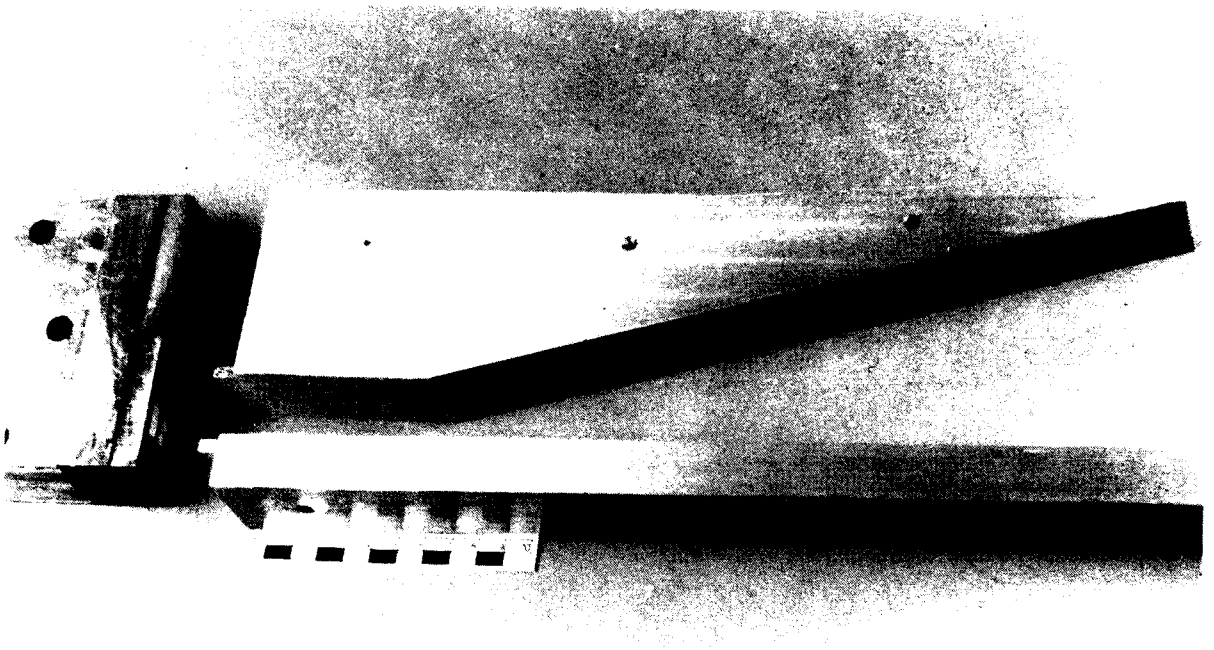

(d) 16° Nozzle

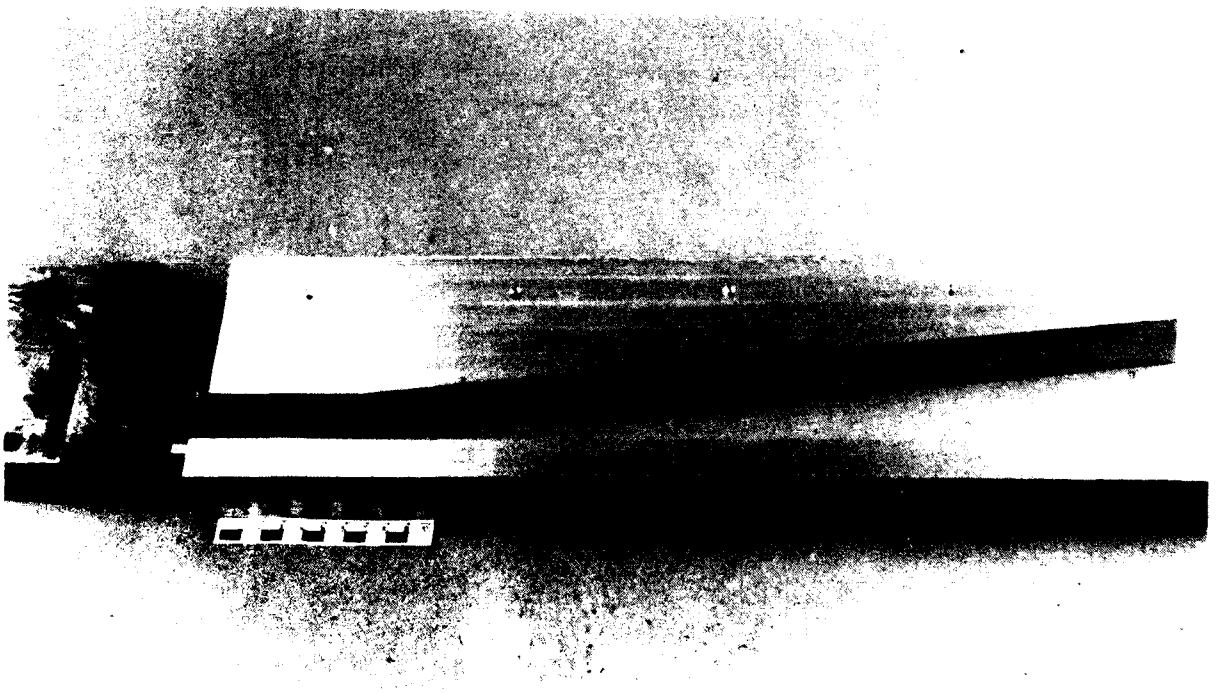

(e) 6° Nozzle

Figure 6: (concluded)

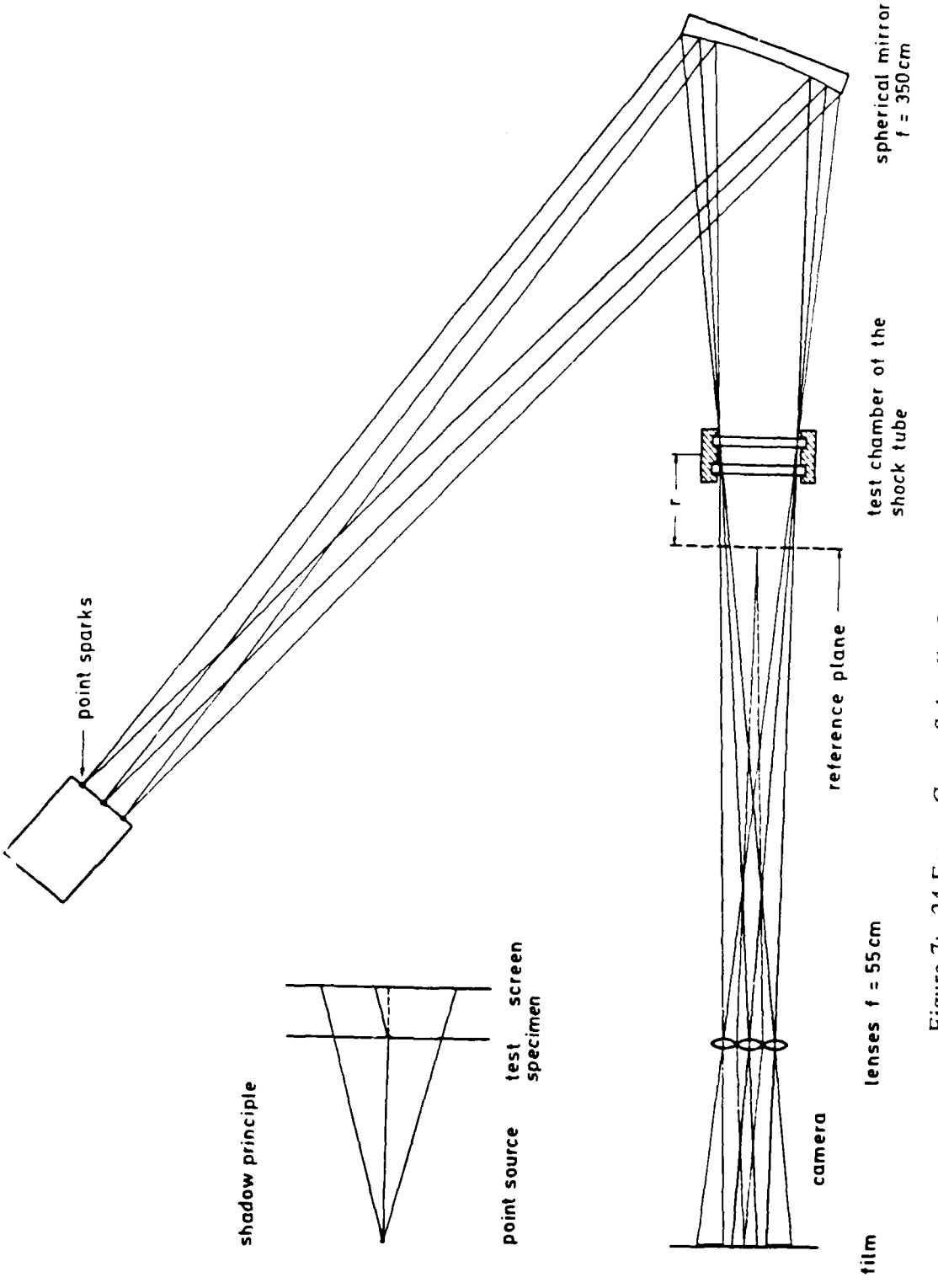

Figure 7: 24-Frame Cranz-Schardin Camera - Shadowgraph Arrangement

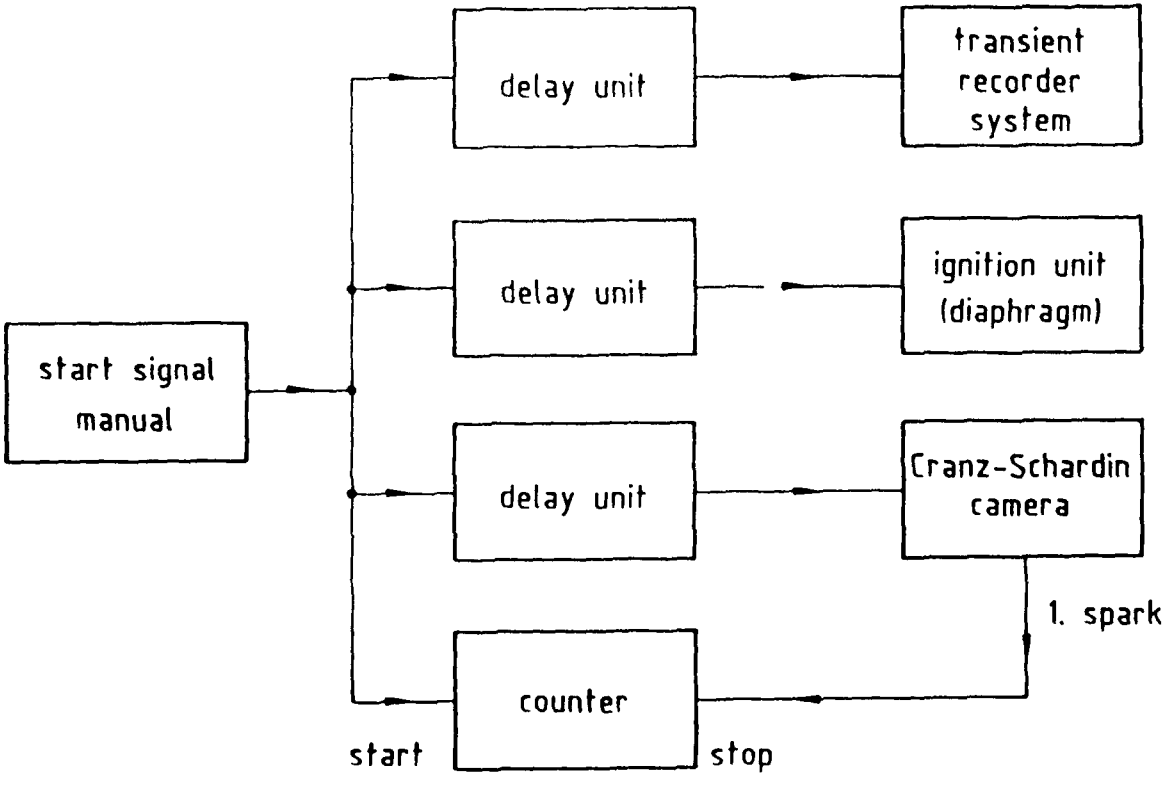

Figure 8: Triggering Circuit

N16/014

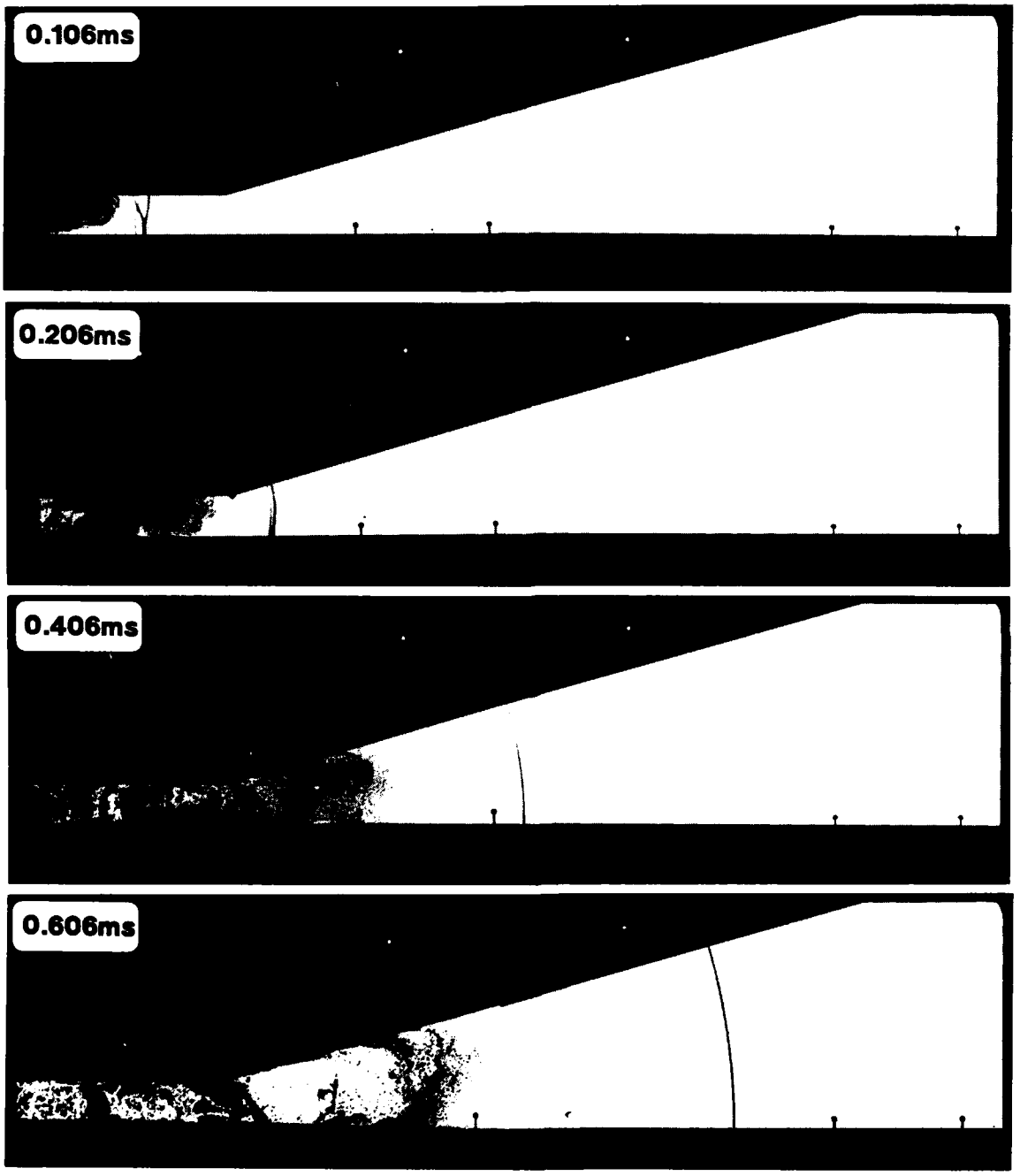

a) Early Times

Figure 9: Shadowgraph Sequence for the 16° Half Nozzle at a Driver Pressure Ratio, P_{41} = 14 (Code N16/014).

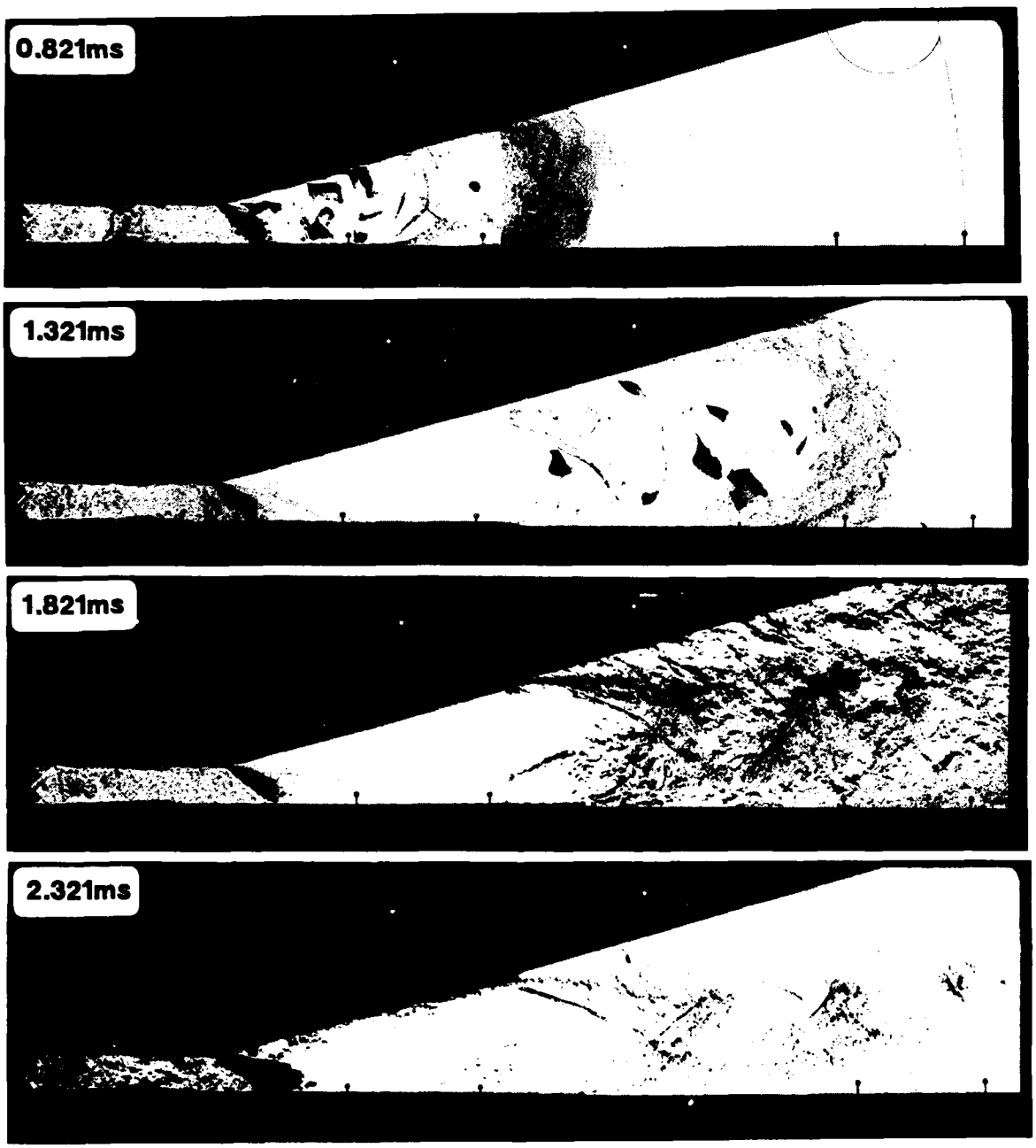

b) Late Times

Figure 9: (concluded)

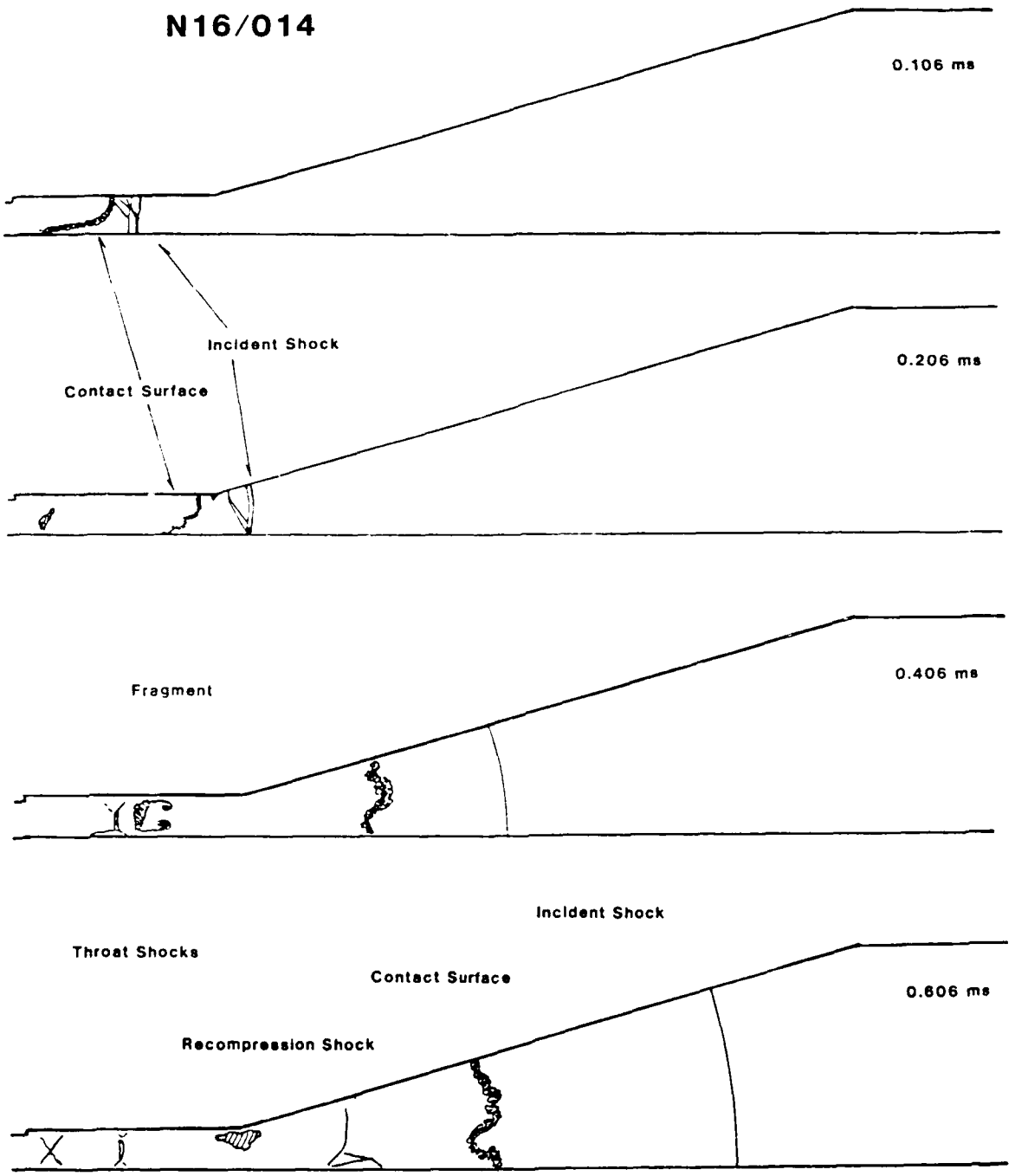

a) Early Times

Figure 10: Illustration of Flow Phenomena in the 16° Half Nozzle at a Driver Pressure Ratio, P_{41} = 14 (Code N16/014).

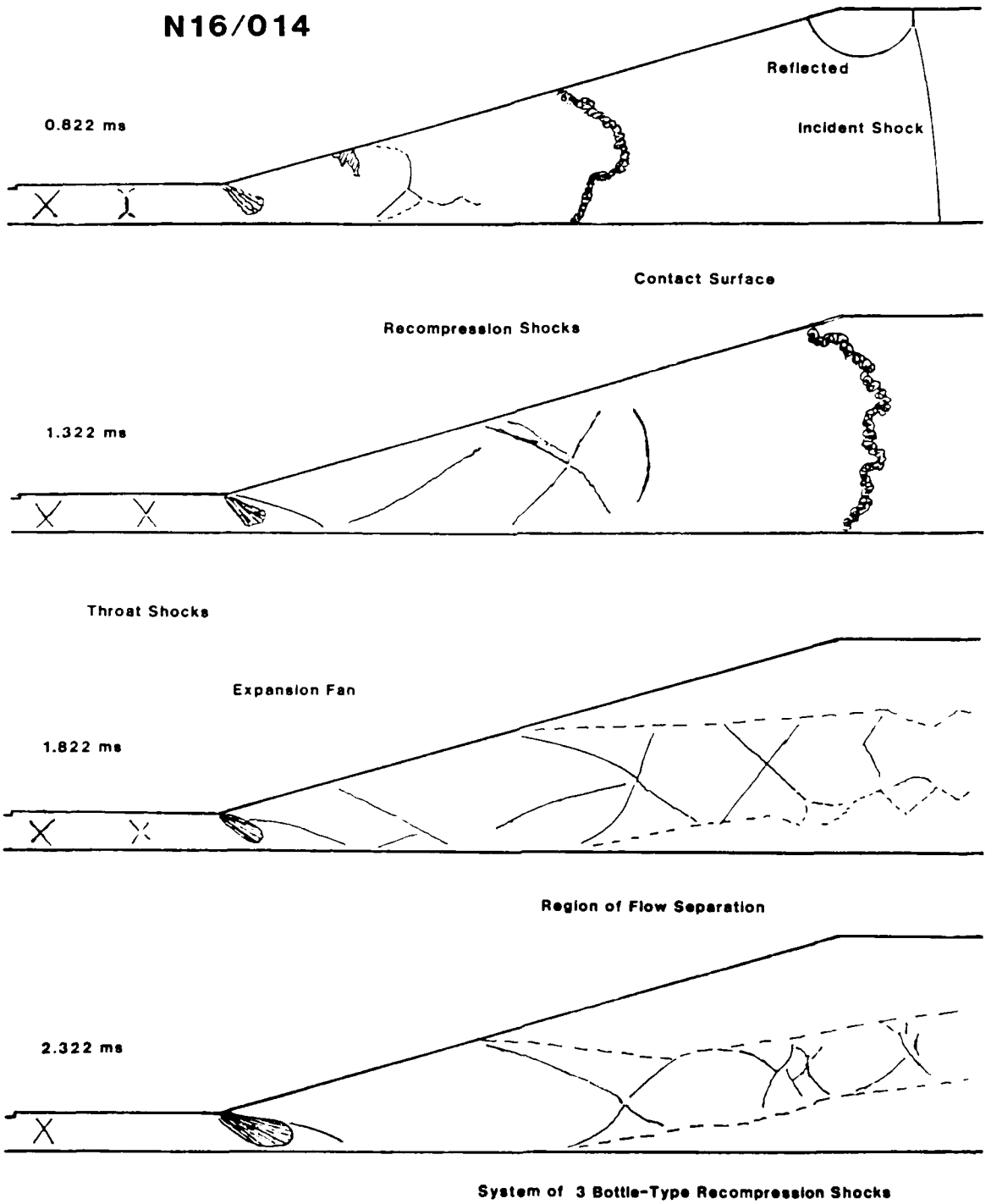

Figure 10: (concluded)

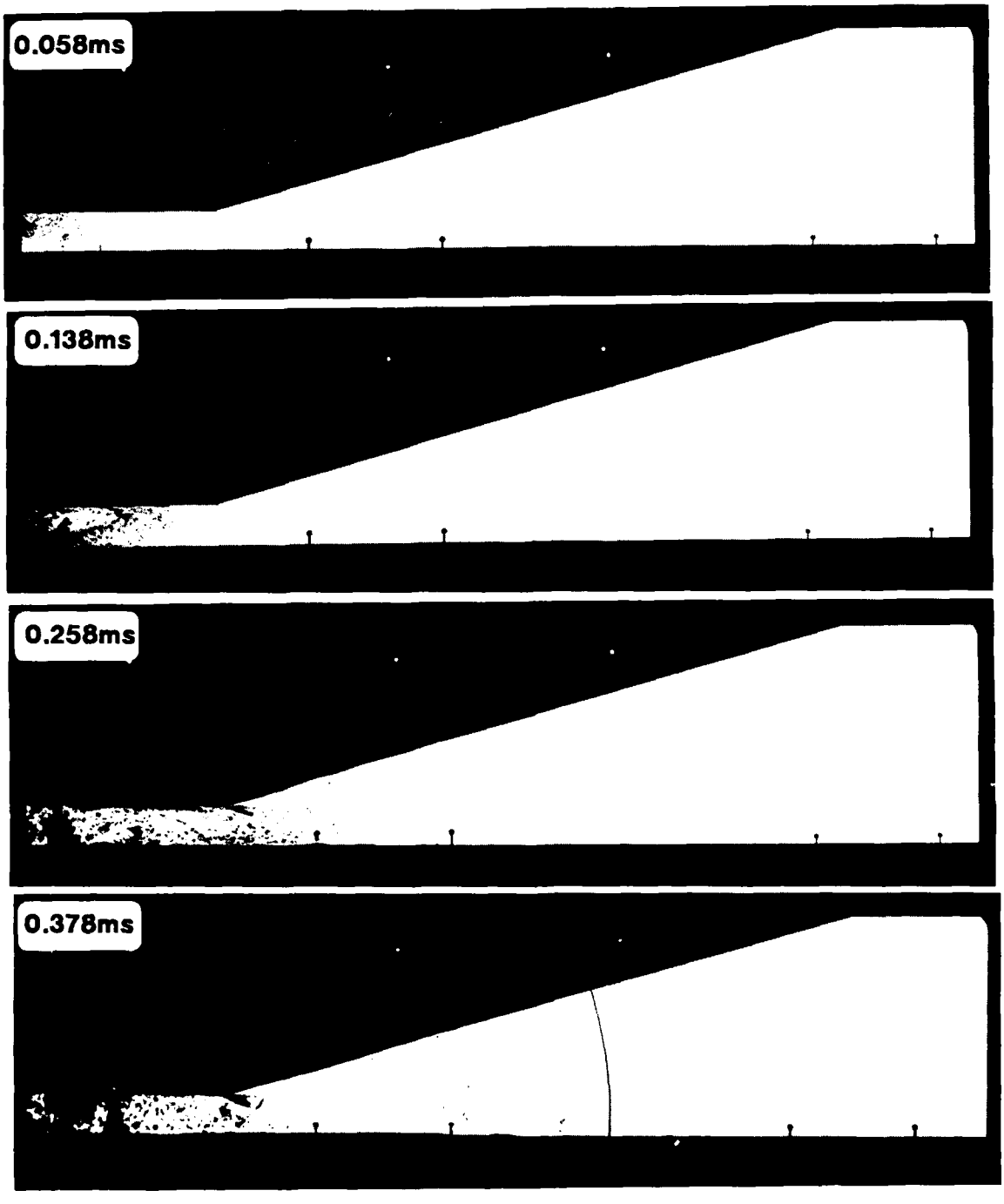

a) Early Times

Figure 11: Shadowgraph Sequence for the 16° Half Nozzle at a Driver Pressure Ratio, P_{41} = 188 (Code N16/188).

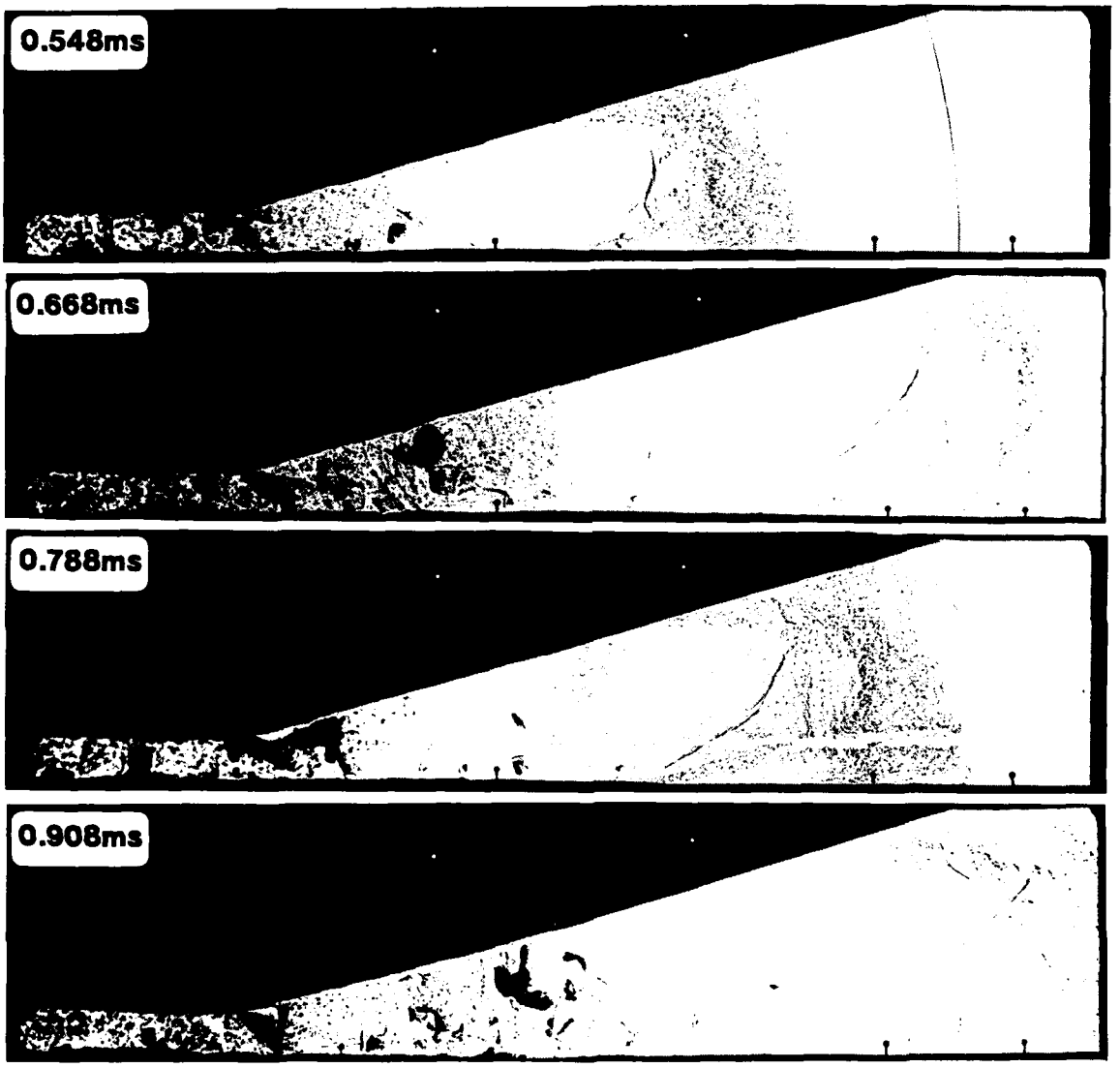

b) Late Times

Figure 11: (concluded)

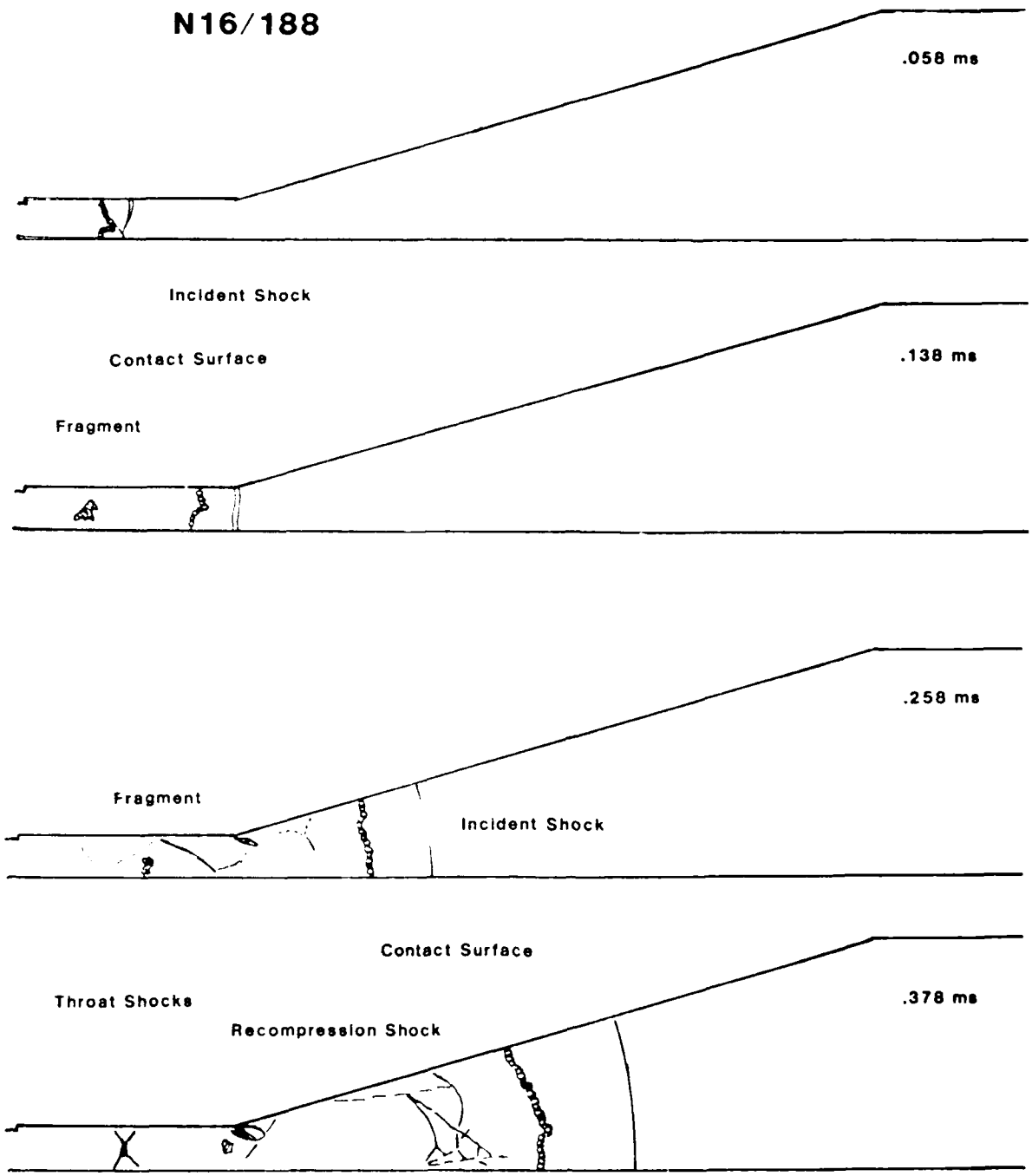

a) Early Times

Figure 12: Illustration of Flow Phenomena in the 16° Half Nozzle at a Driver Pressure Ratio, P_{41} = 188 (Code N16/188).

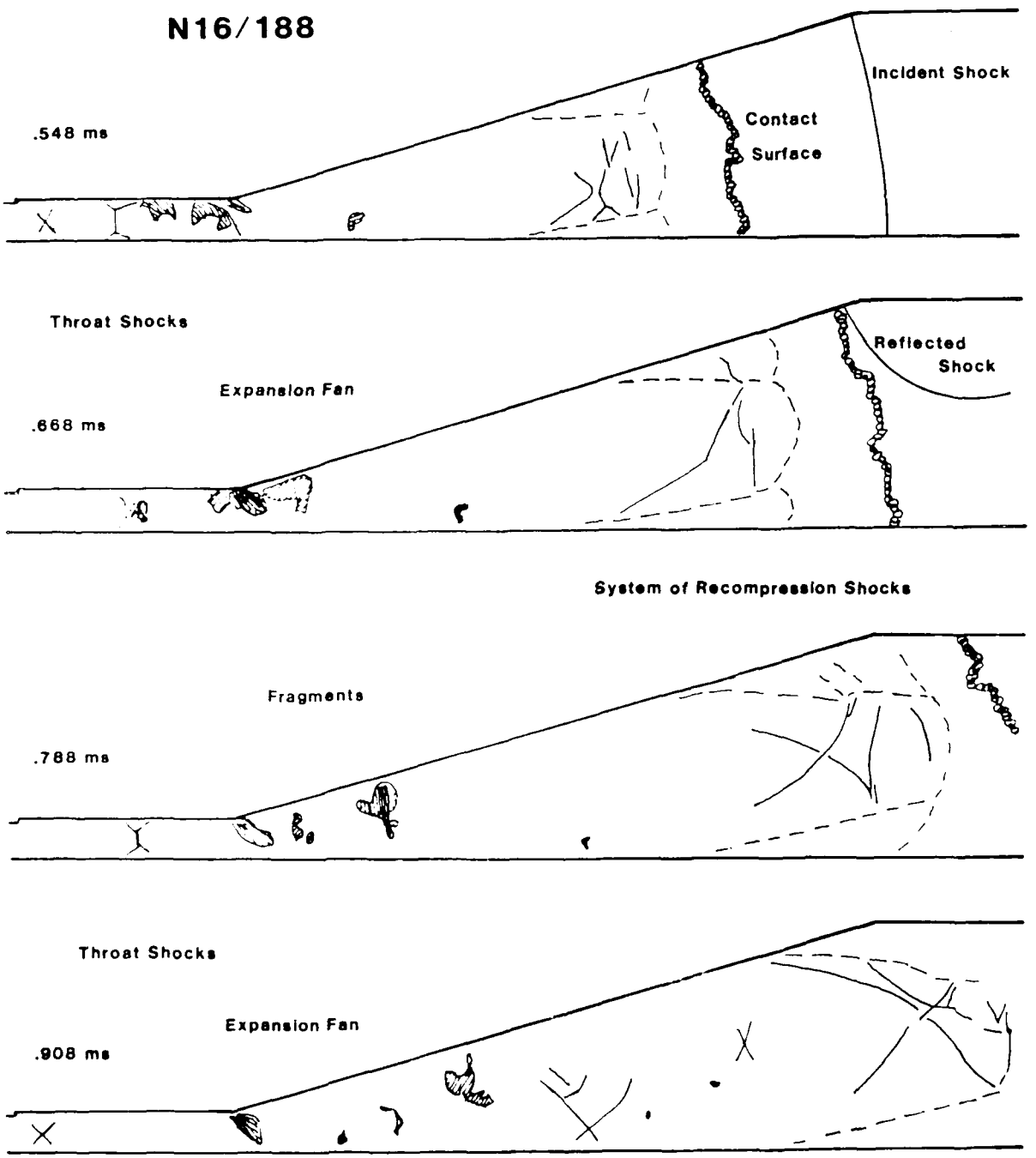

b) Late Times

Figure 12: (concluded)

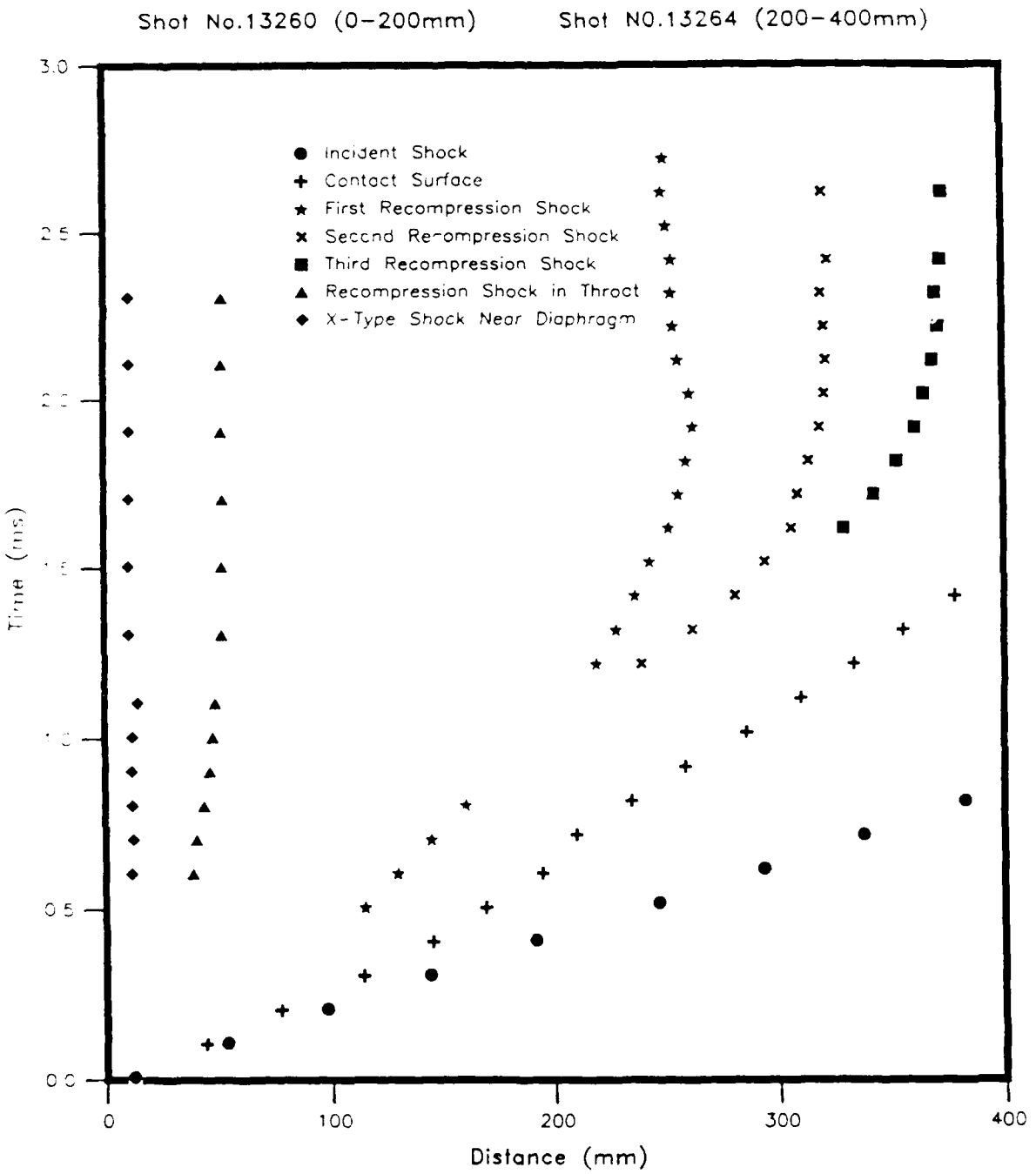

a) Driver-Pressure Ratio P_{41} = 14

Figure 13: x-t Diagrams for the 16° Half Nozzle

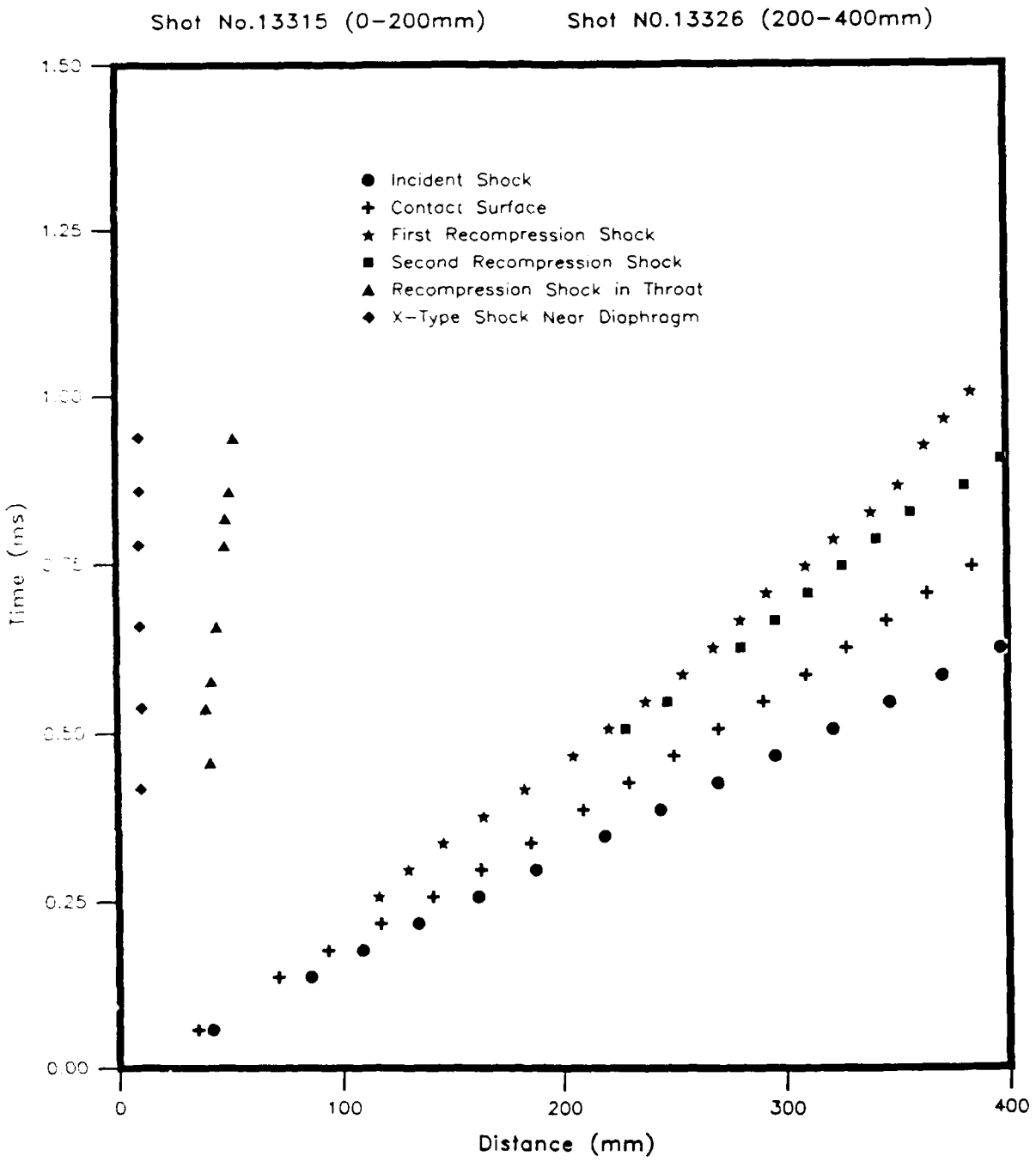

b) Driver-Pressure Ratio, P_{41} = 188

Figure 13: (concluded)

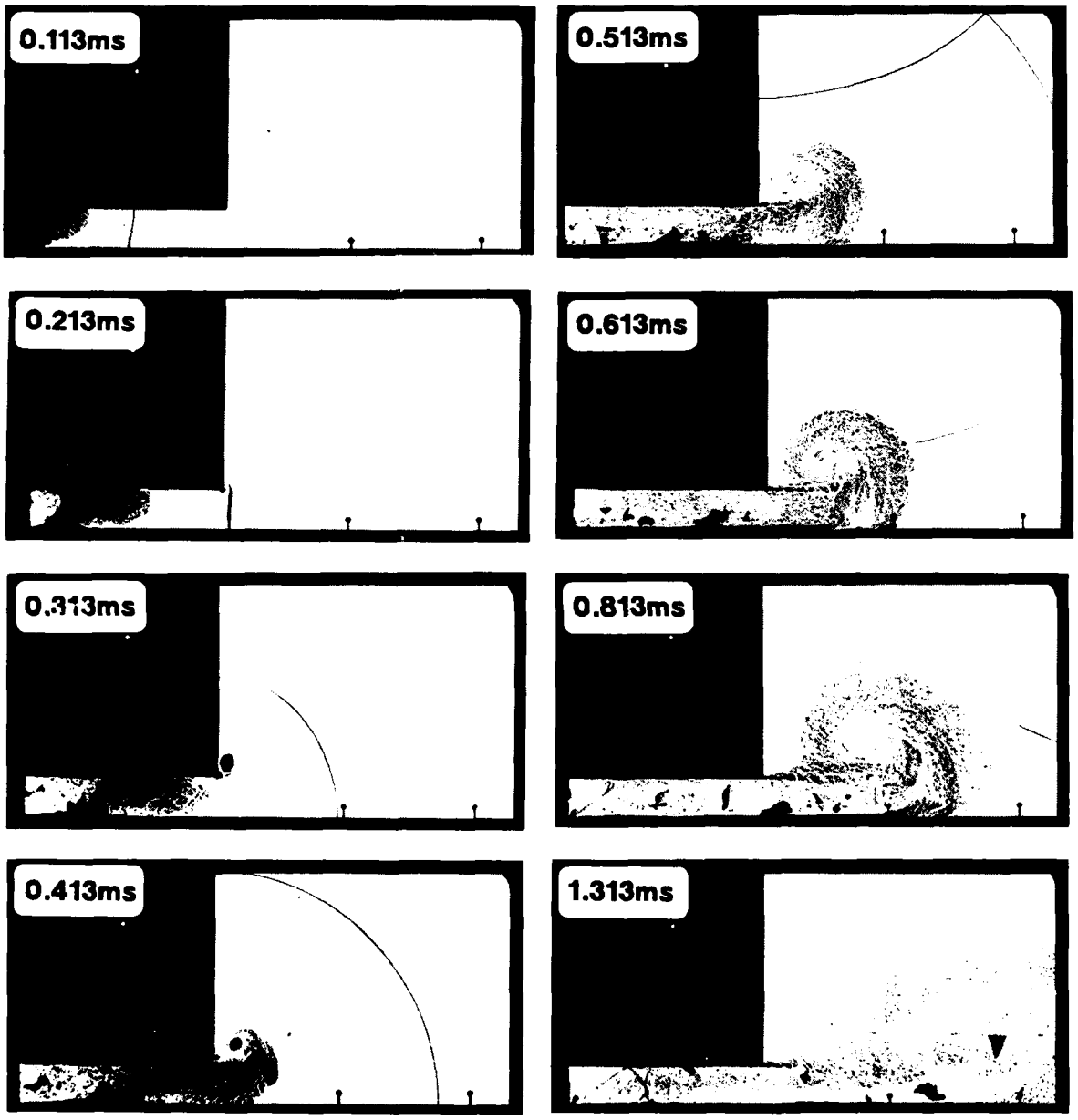

a) Driver-Pressure Ratio, P_{41} = 4

Figure 14: Shadowgraph Sequence for the 90° Half Nozzle

N90/080

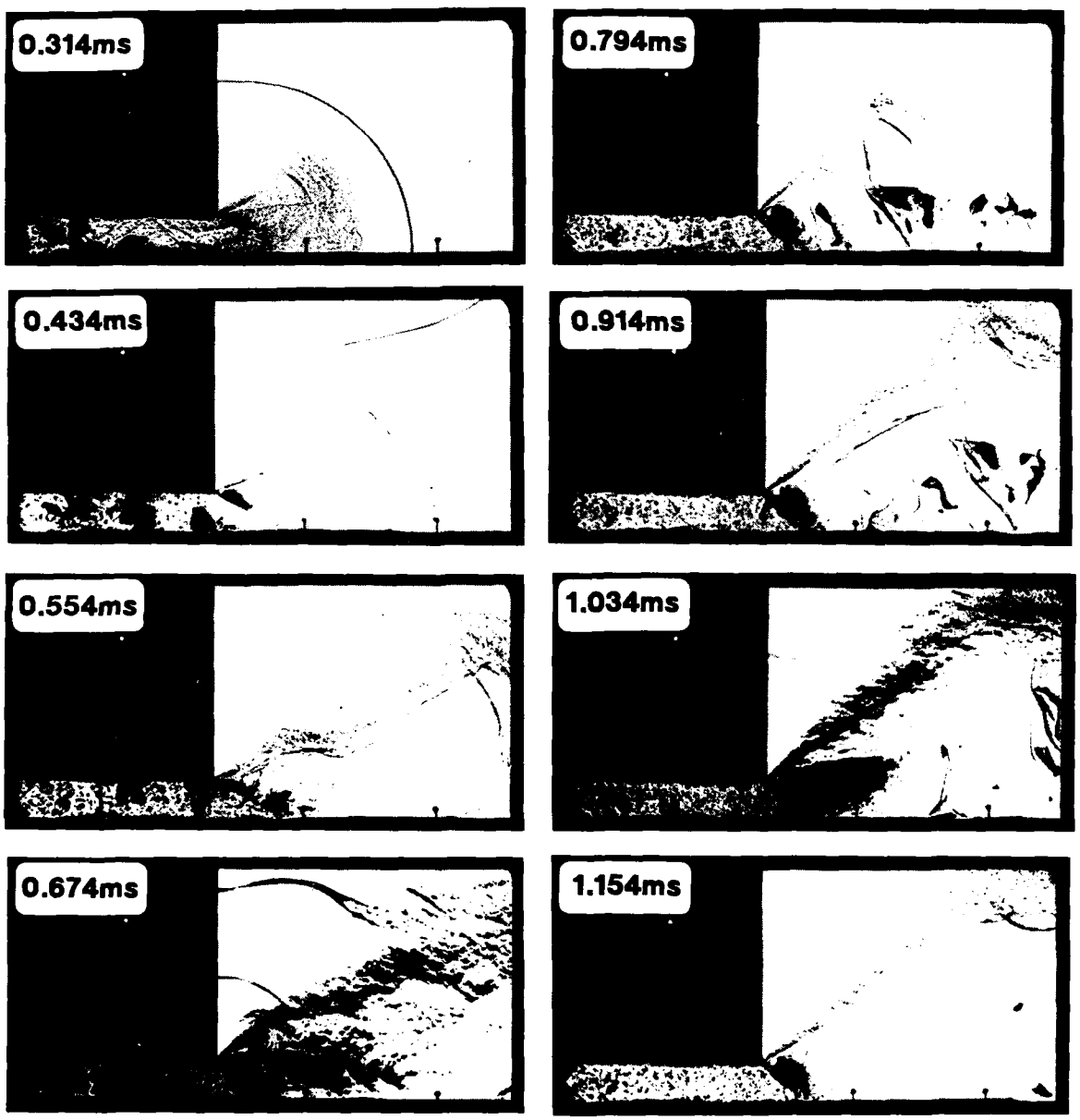

b) Driver-Pressure Ratio, P_{41} = 80

Figure 14: (concluded)

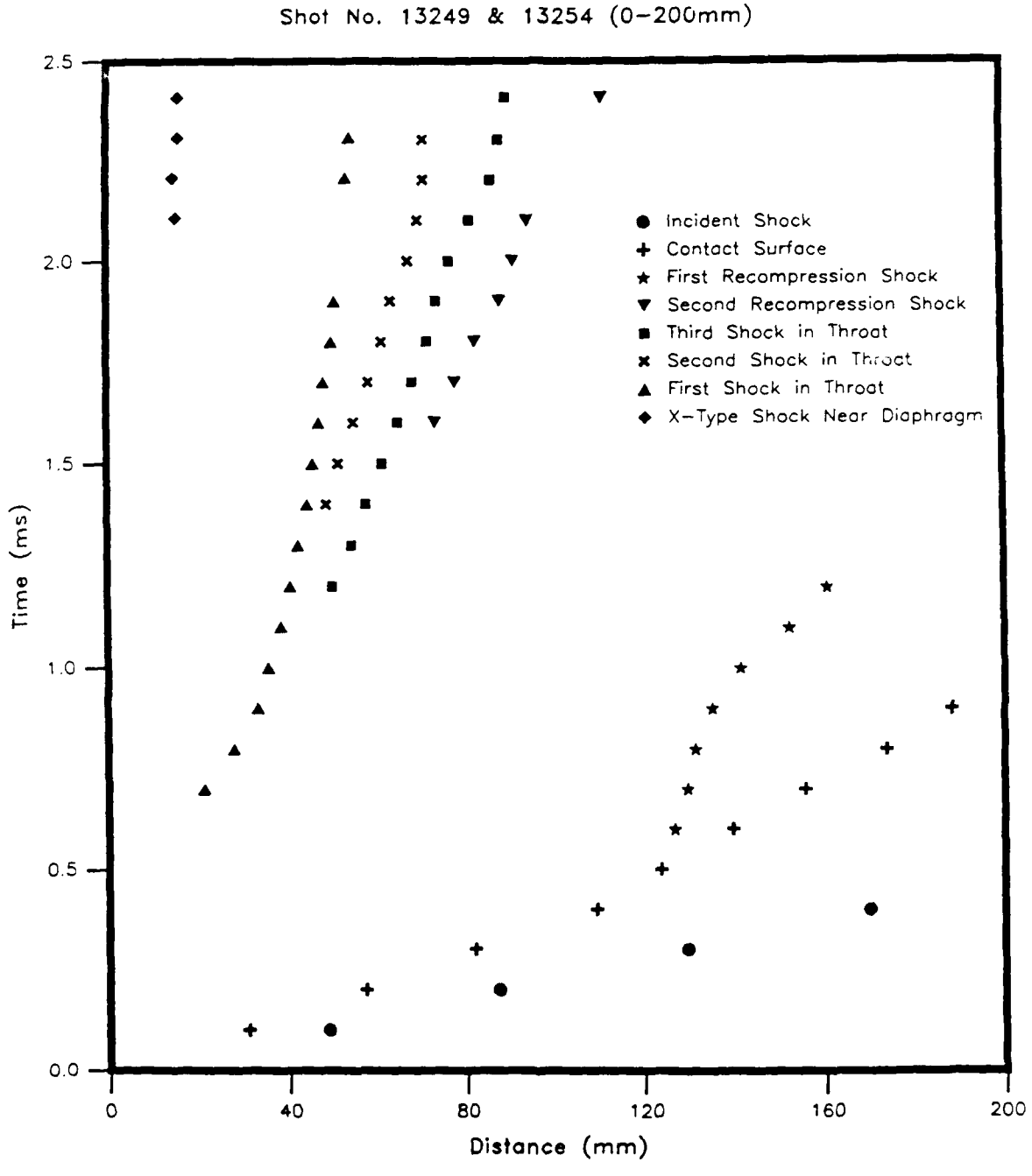

a) Driver-Pressure Ratio, $P_{41} = 4$

Figure 15: x-t Diagrams for the 90° Half Nozzle

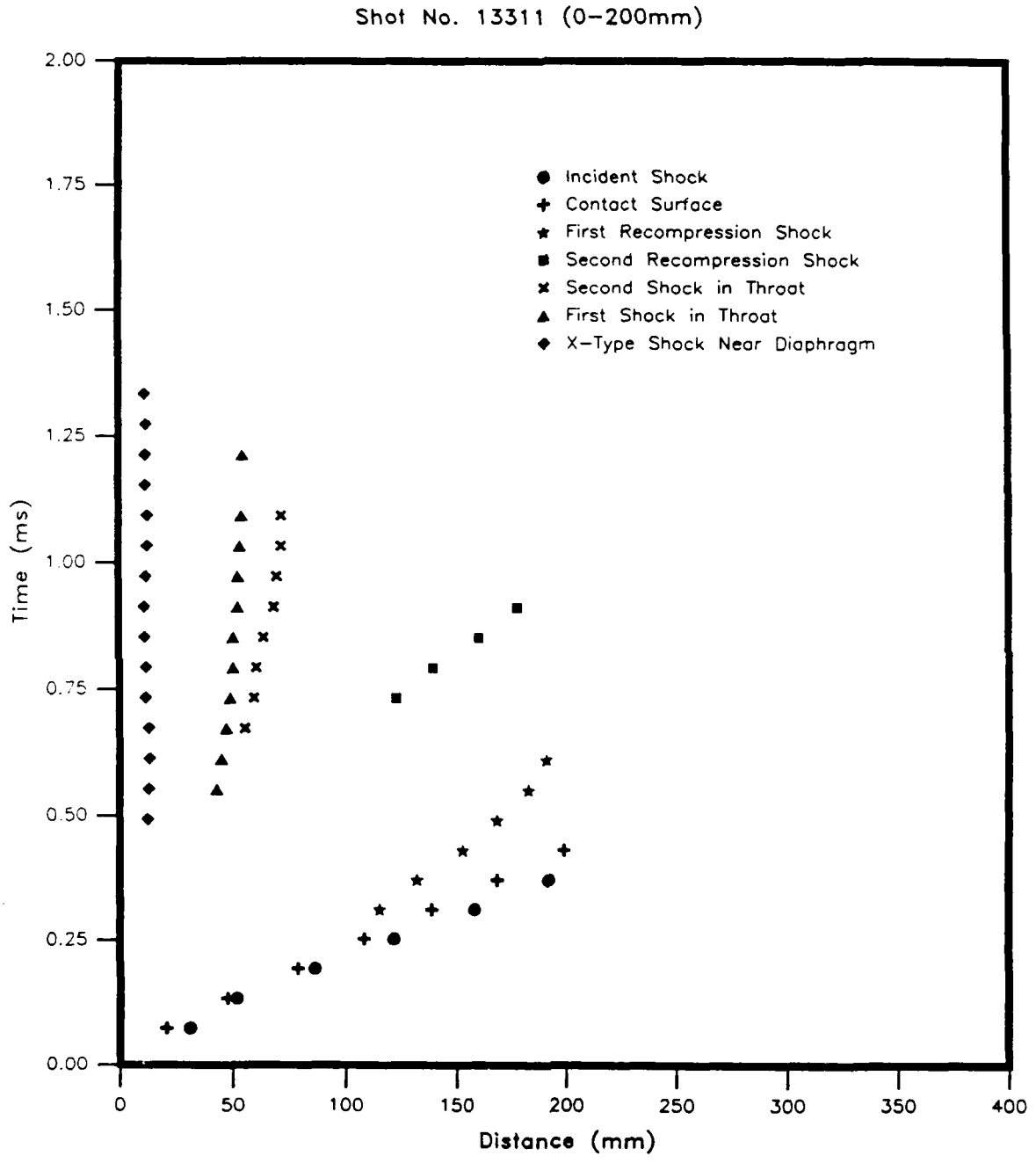

b) Driver-Pressure Ratio, P_{41} = 80

Figure 15: (concluded)

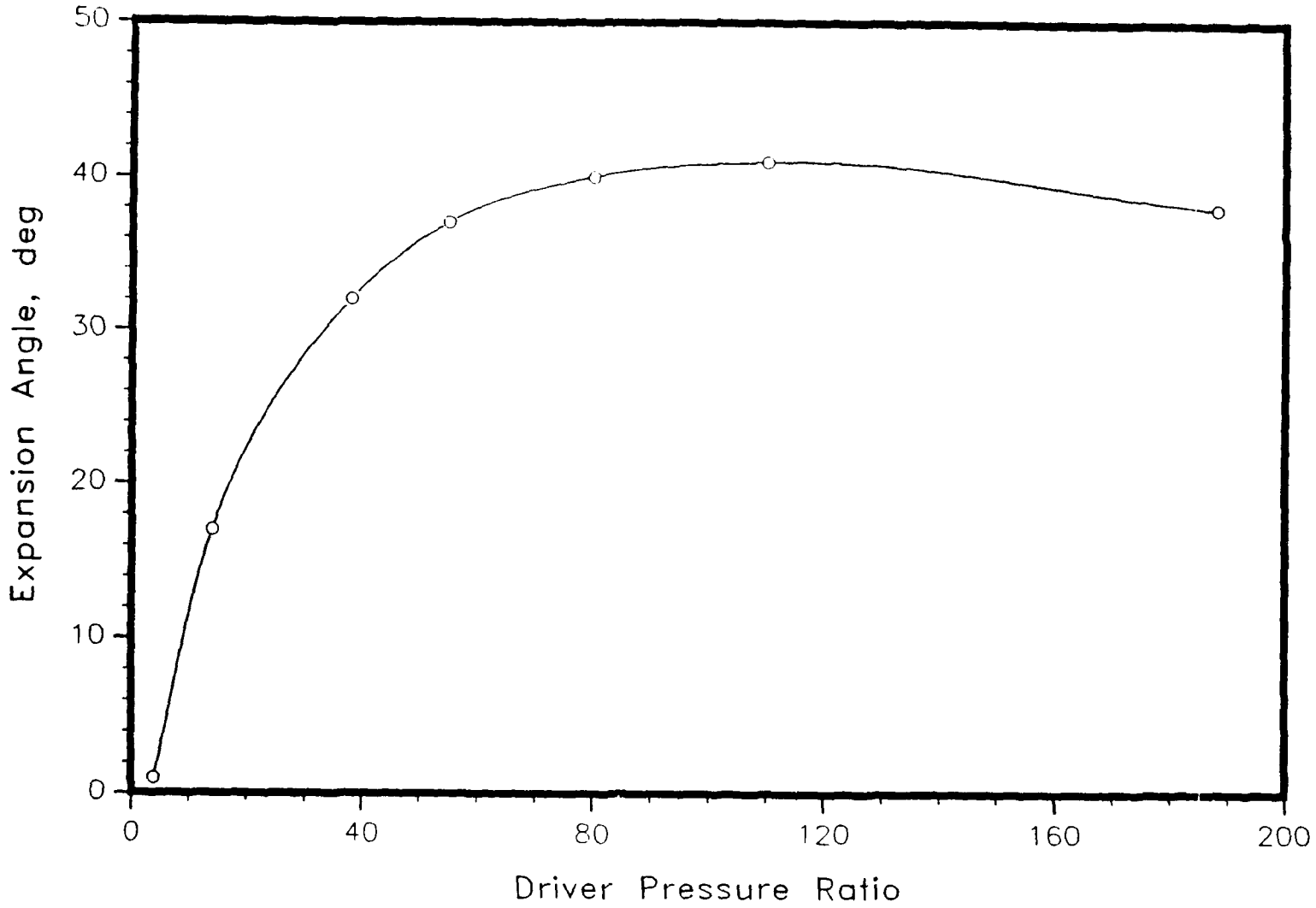

Figure 16: Flow Expansion Angle behind 90° Half Nozzle

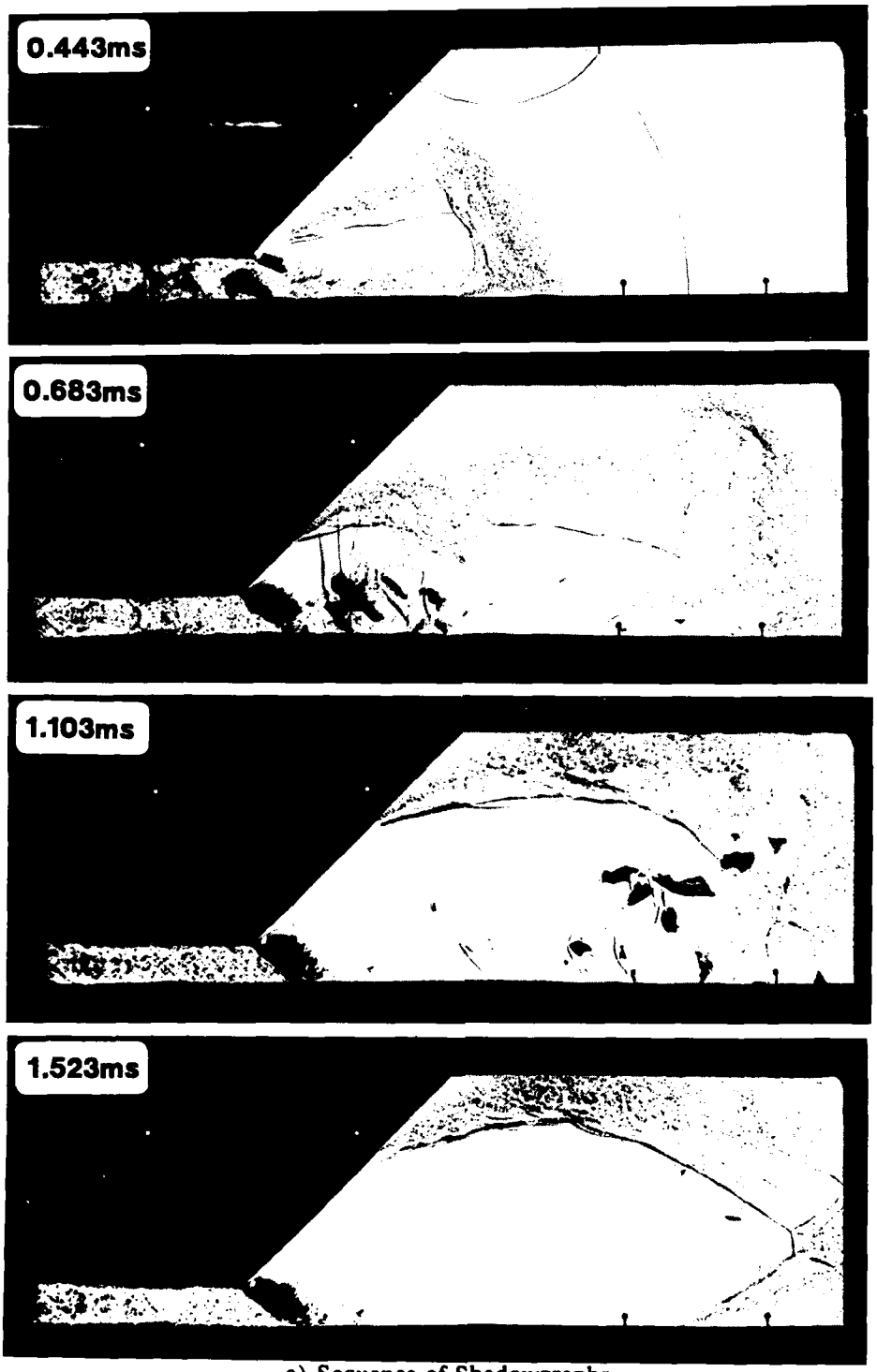

a) Sequence of Shadowgraphs

Figure 17: 45° Half Nozzle at a Driver-Pressure Ratio, P_{41} = 80
(Code N45/080)

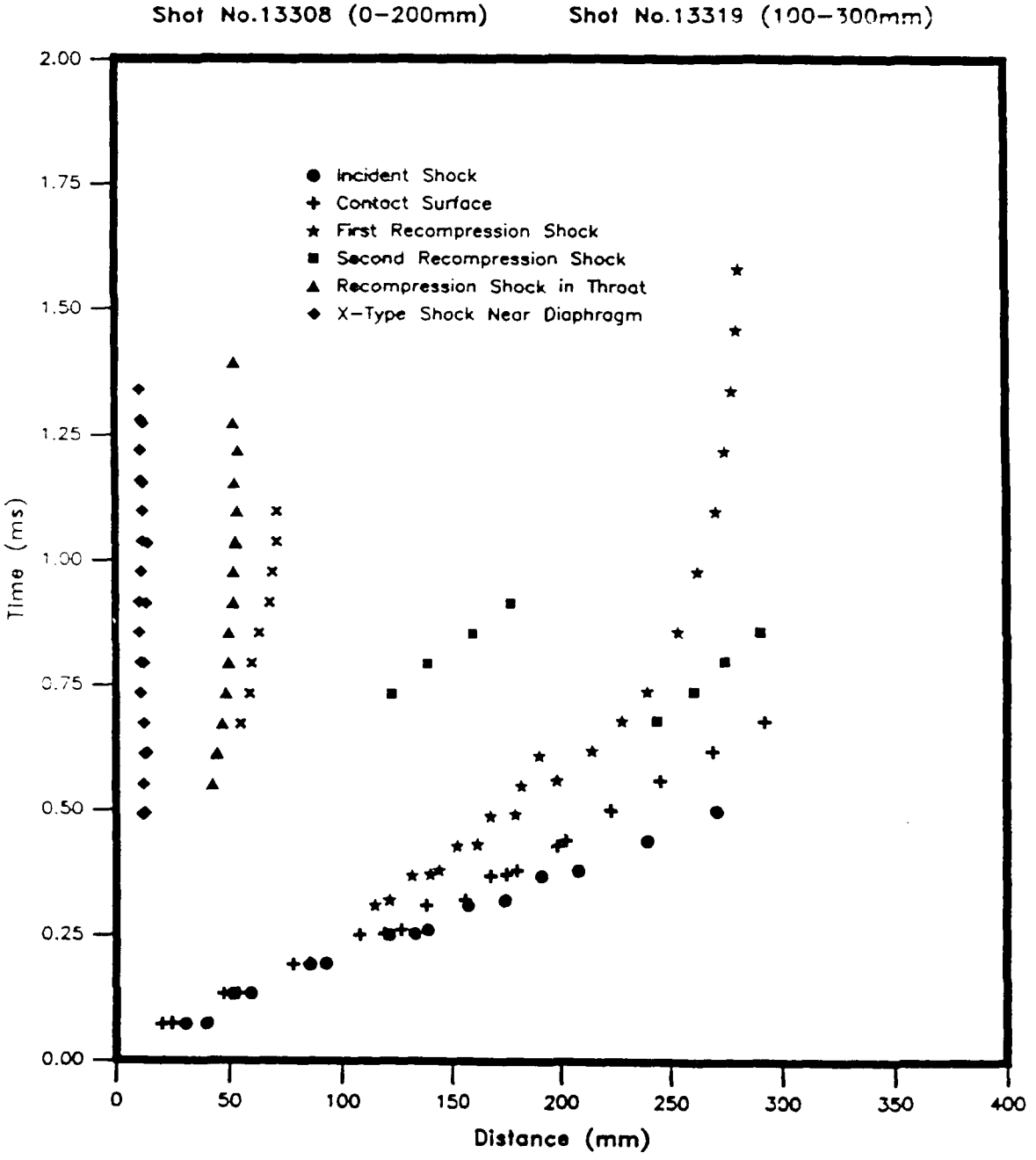

b) x-t diagram

Figure 17: (concluded)

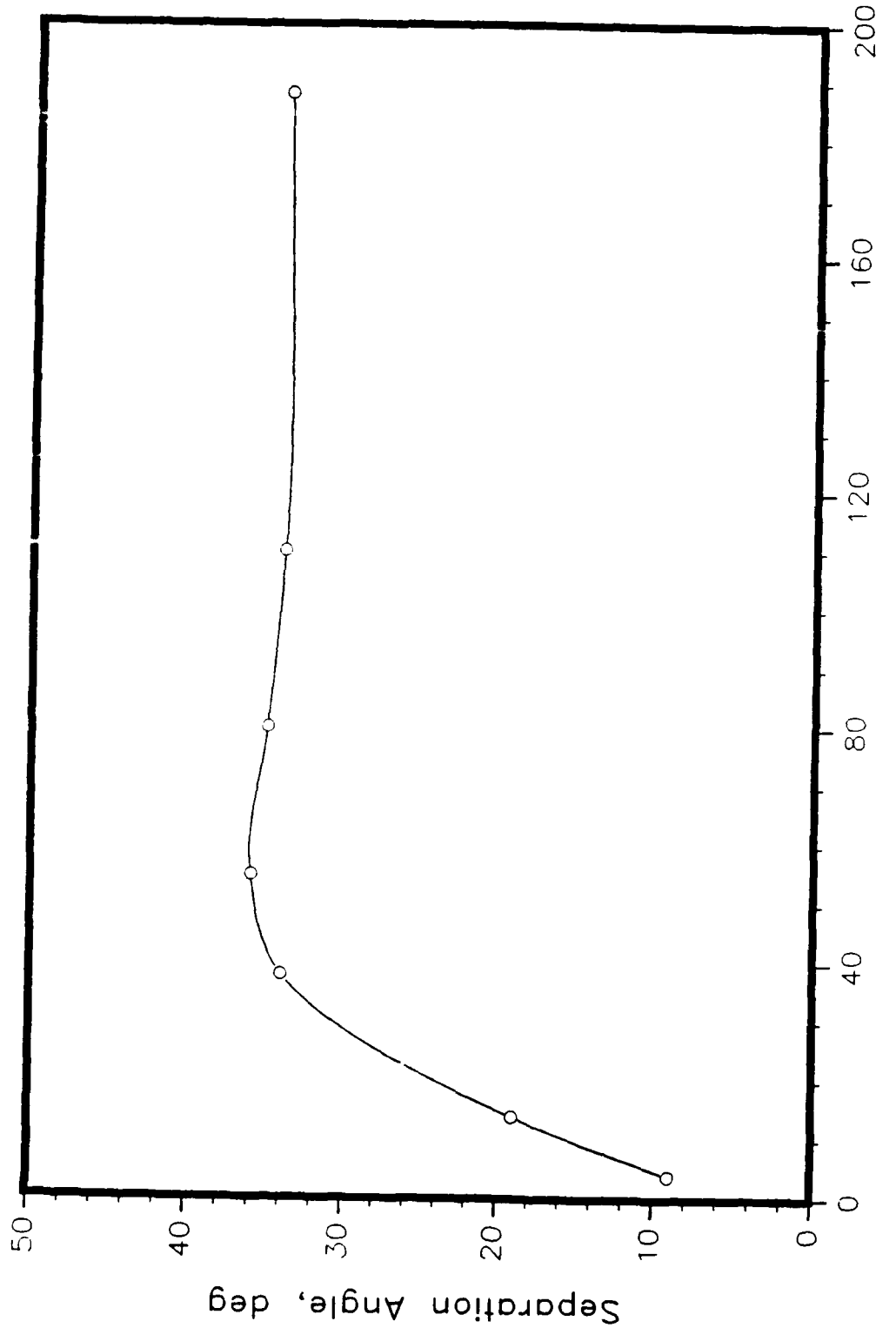

Figure 18: Flow Separation Angle in the 45° Half Nozzle

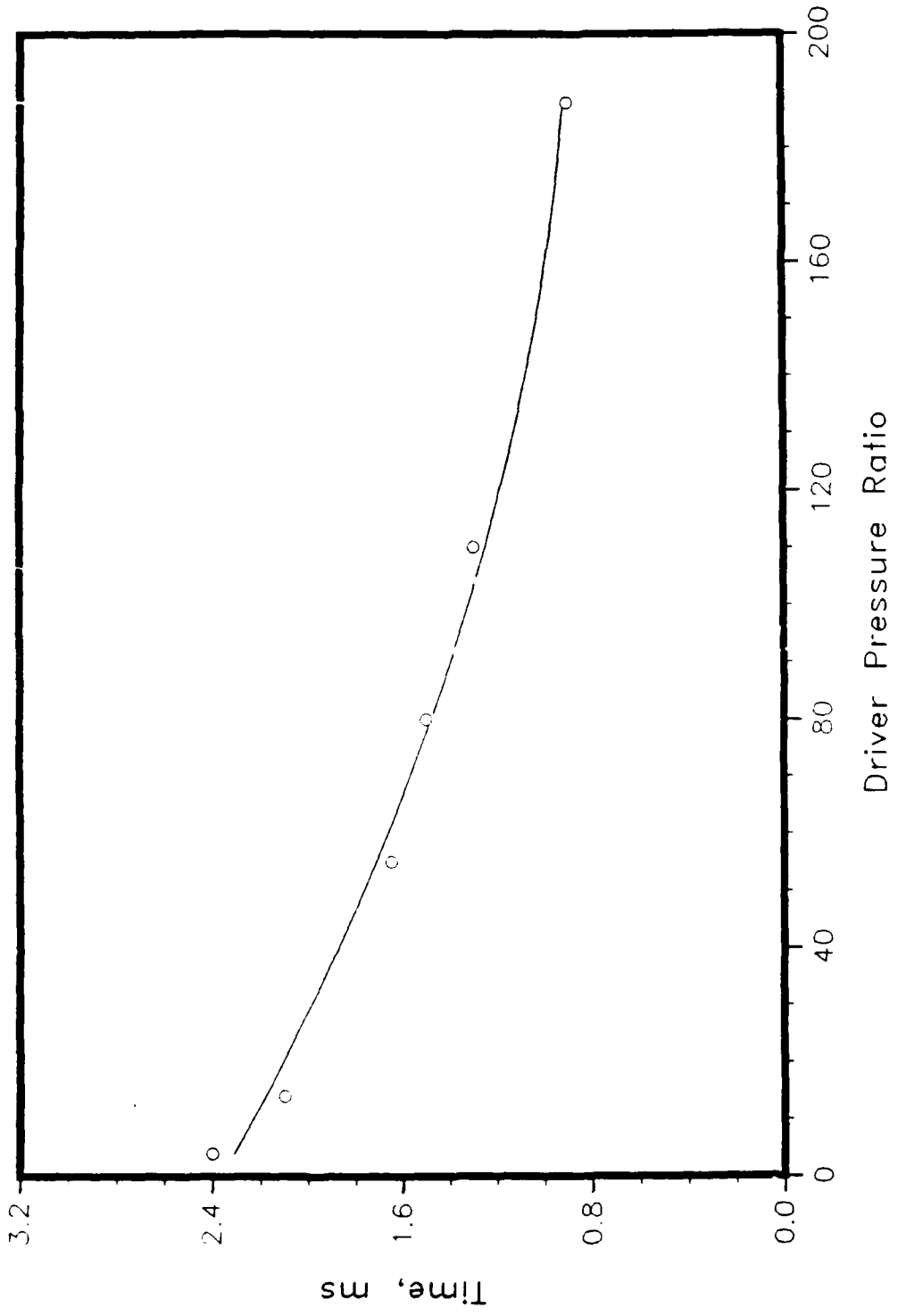

Figure 19: Flow Start-up Period for the 45° Half Nozzle

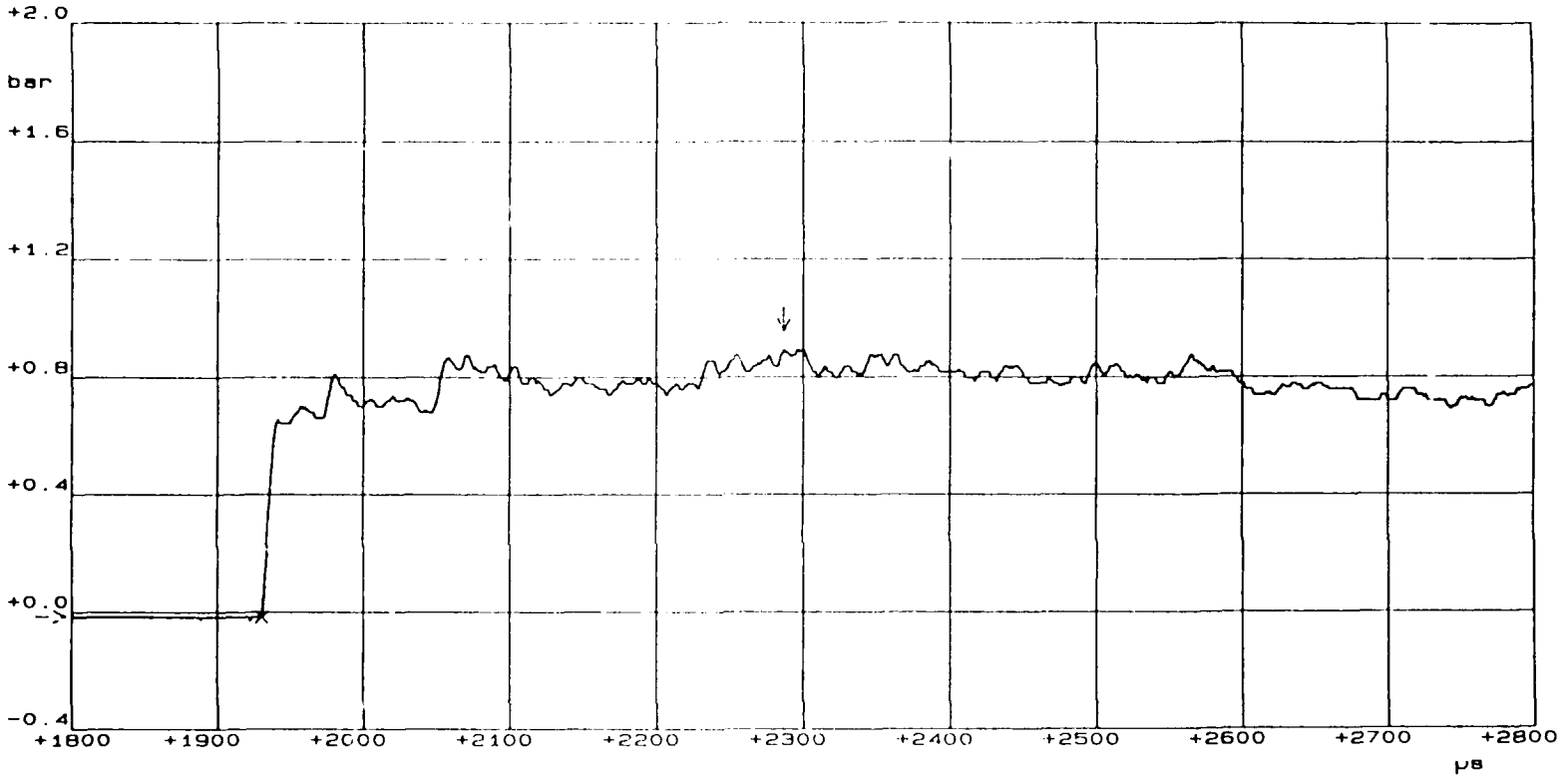

a) Driver-Pressure Ratio, P_{41} = 14

Figure 20: Pressure Histories at Gage # 2 for the 16° Half Nozzle

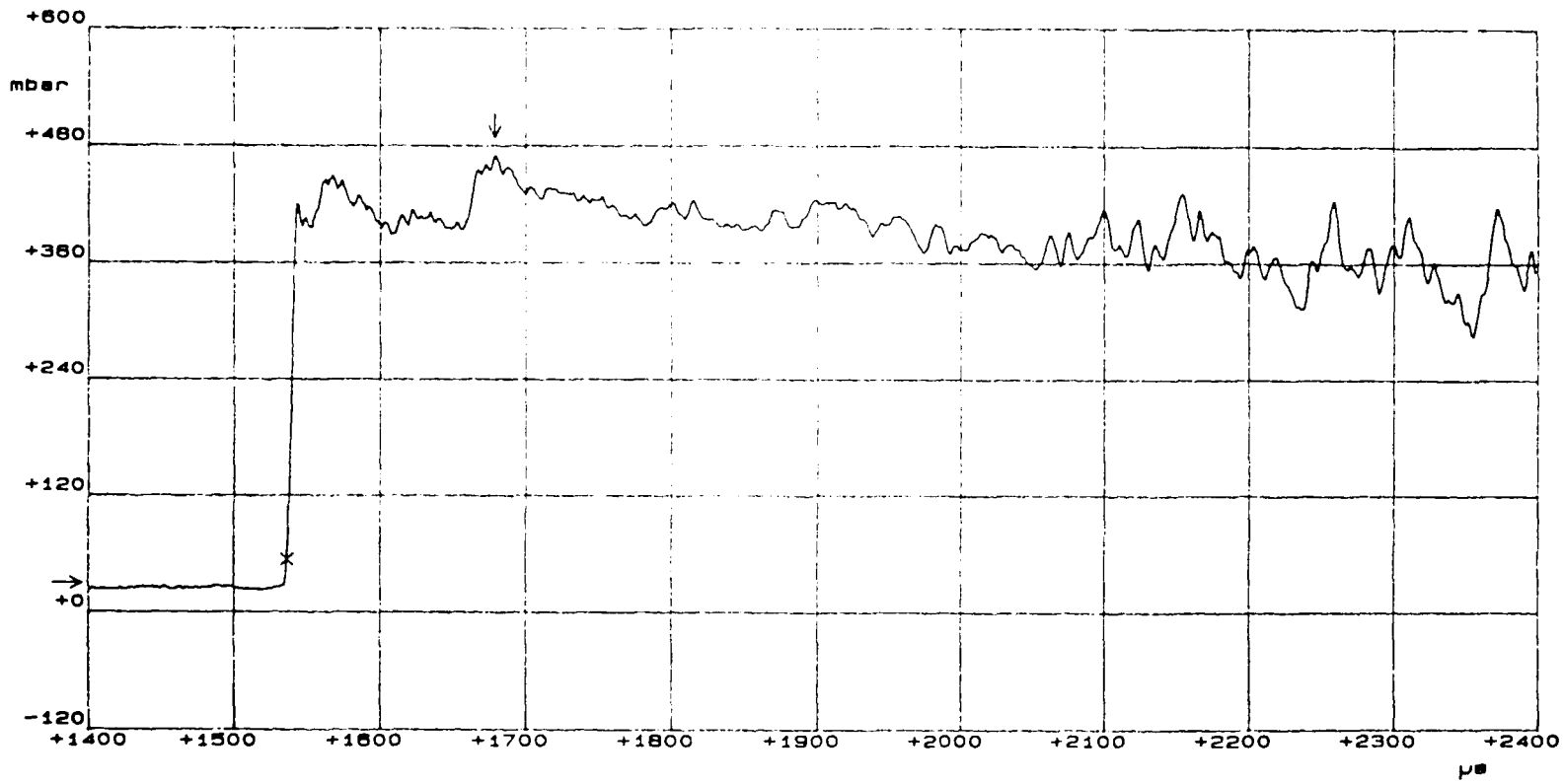

b) Driver-Pressure Ratio, $P_{41} = 80$

Figure 20: (continued)

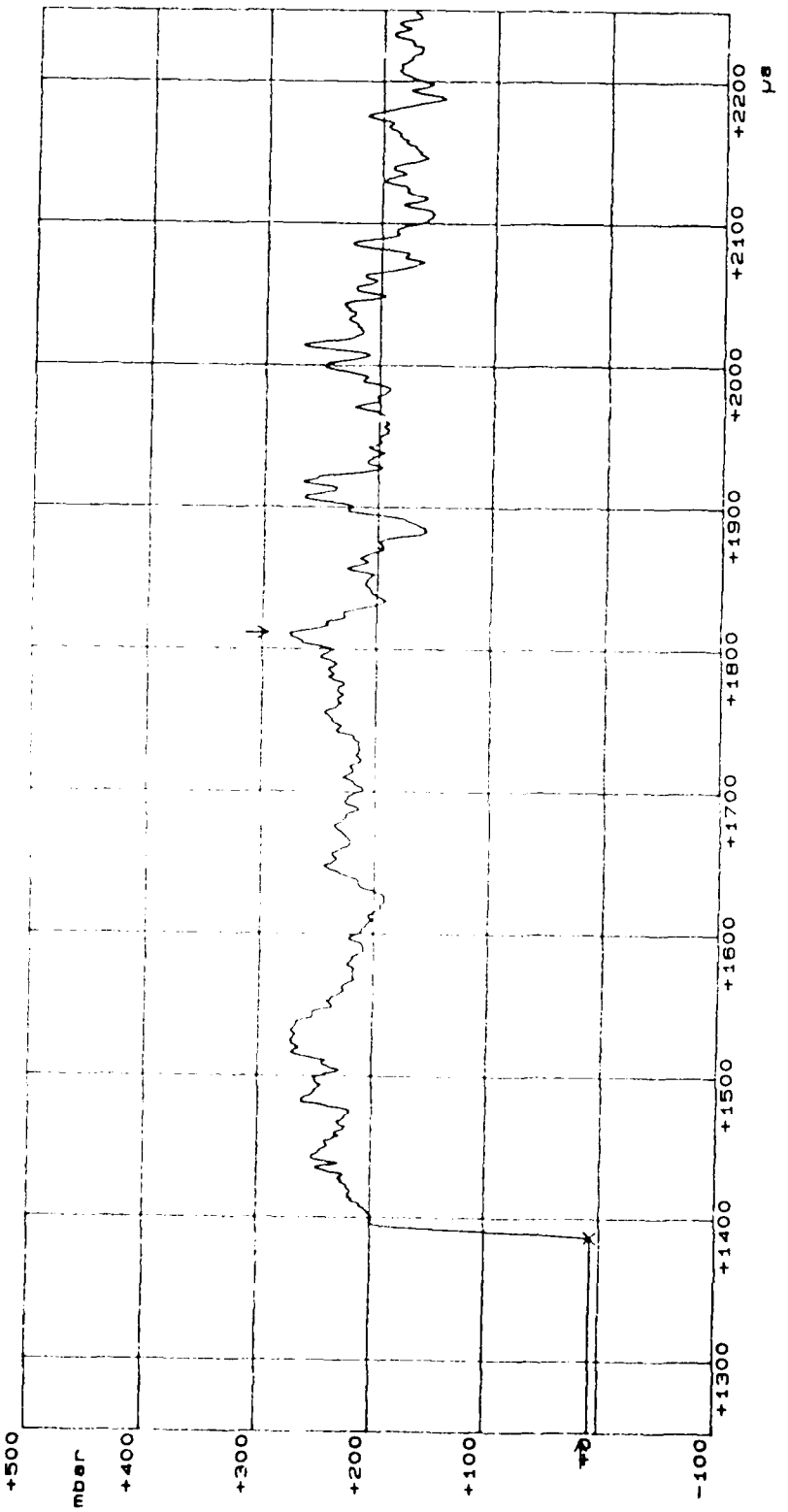

c) Driver-Pressure Ratio, P_{41} = 188

Figure 20: (concluded)

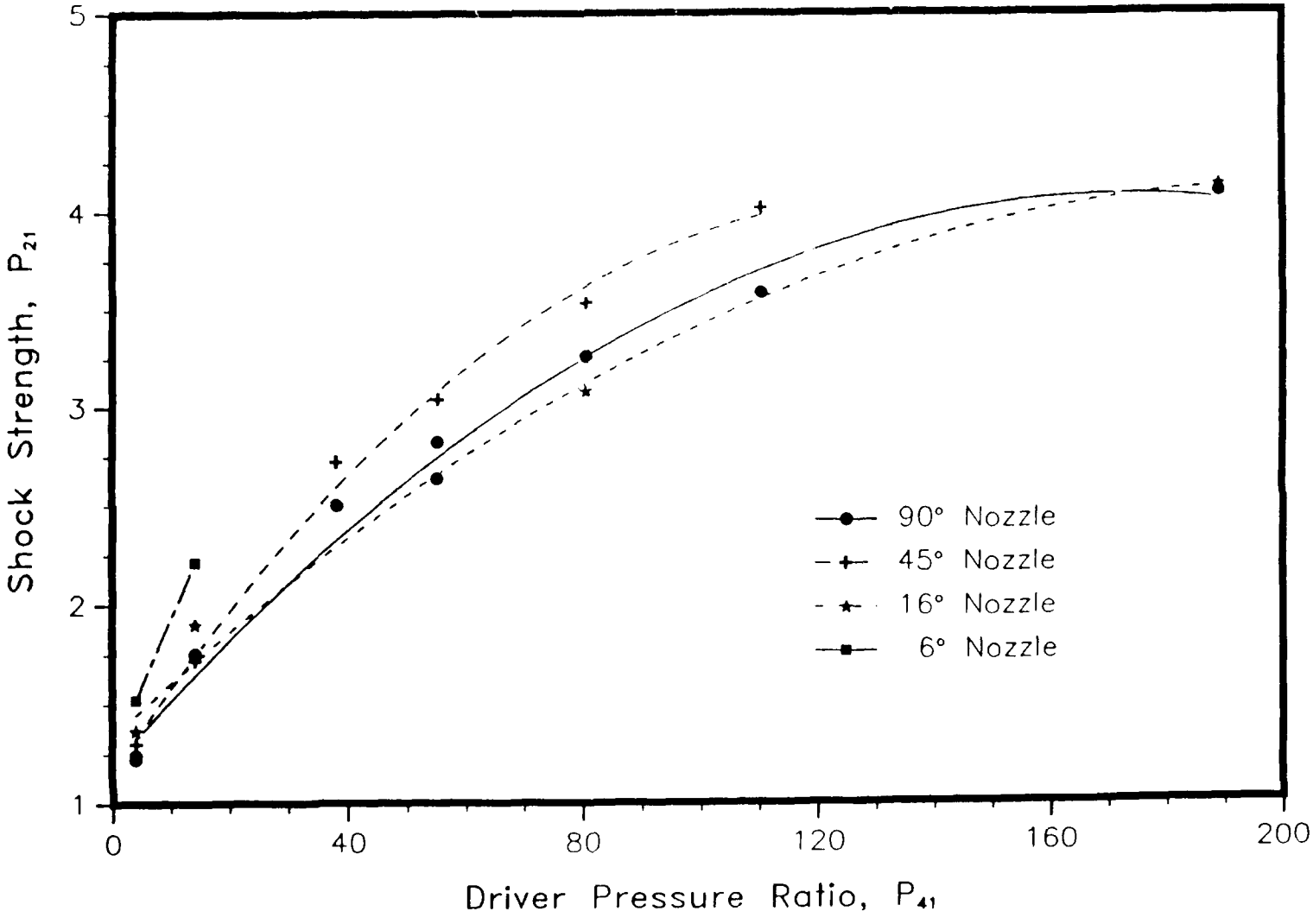

a) Gage # 1, 370 mm from Diaphragm Location

Figure 21: Shock Strength versus Driver-Pressure Ratio

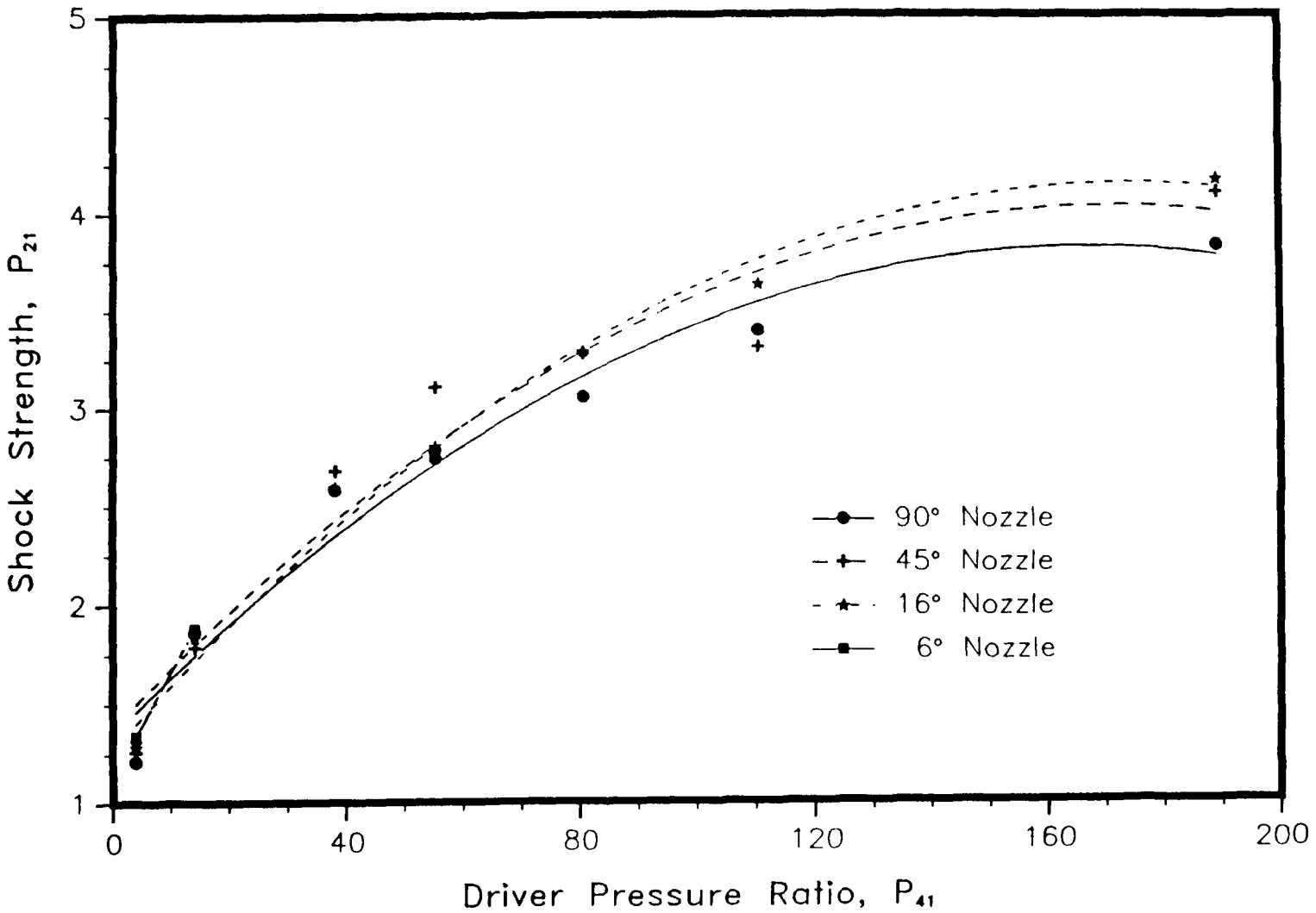

b) Gage #2, 860 mm from Diaphragm Location

Figure 21: (continued)

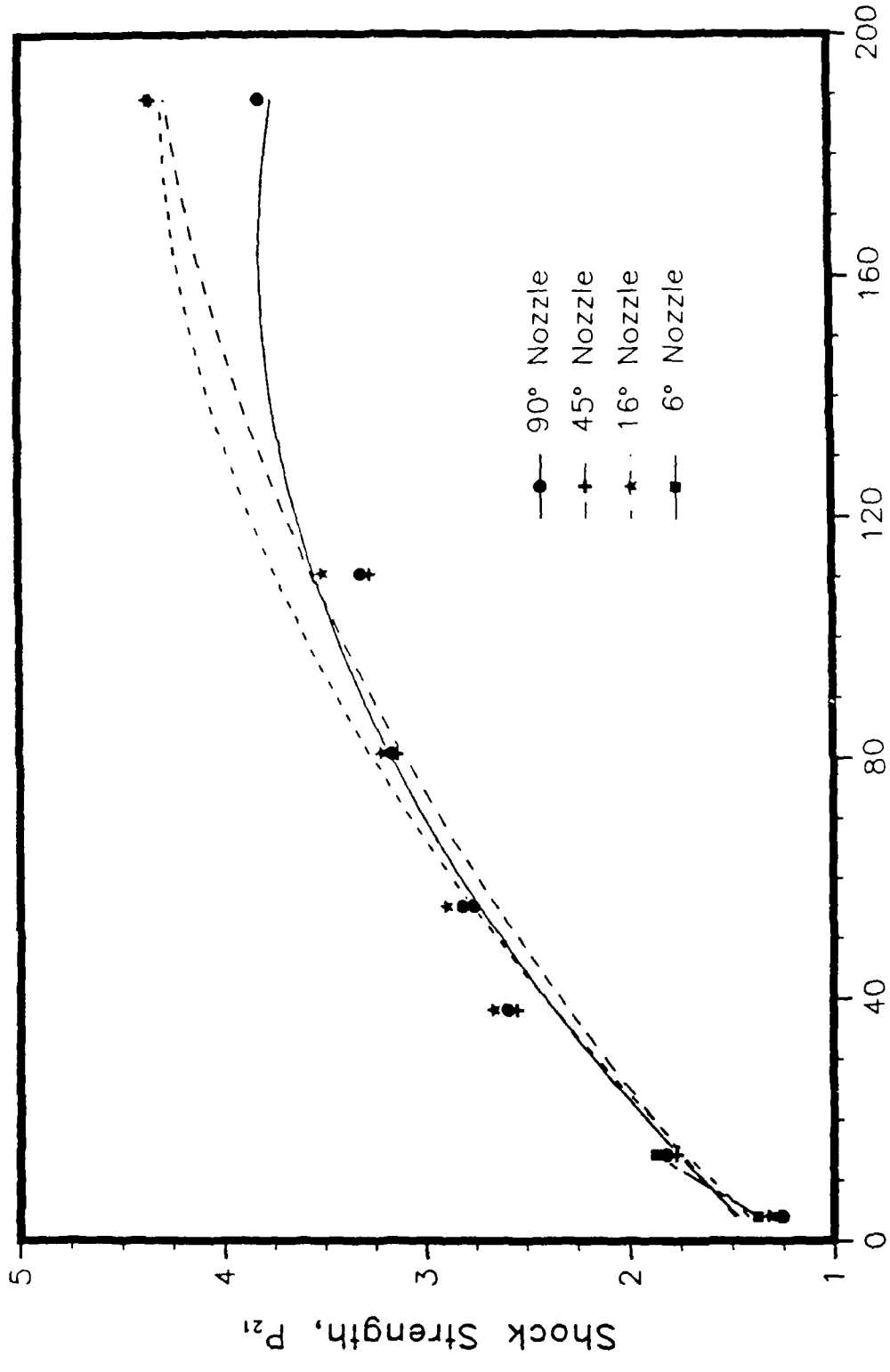

c) Gage # 3, 989 mm from Diaphragm Location

Figure 21: (concluded)

APPENDIX A

x-t DIAGRAMS

6° Nozzle

Driver Pressure Ratio 4

Shot No.13247 (100-300mm) Shot No.13248 (300-500mm)

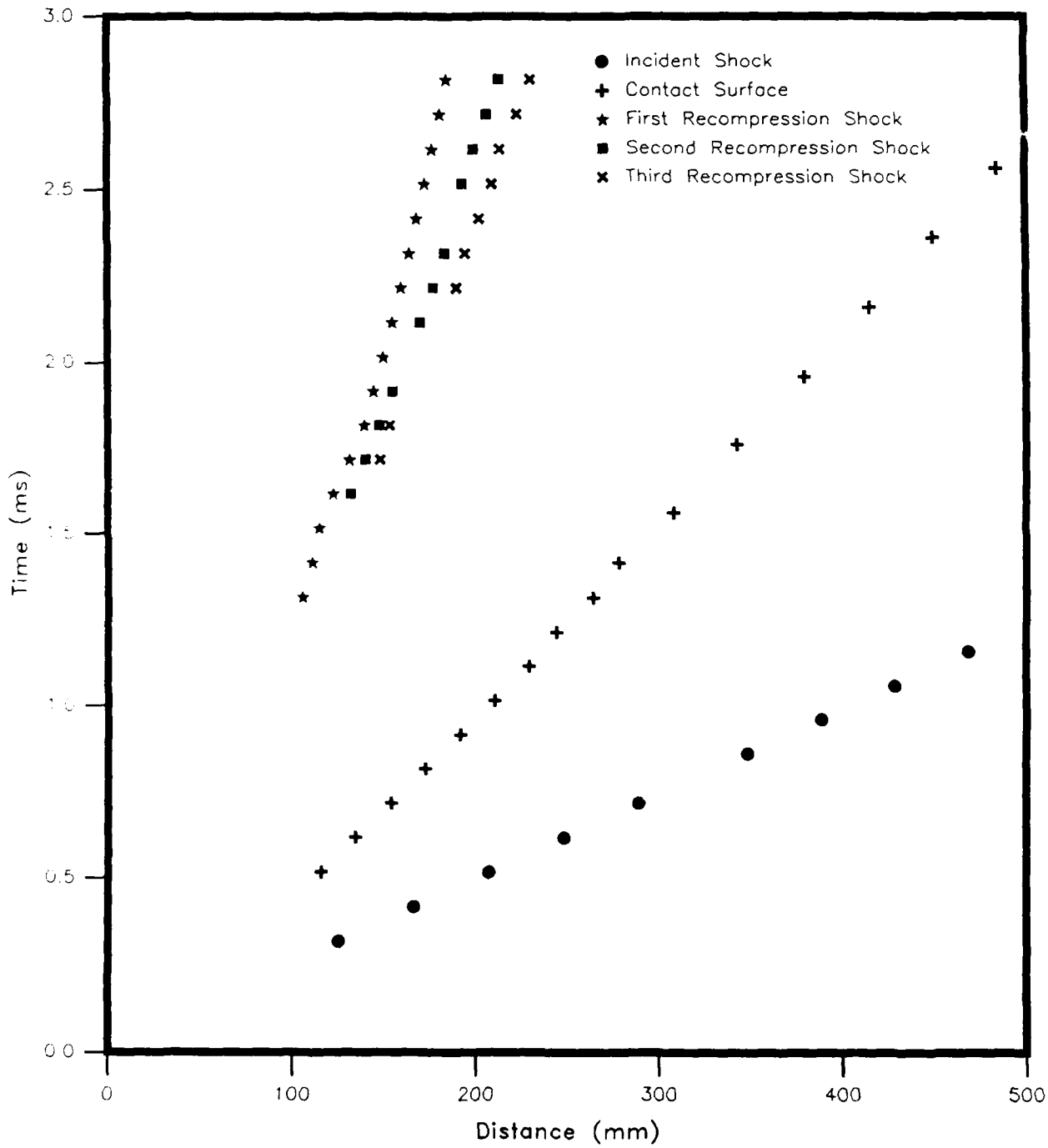

6° Nozzle

Driver Pressure Ratio 14

Shot No.13261 (0-200mm) Shot No.13262 (300-500mm)

Shot No.13263 (200-400mm)

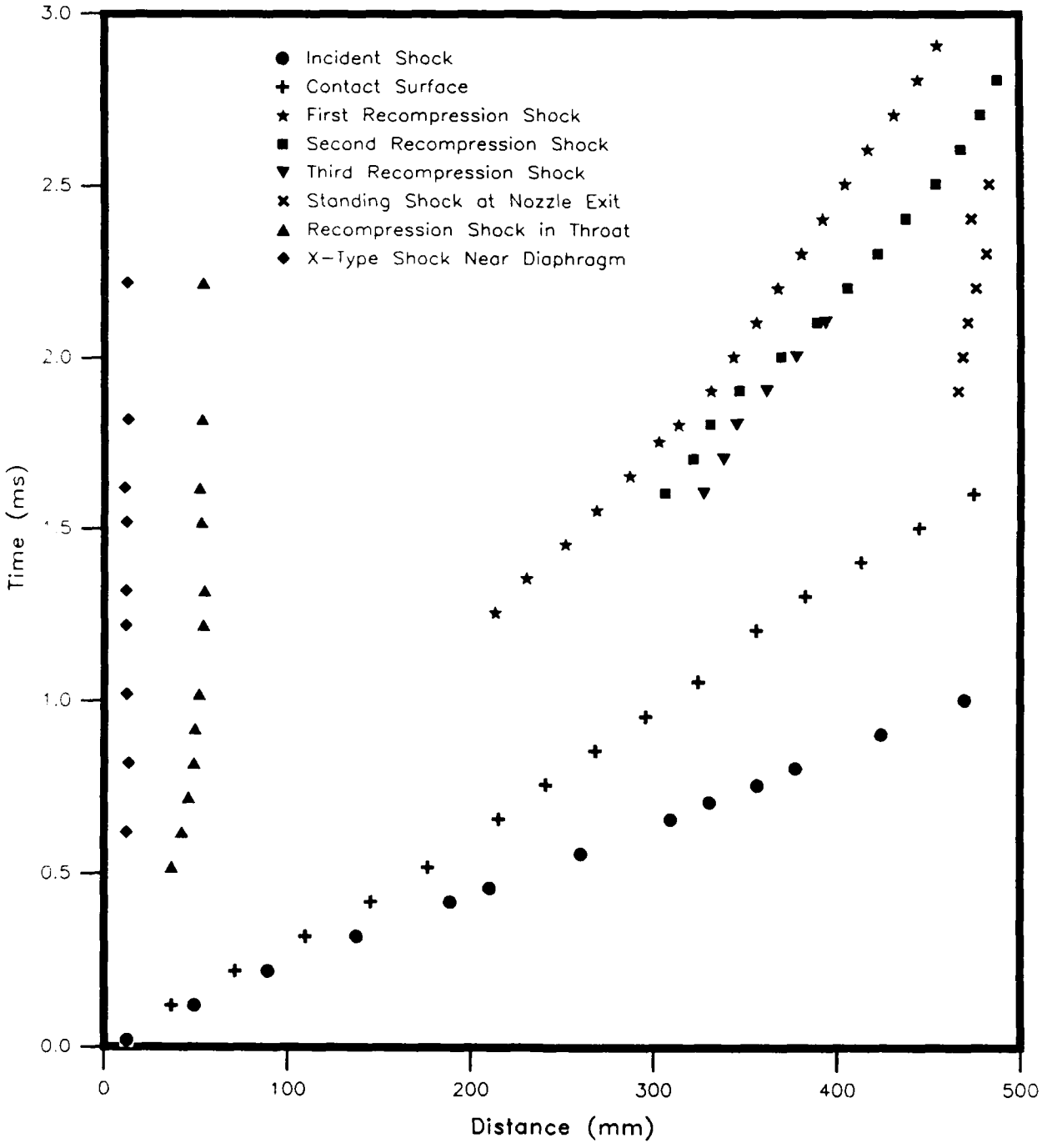

6° Nozzle

Driver Pressure Ratio 38

Shot No.13327 (300–500mm)

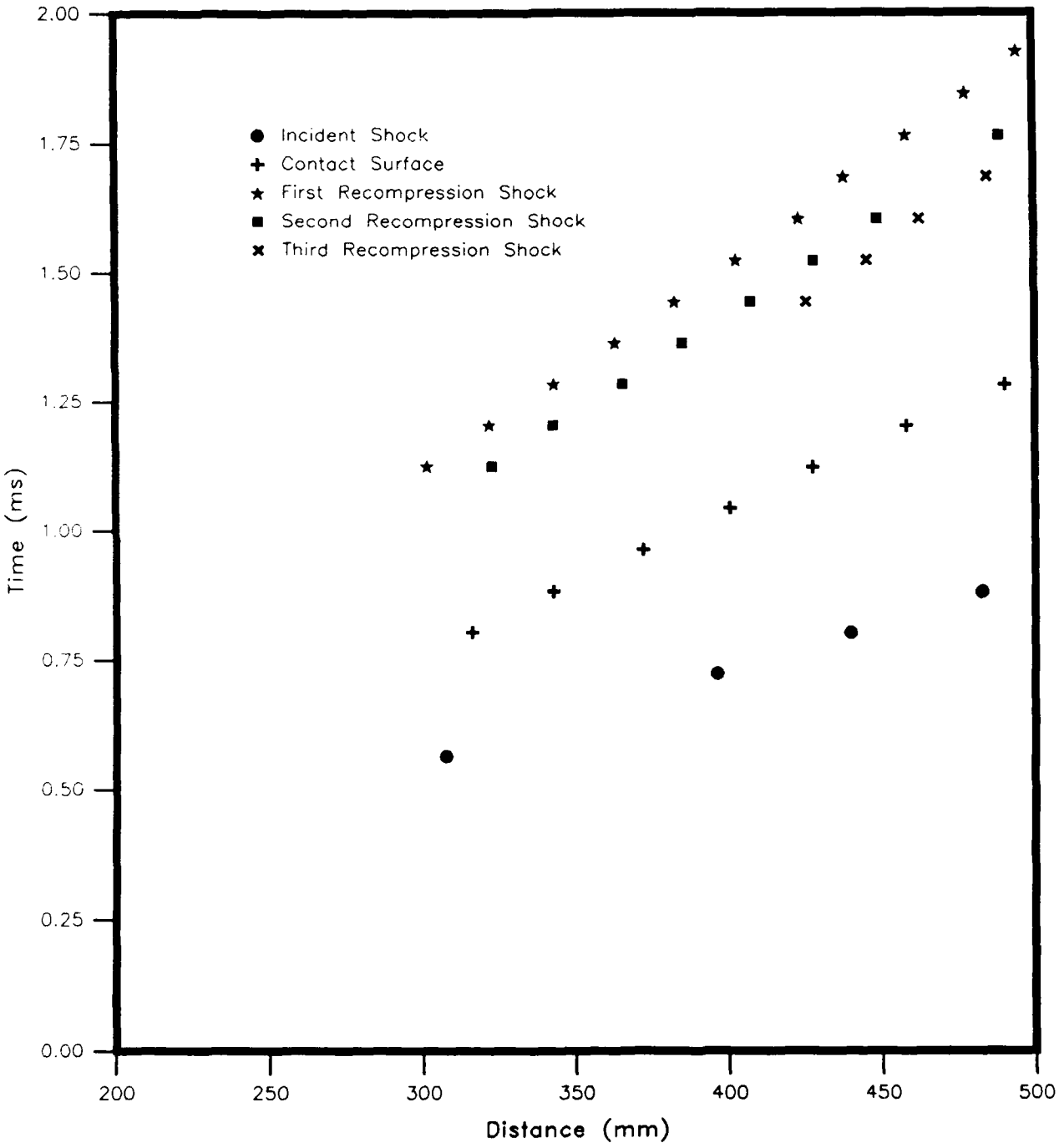

6° Nozzle

Driver Pressure Ratio 55

Shot No.13328 (300–500mm)

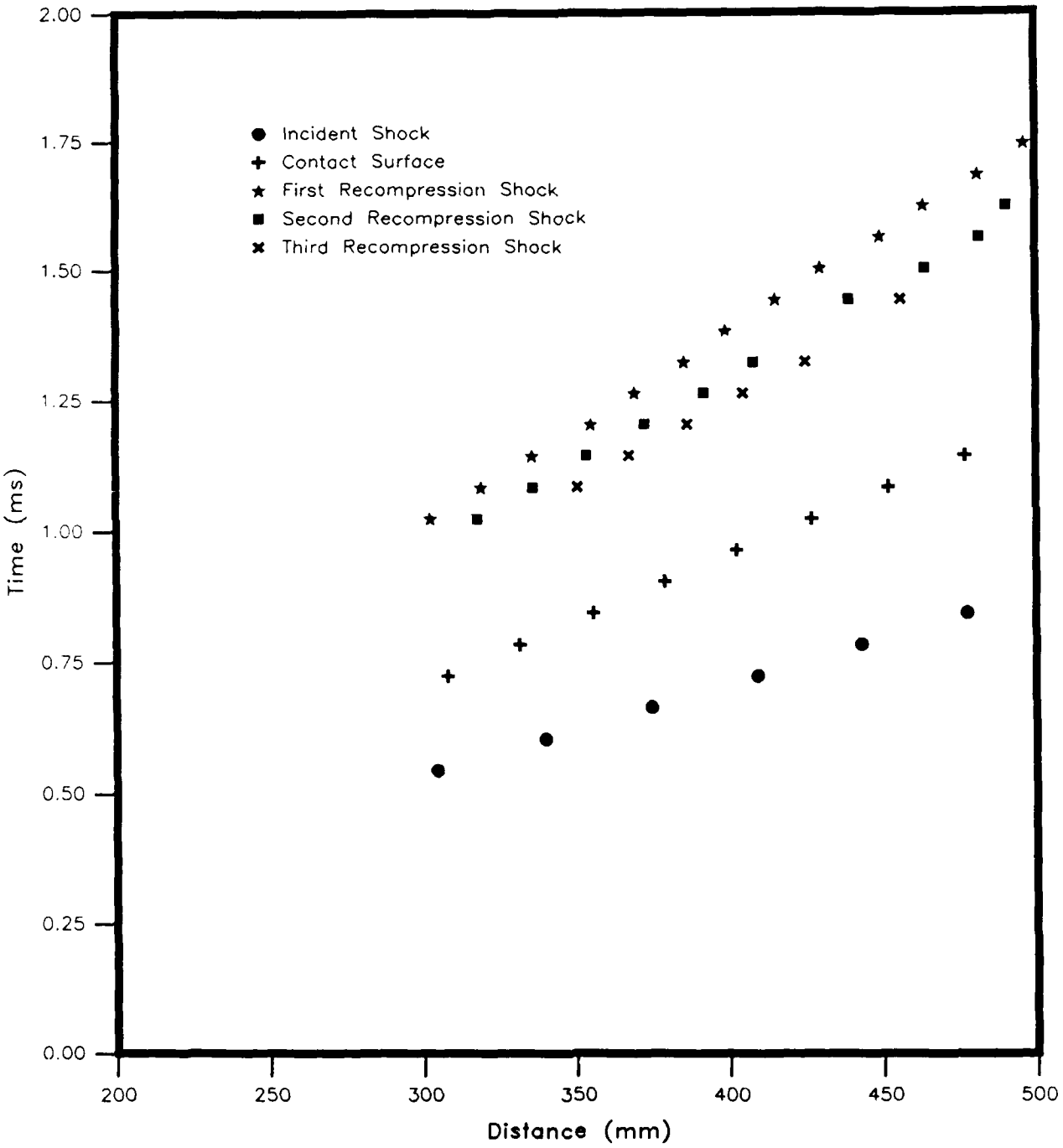

6° Nozzle

Driver Pressure Ratio 80

Shot No.13329 (300–500mm)

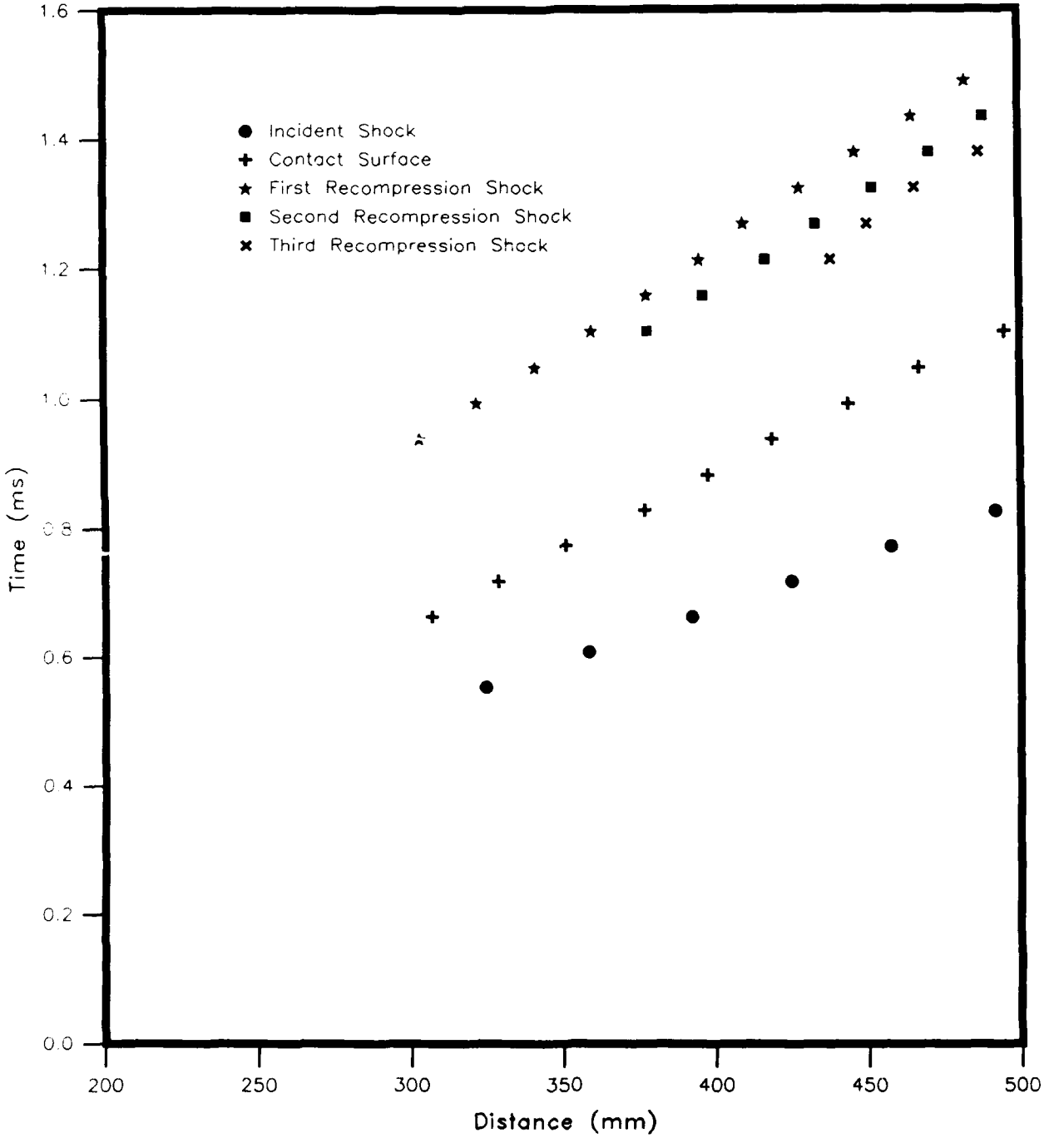

6° Nozzle

Driver Pressure Ratio 110

Shot No.13330 (300-500mm)

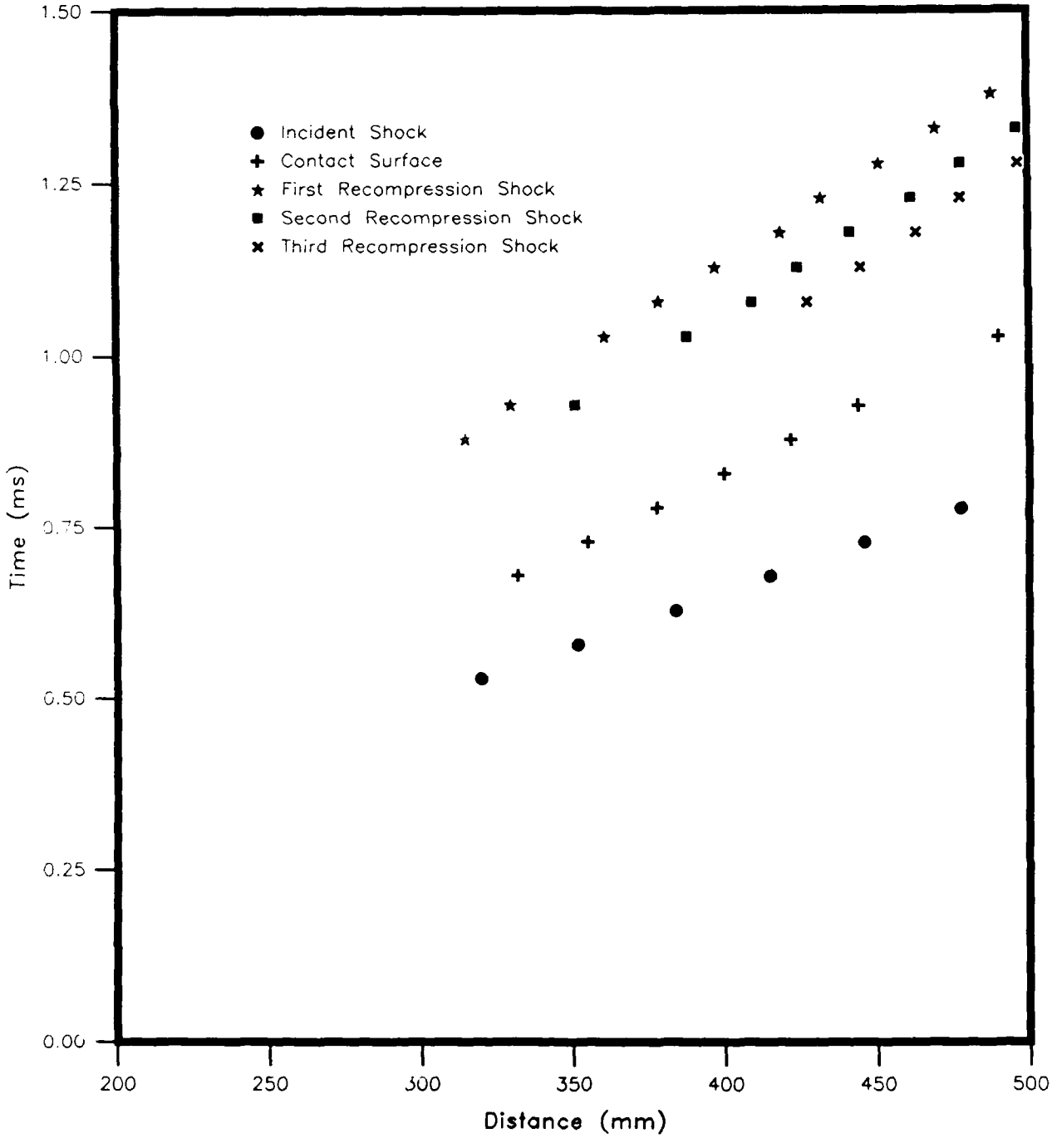

6° Nozzle

Driver Pressure Ratio 188

Shot No.13331 (300-500mm)

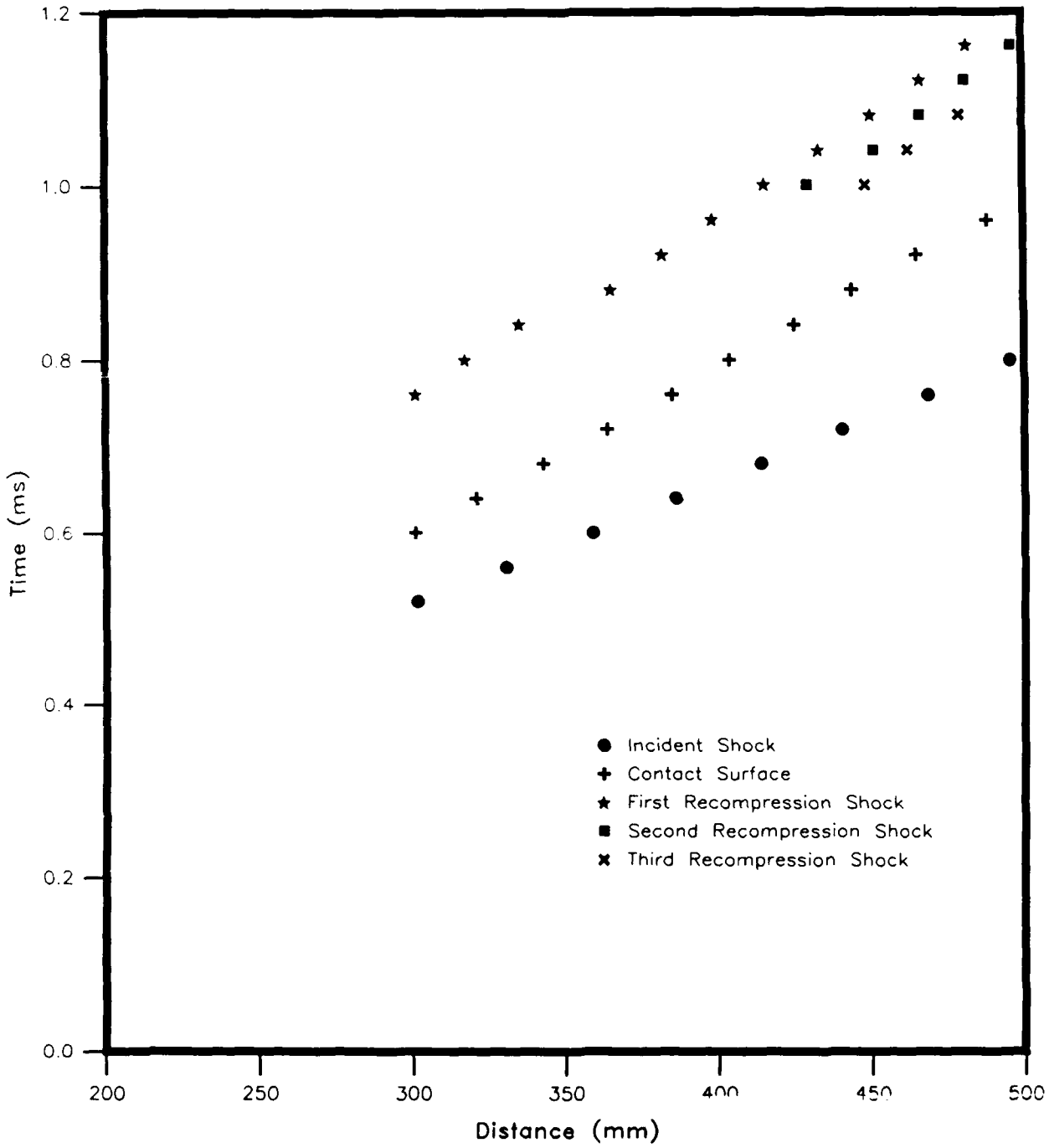

16° Nozzle

Driver Pressure Ratio 4

Shot No.13245 (0–200mm) Shot N0.13246 (200–400mm)

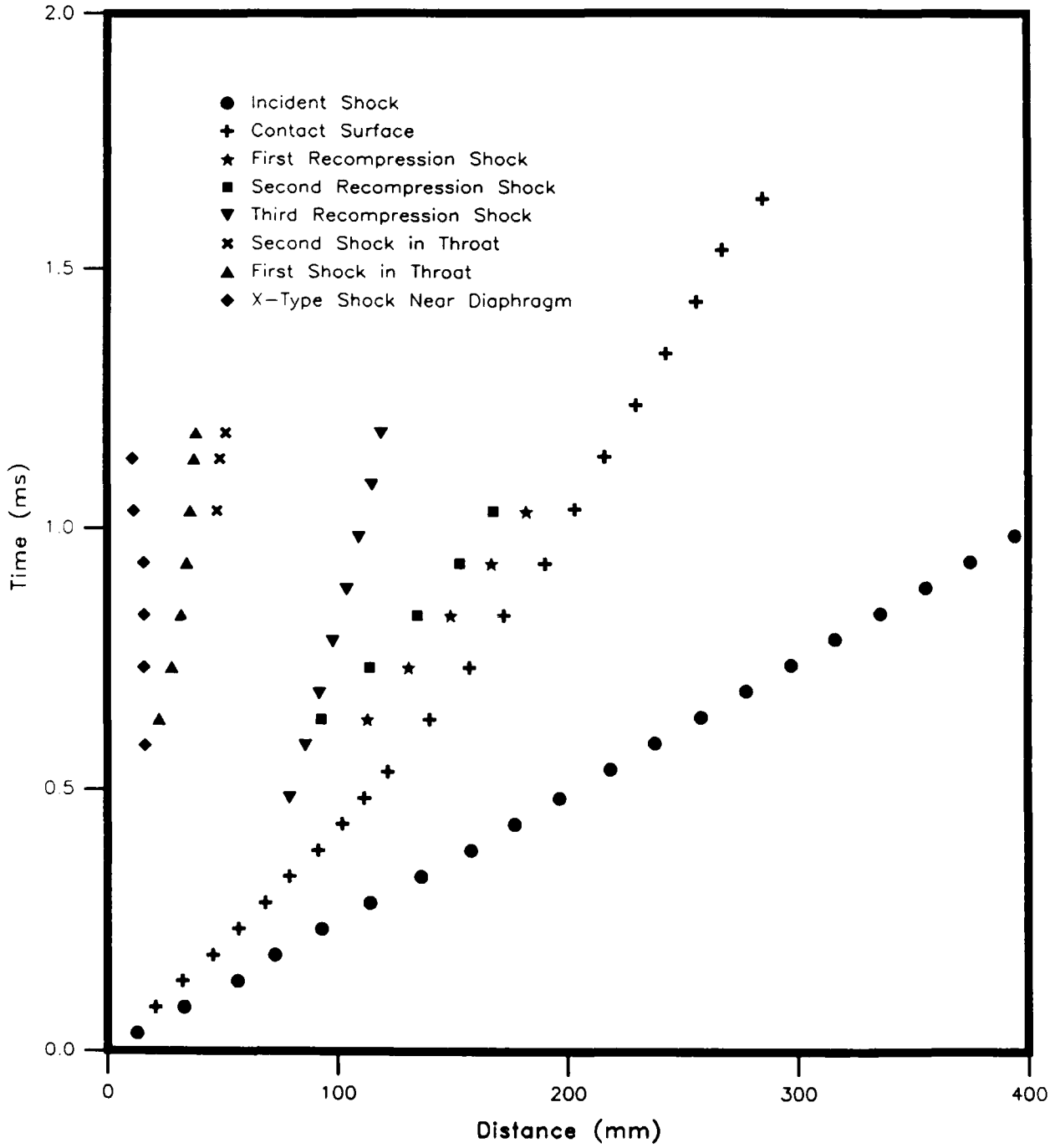

16° Nozzle

Driver Pressure Ratio 14

Shot No.13260 (0–200mm) Shot N0.13264 (200–400mm)

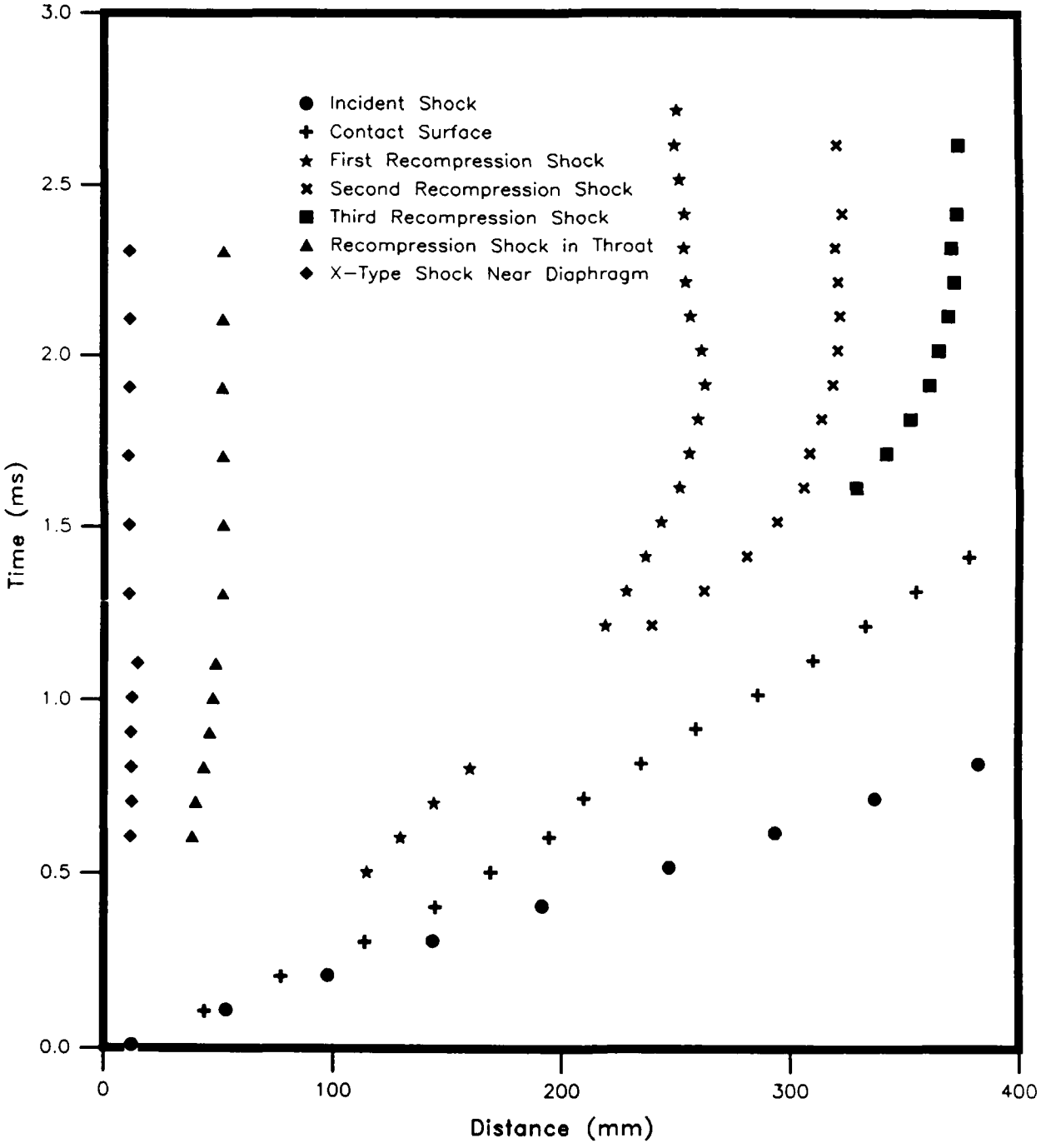

16° Nozzle

Driver Pressure Ratio 38

Shot No.13317 (0-200mm) Shot N0.13322 (200-400mm)

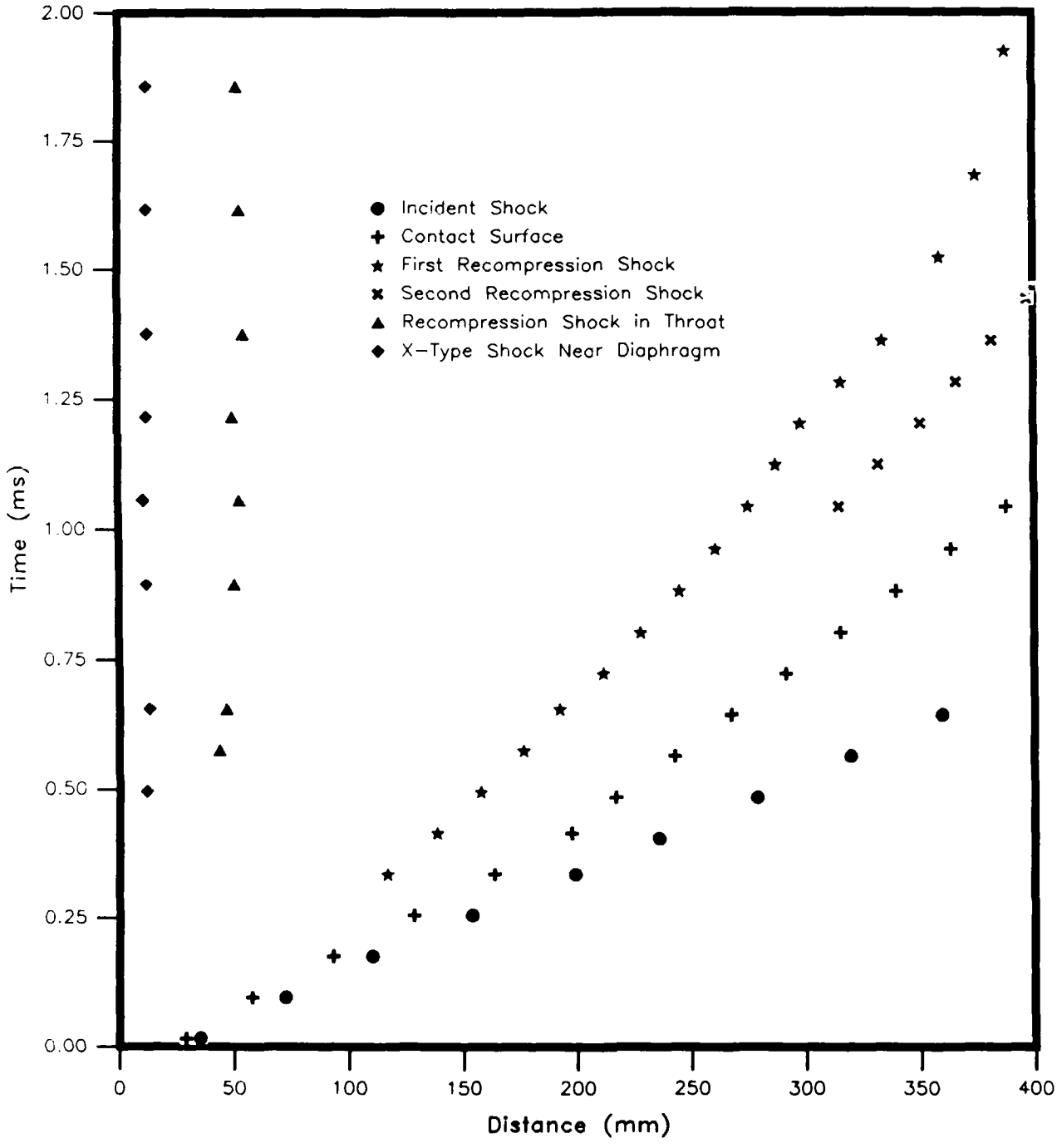

16° Nozzle

Driver Pressure Ratio 55

Shot No.13304 (0–200mm) Shot N0.13323 (200–400mm)

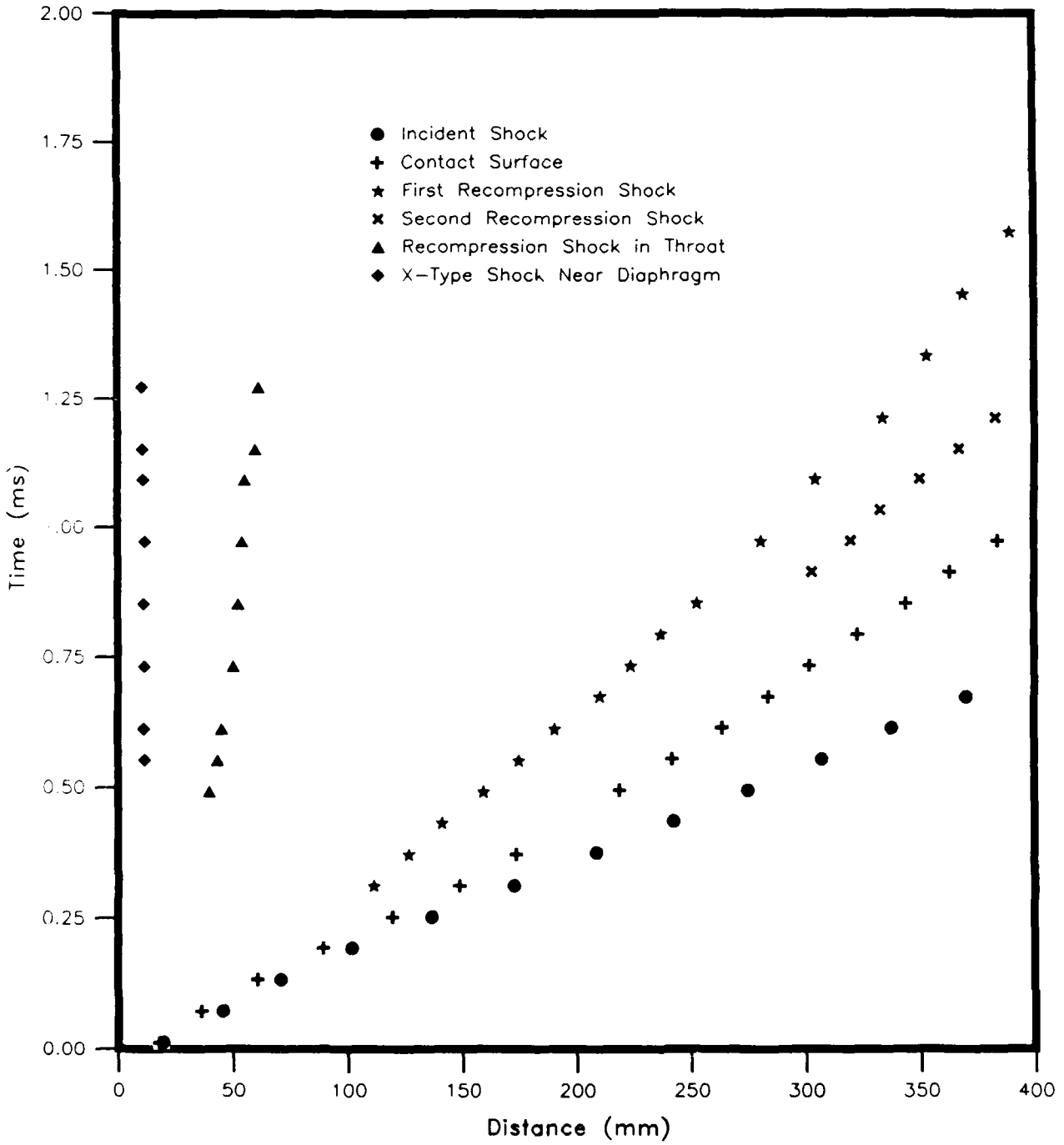

16° Nozzle

Driver Pressure Ratio 80

Shot No.13316 (0–200mm) Shot N0.13324 (200–400mm)

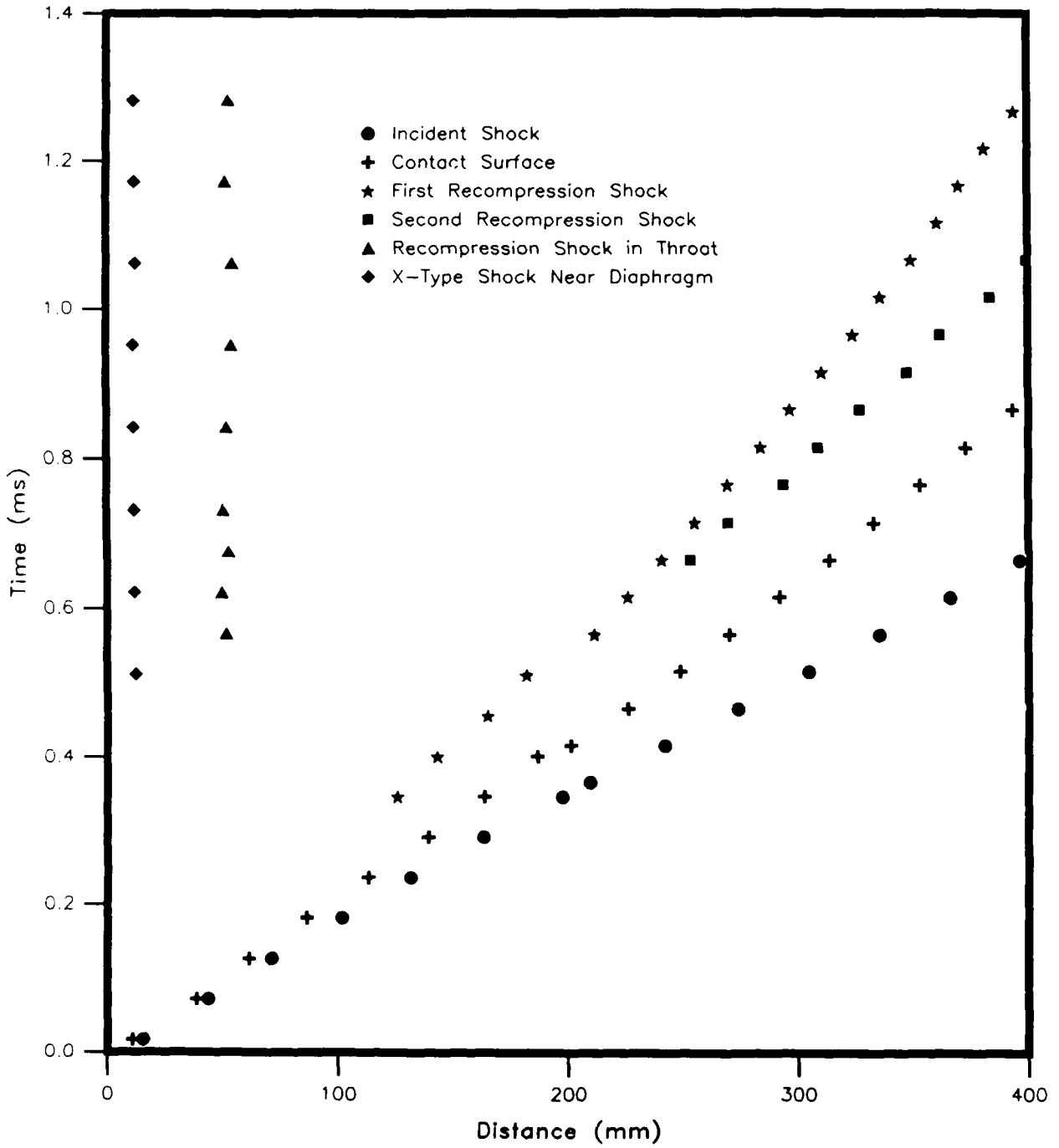

16° Nozzle

Driver Pressure Ratio 110

Shot No.13305 (0–200mm) Shot N0.13325 (200–400mm)

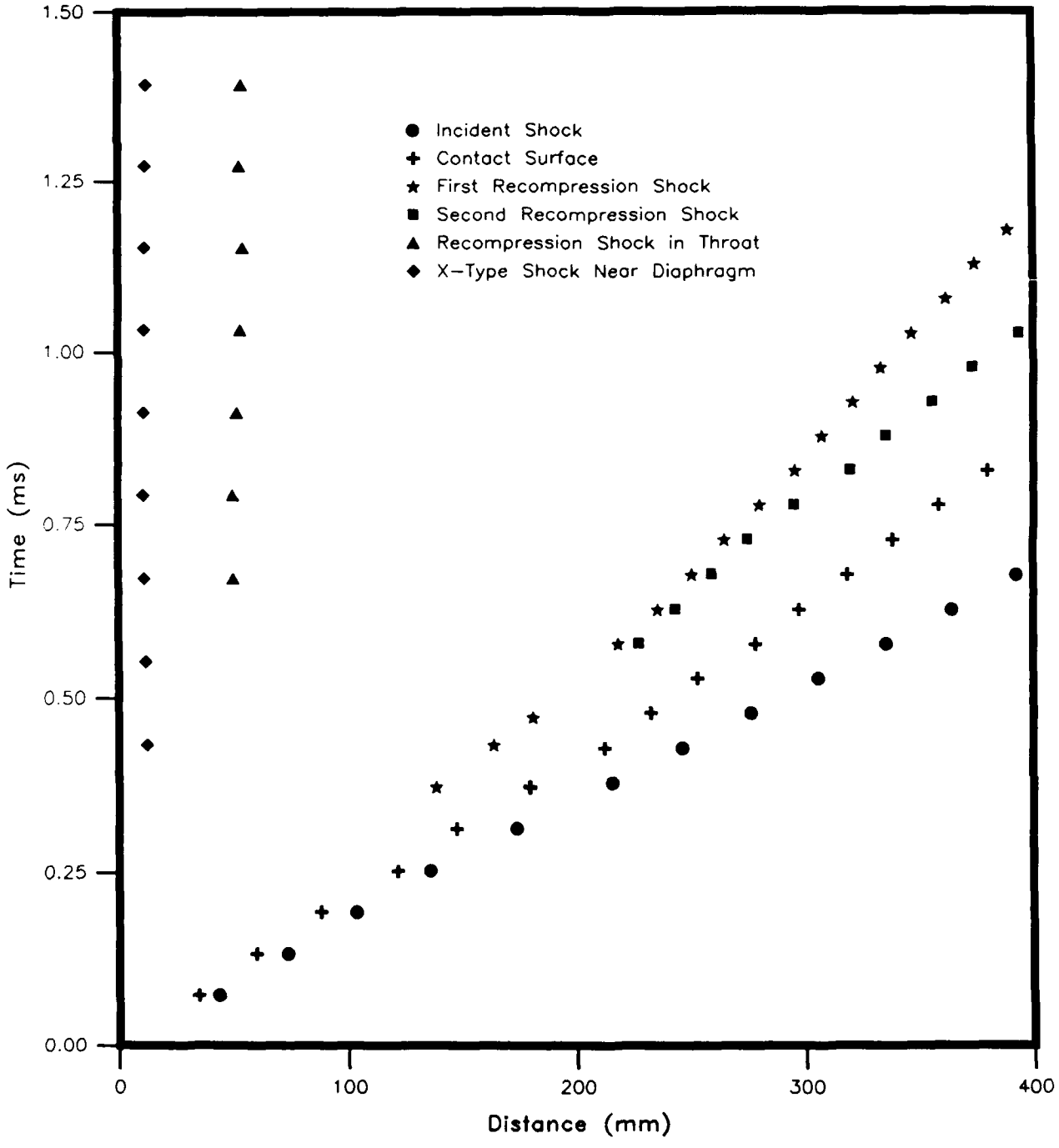

16° Nozzle

Driver Pressure Ratio 188

Shot No.13315 (0–200mm) Shot N0.13326 (200–400mm)

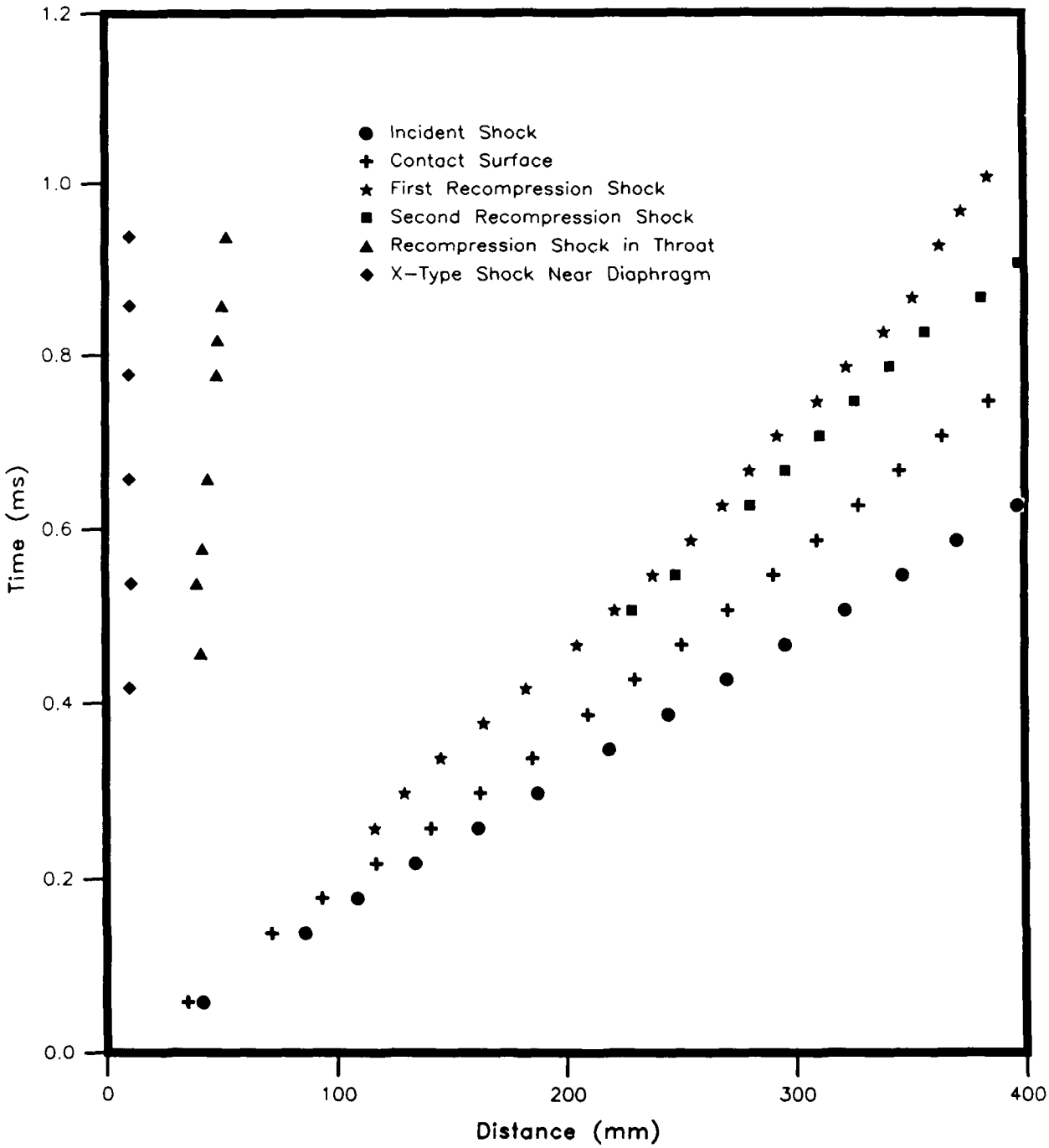

45° Nozzle

Driver Pressure Ratio 4

Shot No.13244 & 13253 (0-200mm)

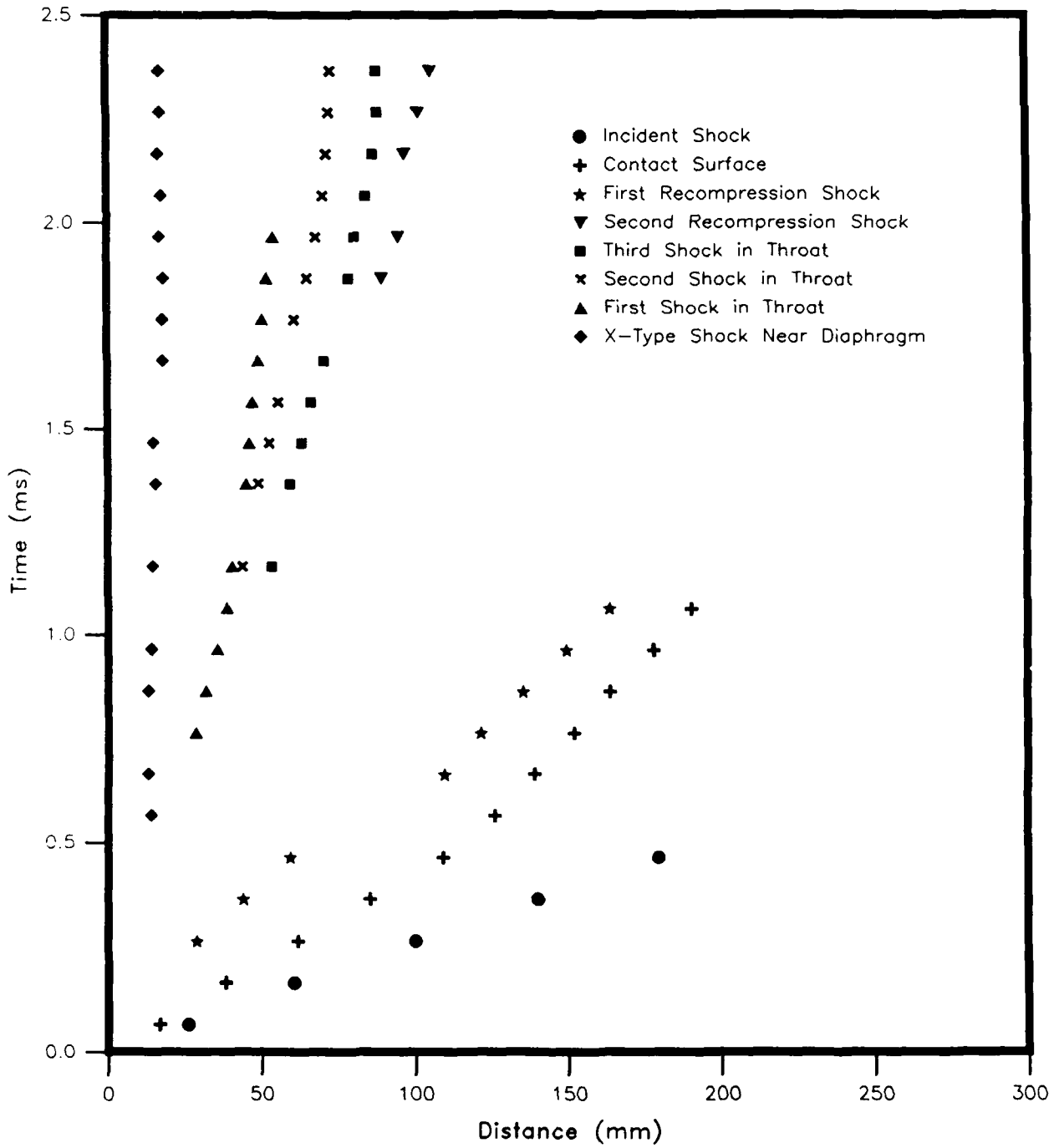

45° Nozzle

Driver Pressure Ratio 14

Shot No.13244 (0–200mm) Shot No.13253 (100–300mm)

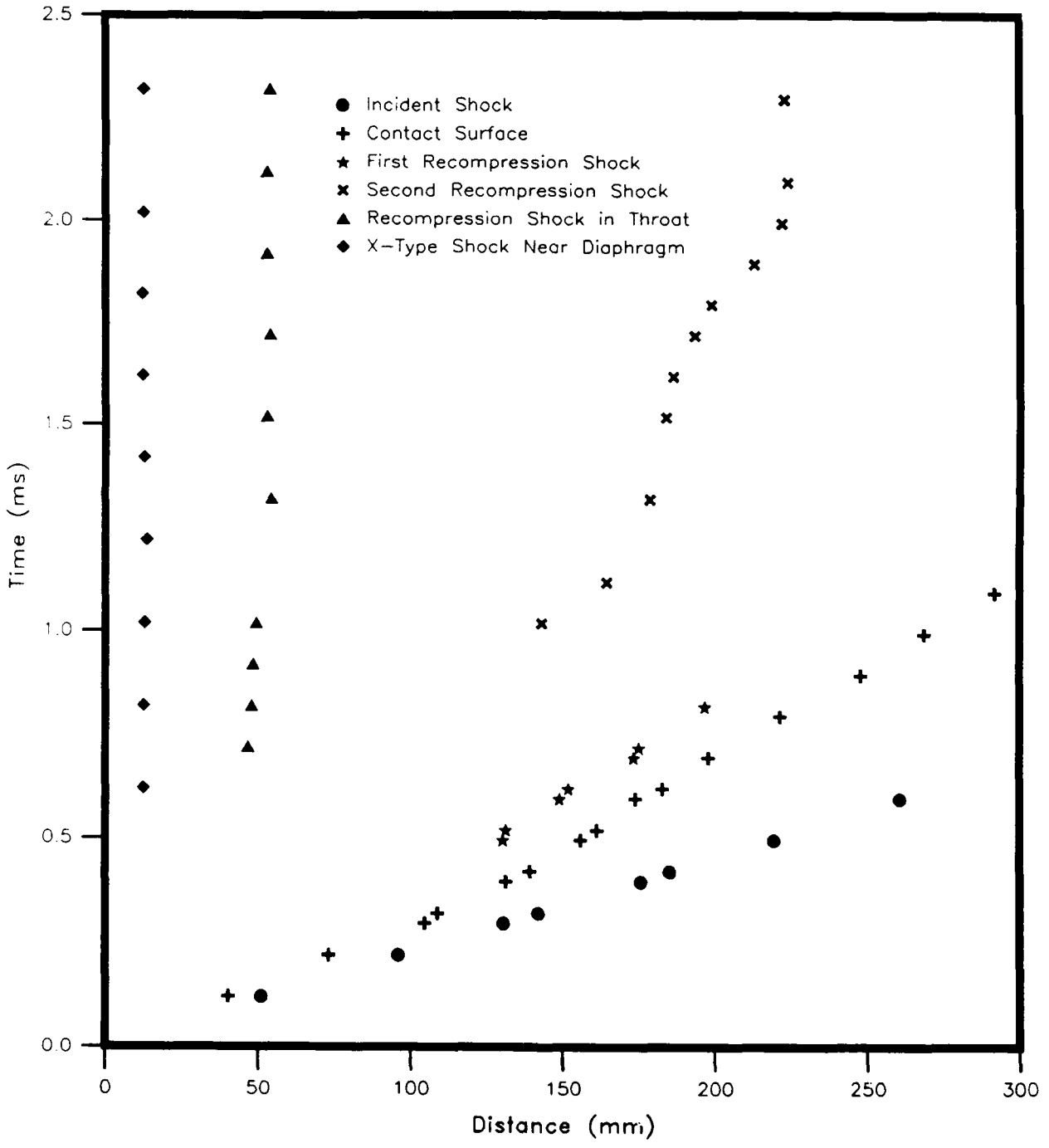

45° Nozzle

Driver Pressure Ratio 38

Shot No.13309 (0-200mm)

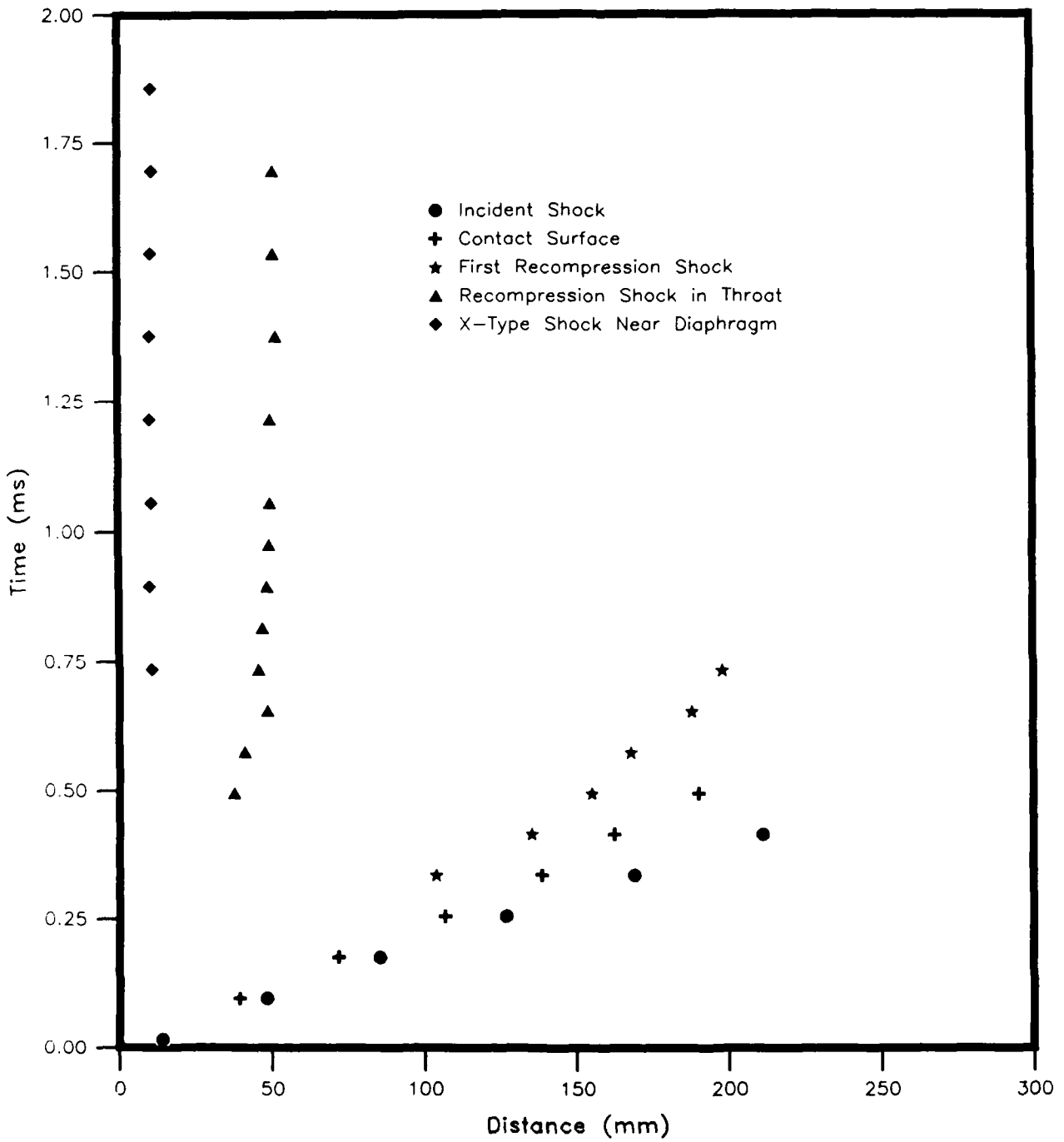

45° Nozzle

Driver Pressure Ratio 55

Shot No.13303 (0–200mm) Shot No.13321 (100–300mm)

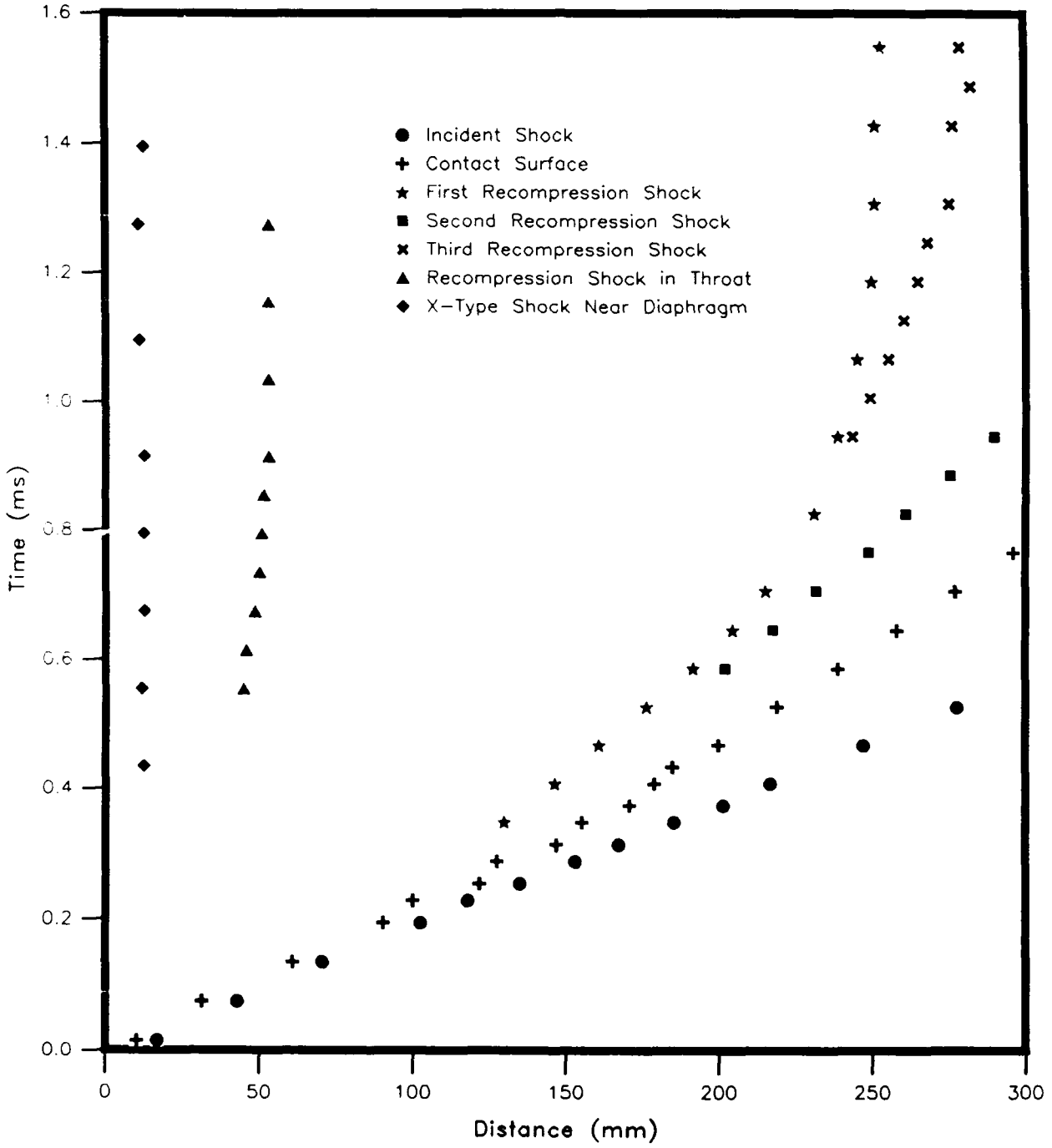

45° Nozzle

Driver Pressure Ratio 80

Shot No.13308 (0–200mm) Shot No.13319 (100–300mm)

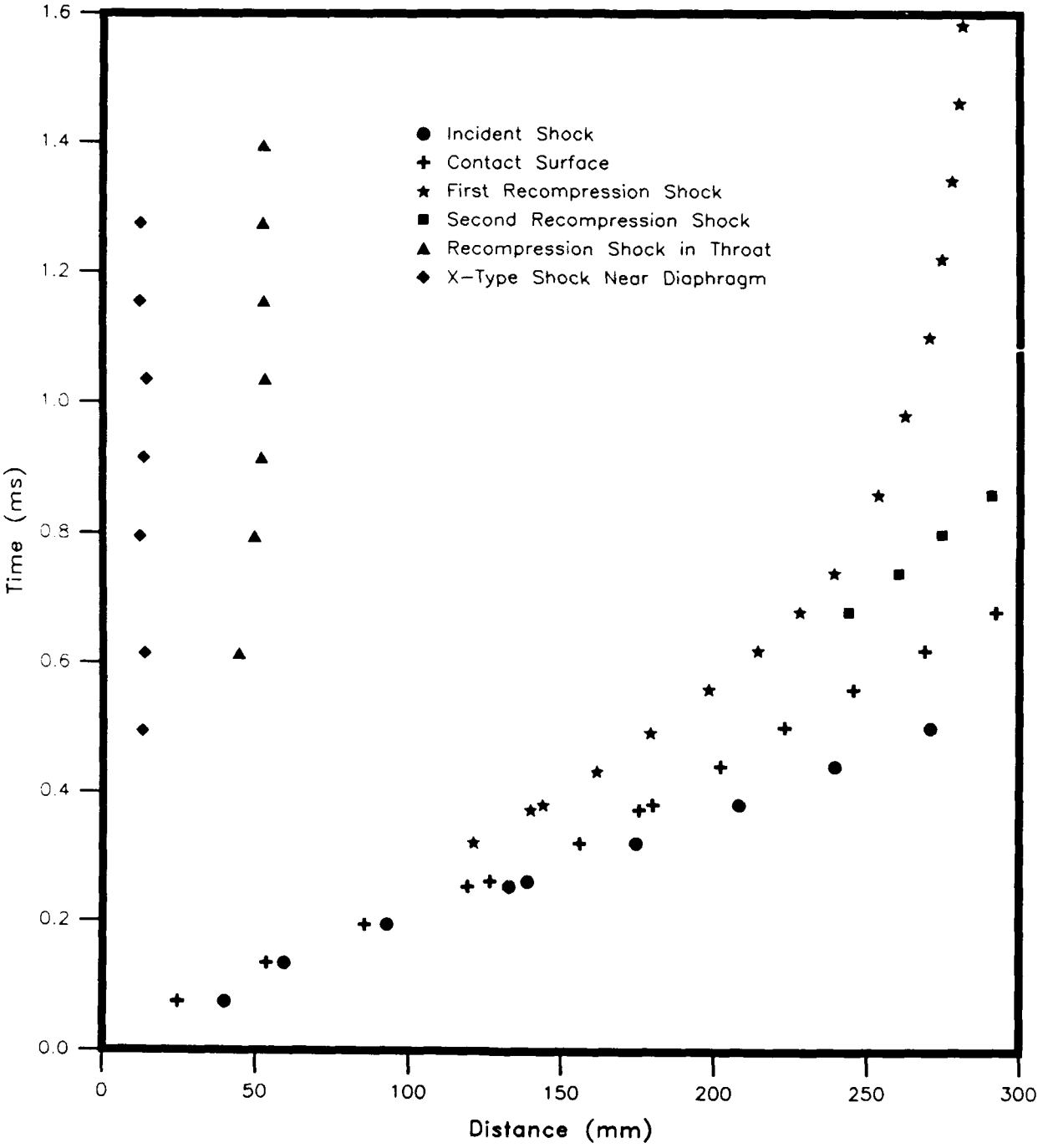

45° Nozzle

Driver Pressure Ratio 110

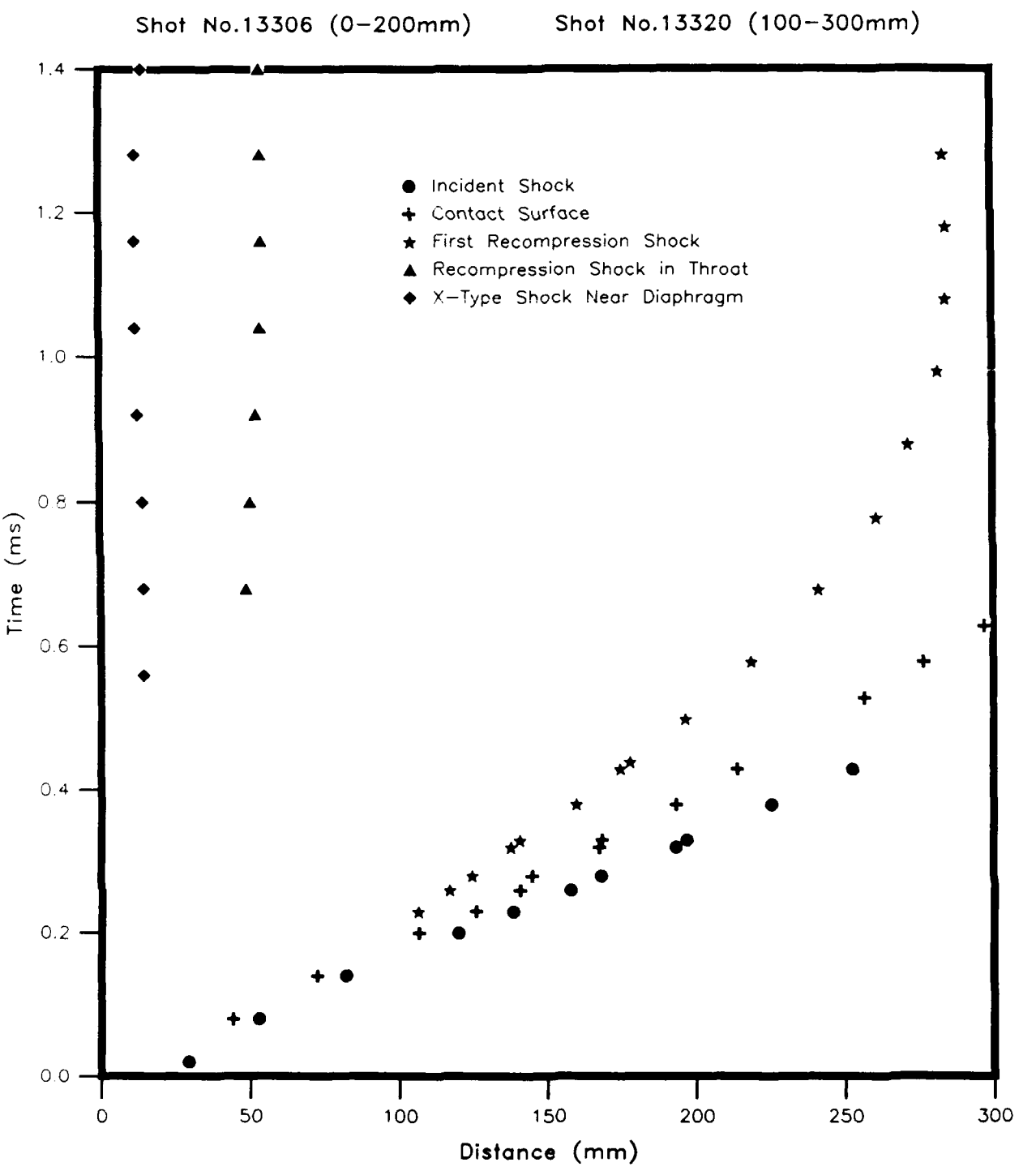

45° Nozzle

Driver Pressure Ratio 188

Shot No.13307 (0–200mm) Shot No.13318 (100–300mm)

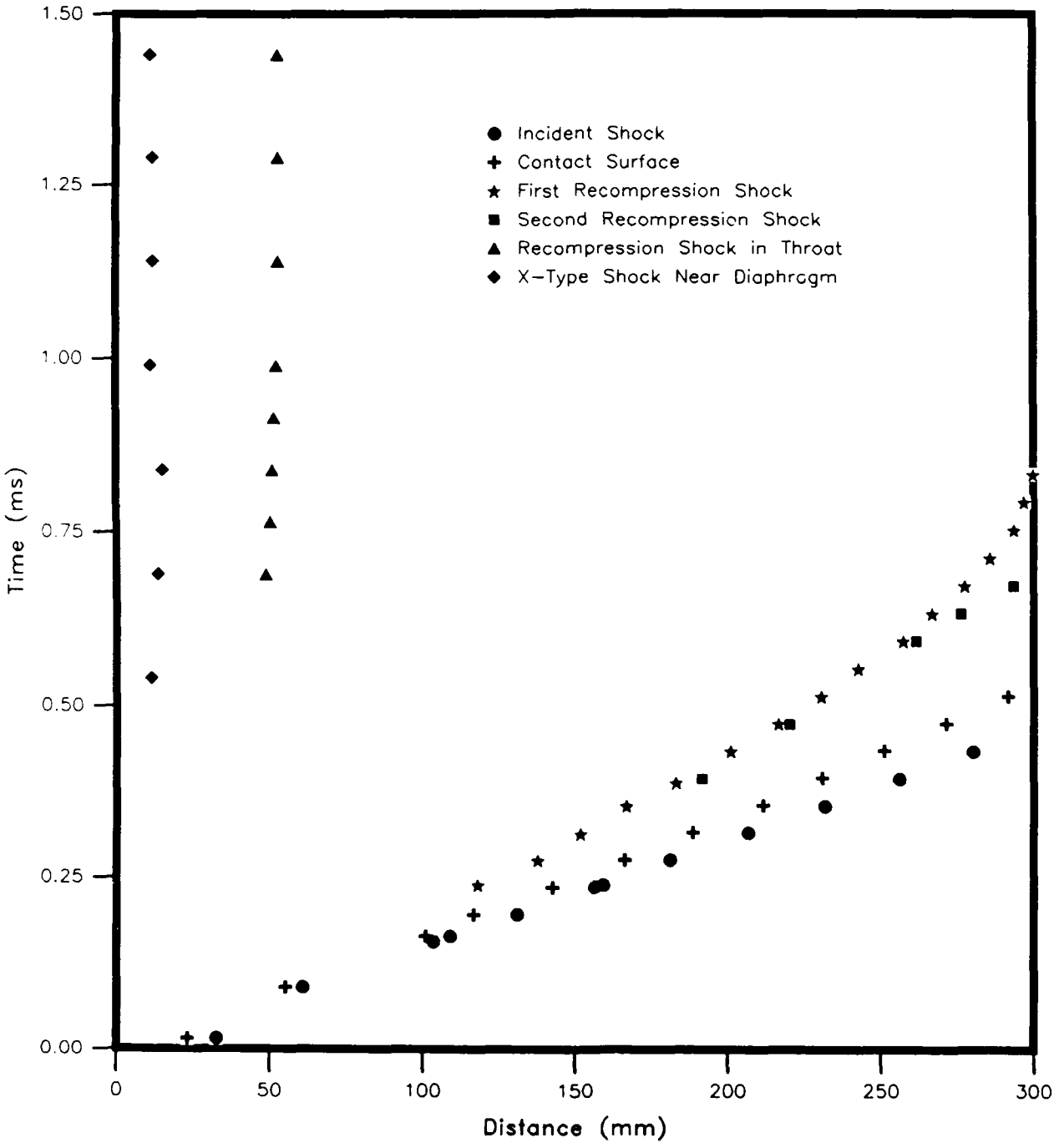

90° Nozzle

Driver Pressure Ratio 4

Shot No. 13249 & 13254 (0–200mm)

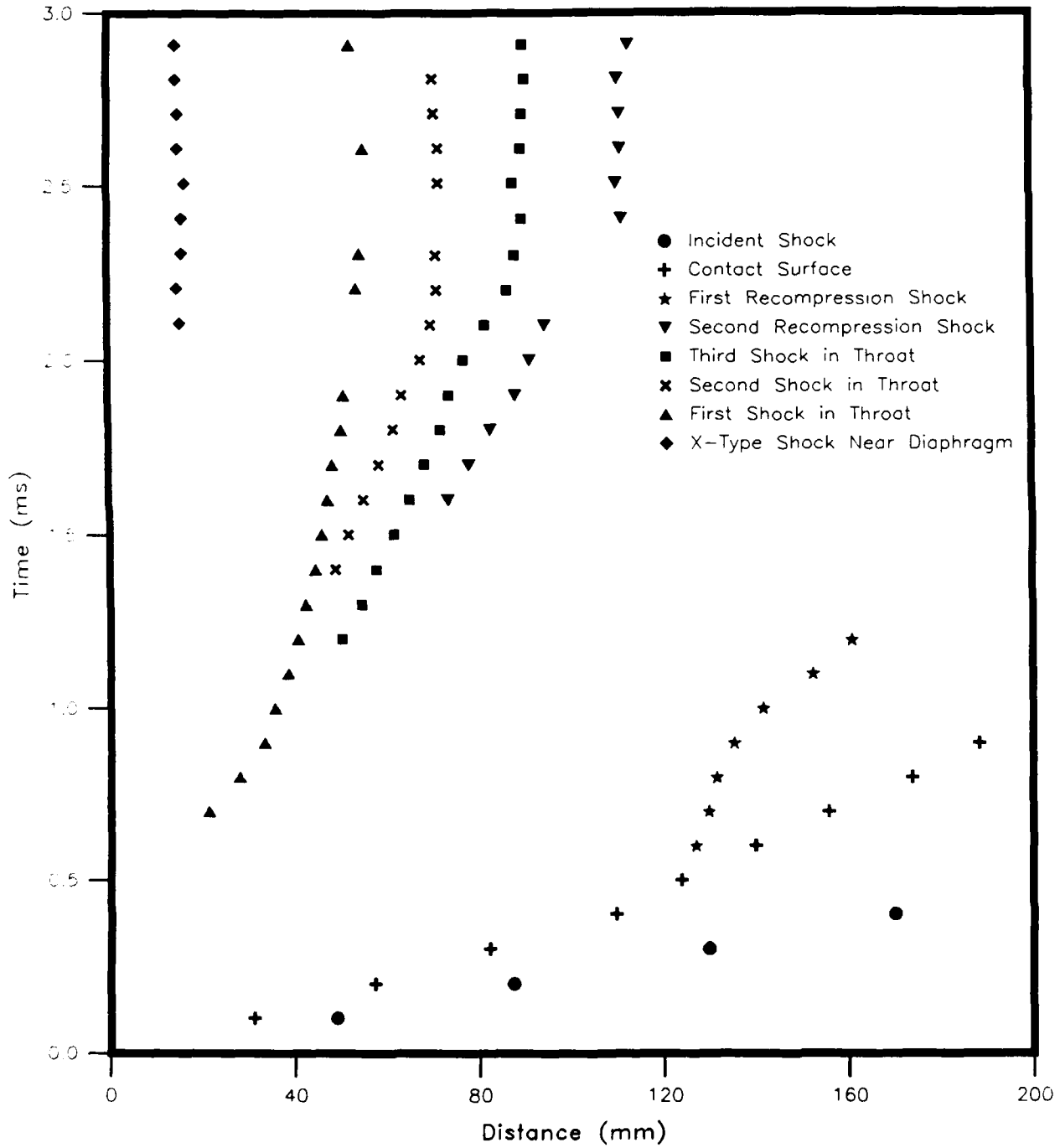

90° Nozzle

Driver Pressure Ratio 14

Shot No. 13258 (0–200mm)

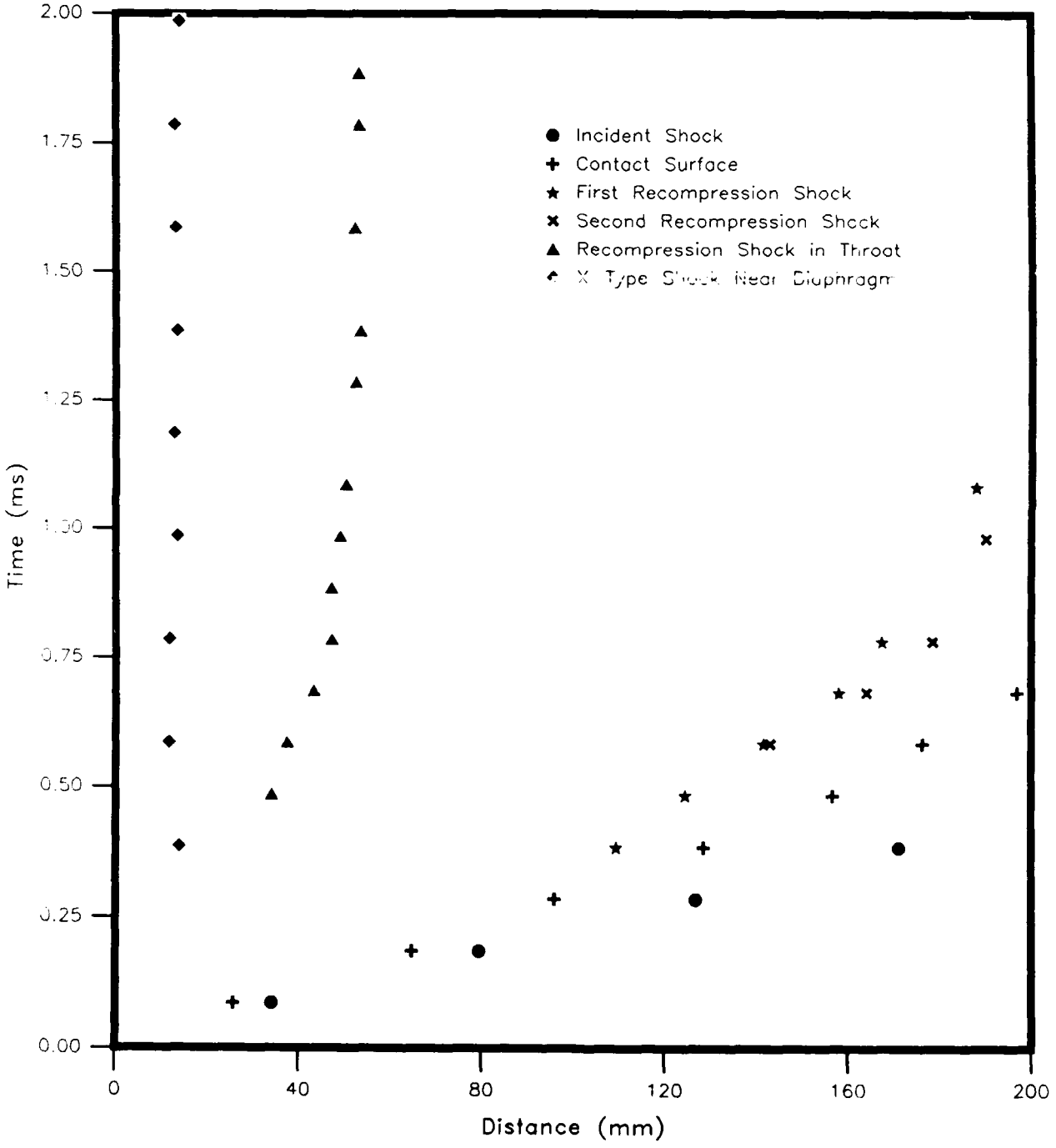

90° Nozzle

Driver Pressure Ratio 38

Shot No. 13310 (0–200mm)

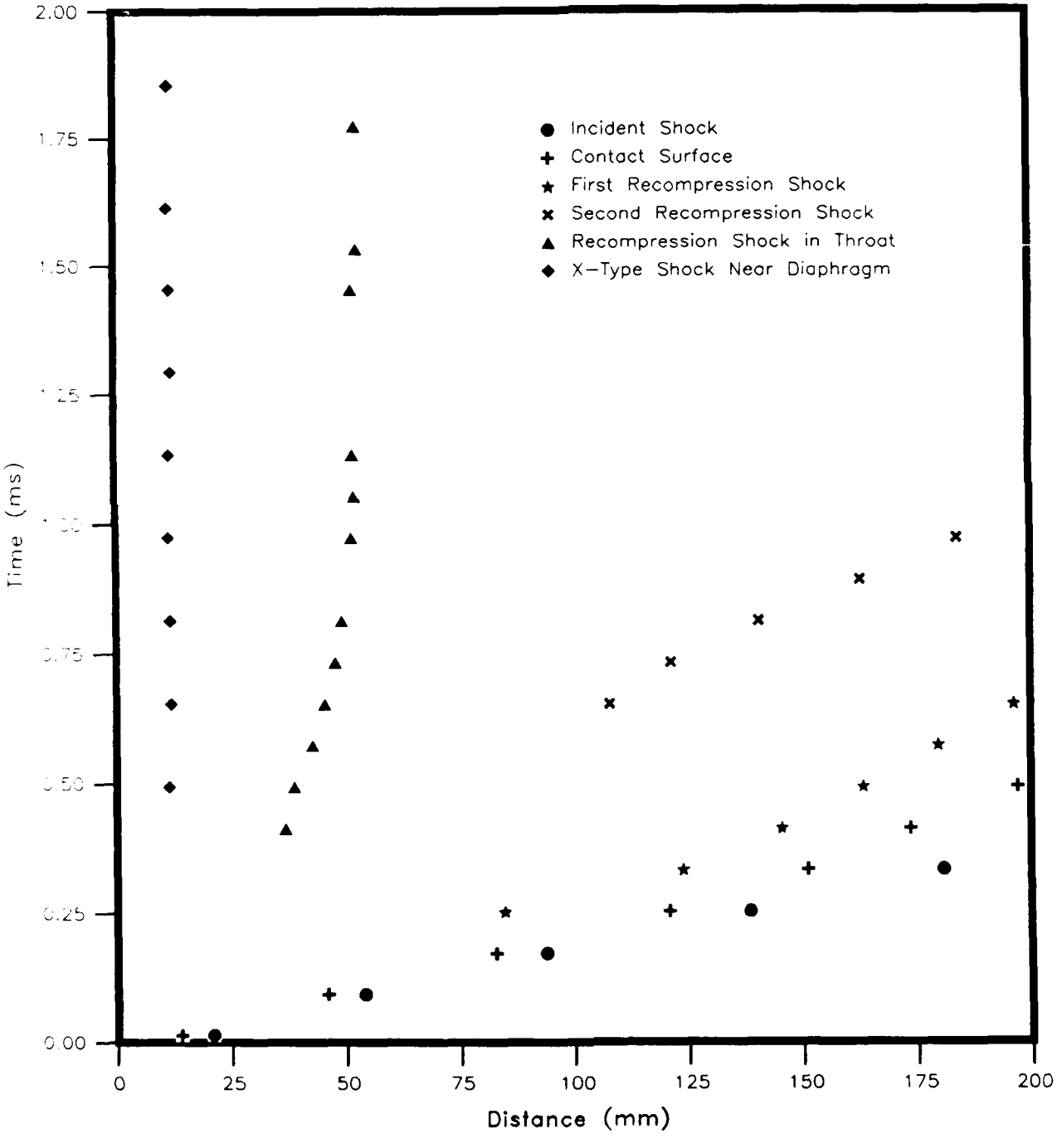

90° Nozzle

Driver Pressure Ratio 55

Shot No. 13301 (0–200mm)

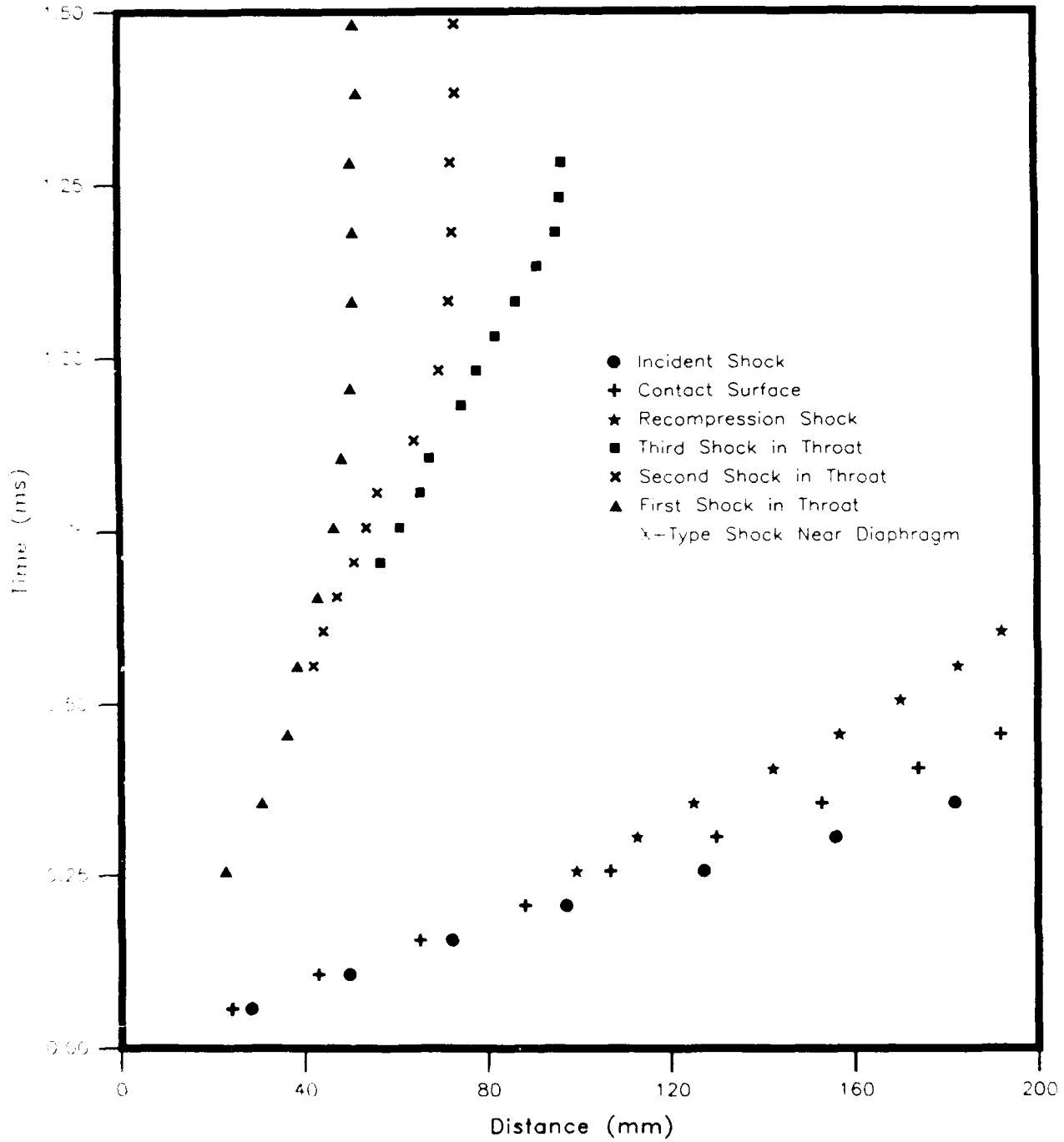

90° Nozzle

Driver Pressure Ratio 80

Shot No. 13311 (0-200mm)

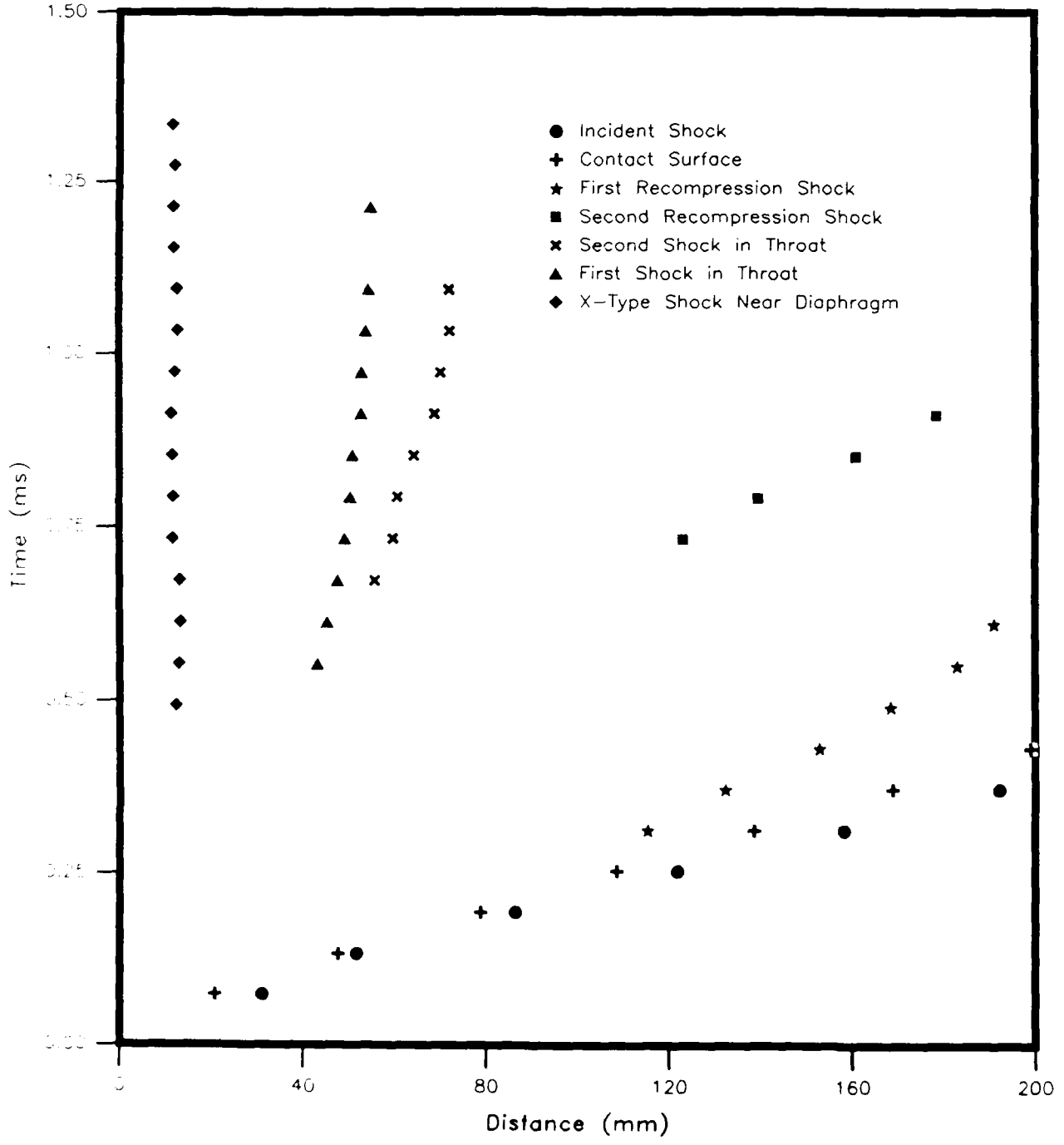

90° Nozzle

Driver Pressure Ratio 110

Shot No.13314 (0-200mm)

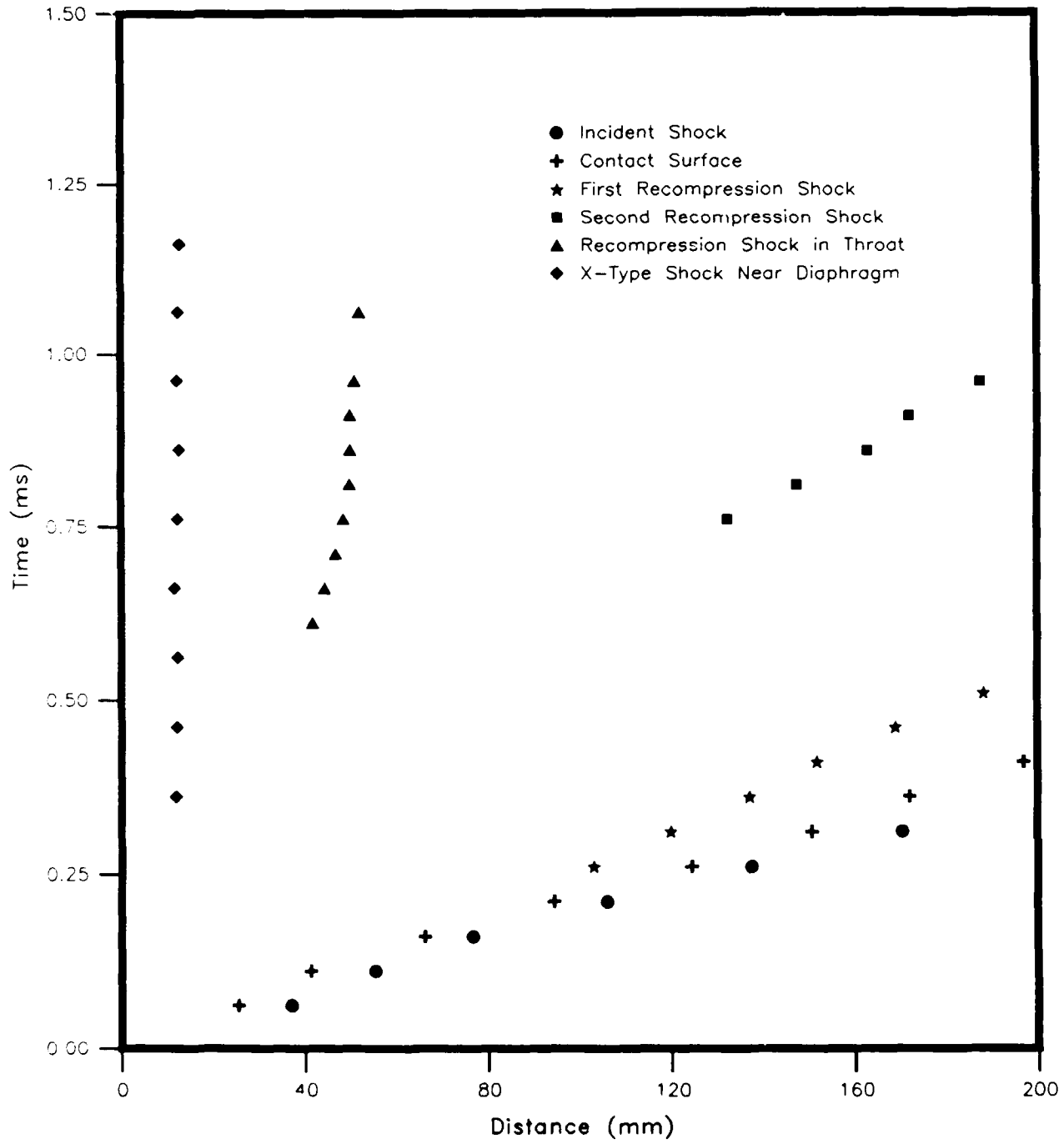

90° Nozzle

Driver Pressure Ratio 188

Shot No.13312 & 13313 (0–200mm)

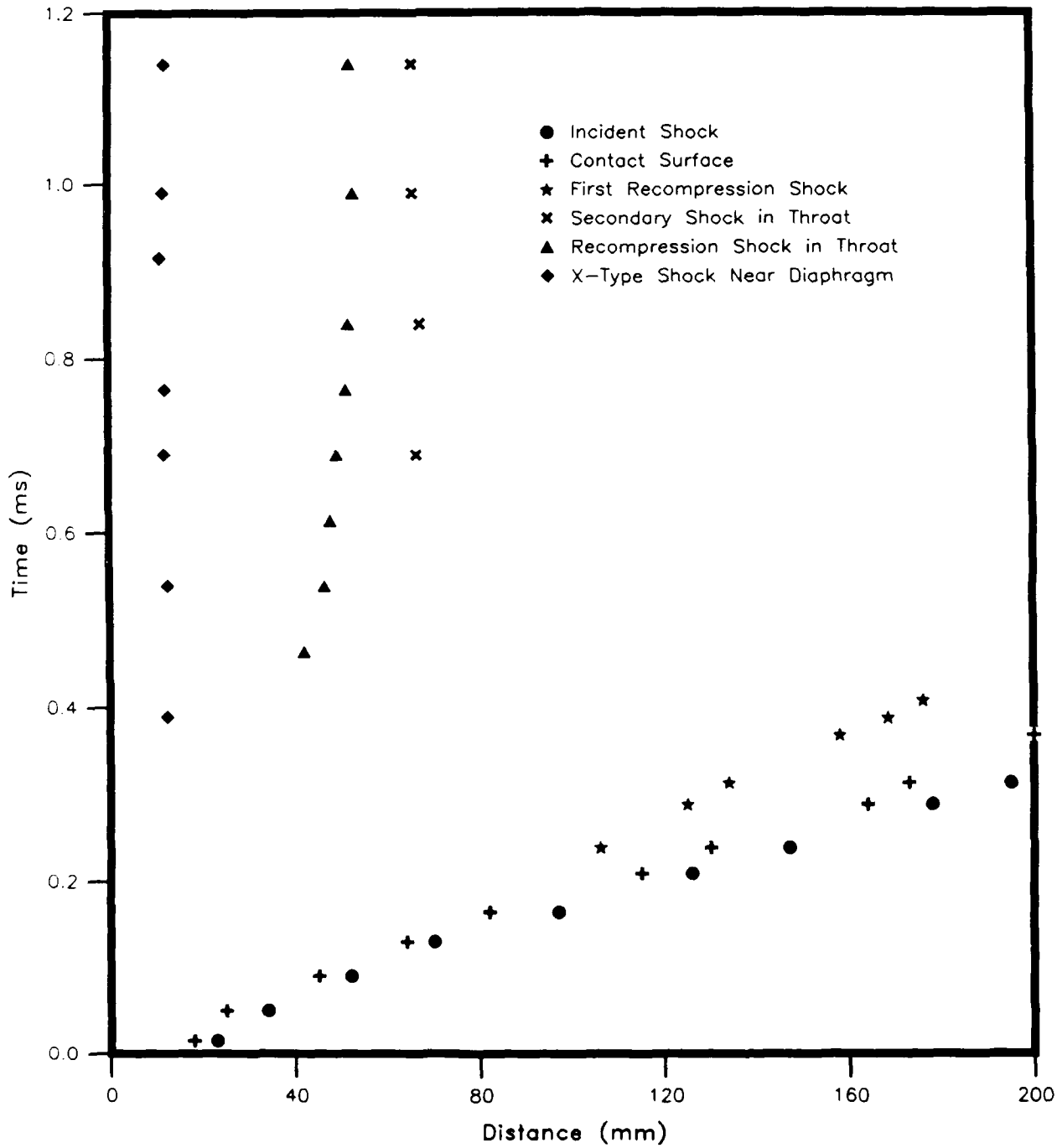

90° & 6° Nozzles

Driver Pressure Ratio 38

Shot No. 13310 (0–200mm) Shot No.13327 (300–500mm)

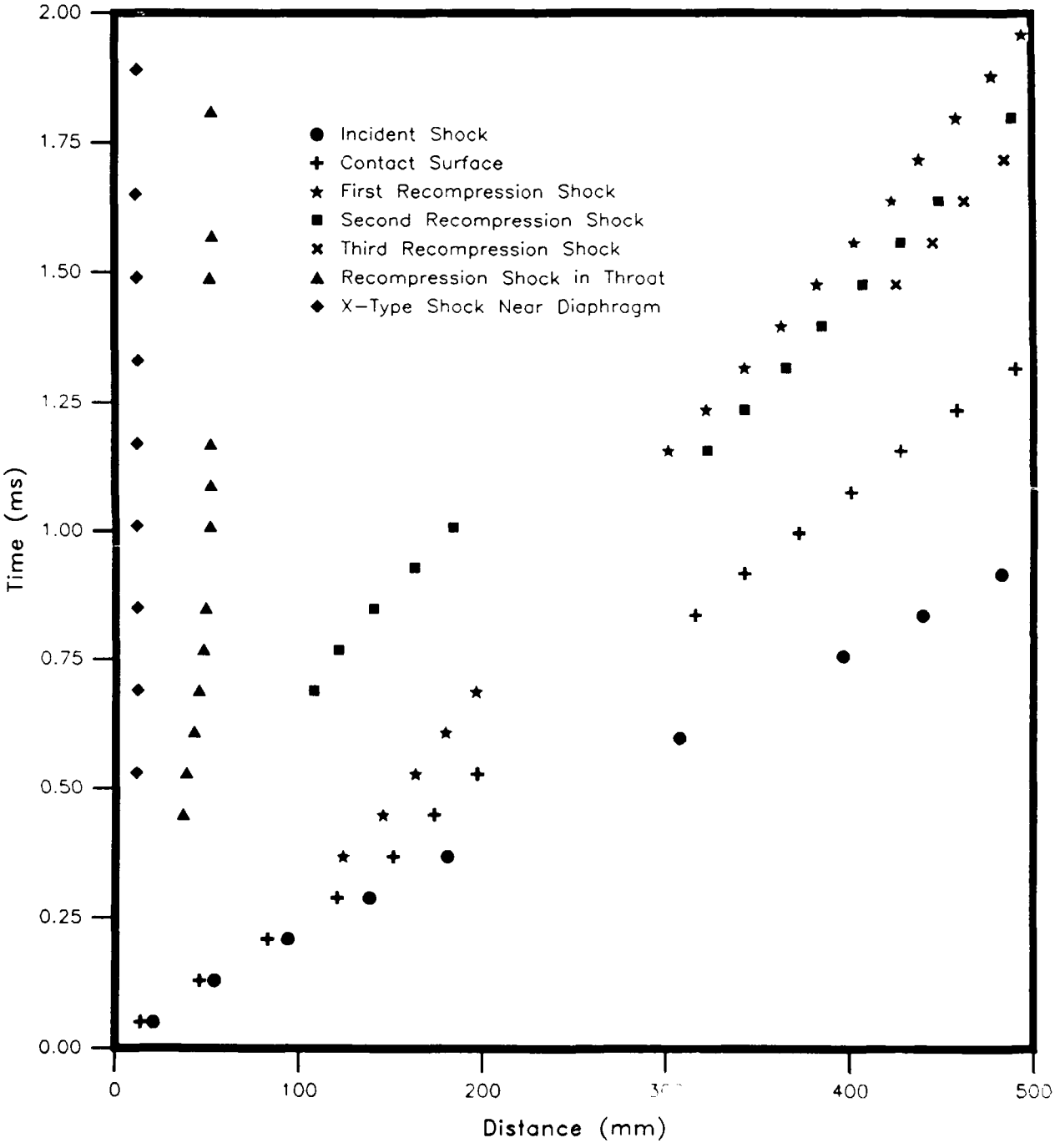

90° & 6° Nozzles

Driver Pressure Ratio 55

Shot No. 13301/02 (0–200mm) Shot No.13328 (300–500mm)

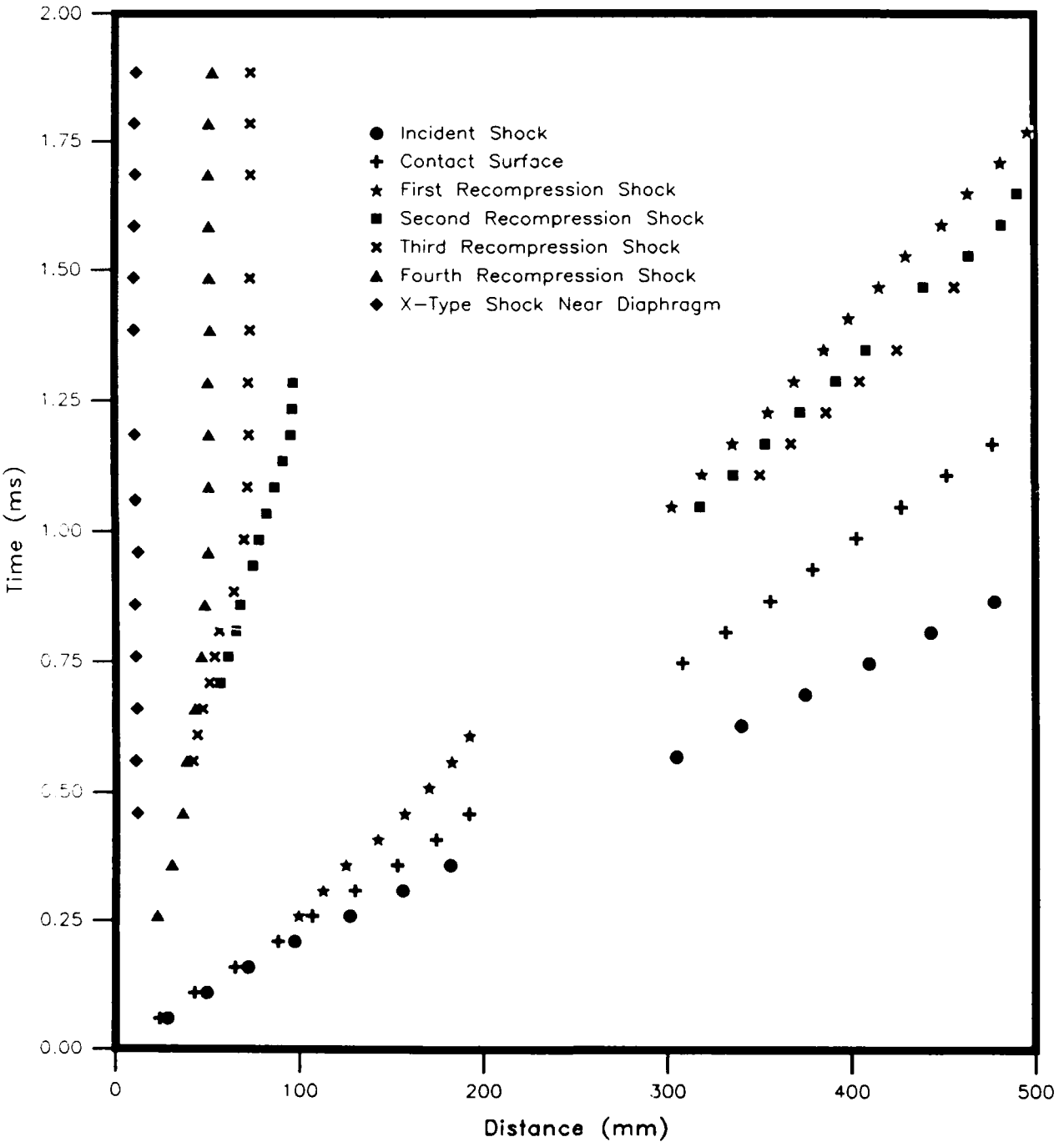

90° & 6° Nozzles

Driver Pressure Ratio 80

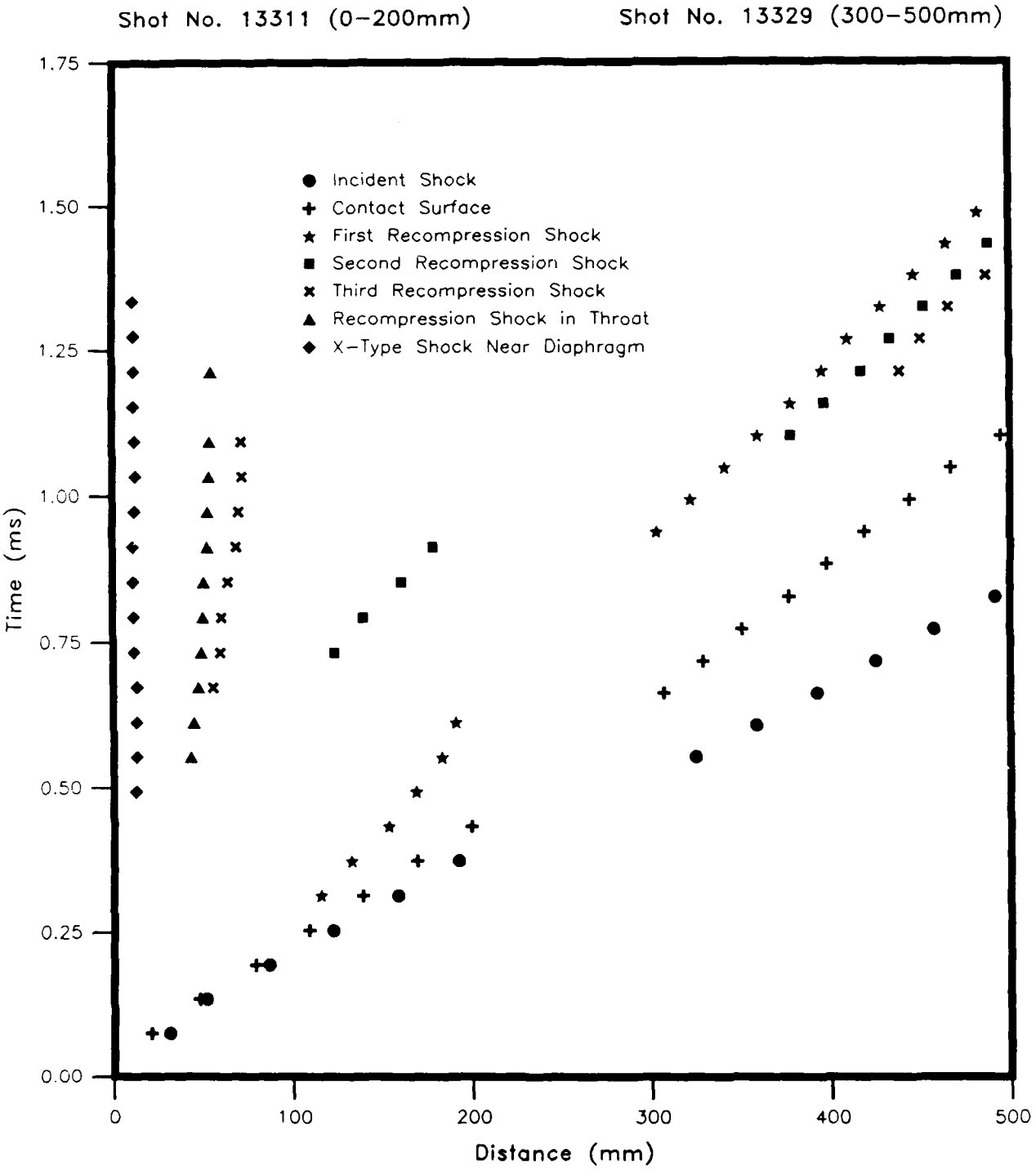

90° & 6° Nozzles

Driver Pressure Ratio 110

Shot No.13314 (0–200mm) Shot No.13330 (300–500mm)

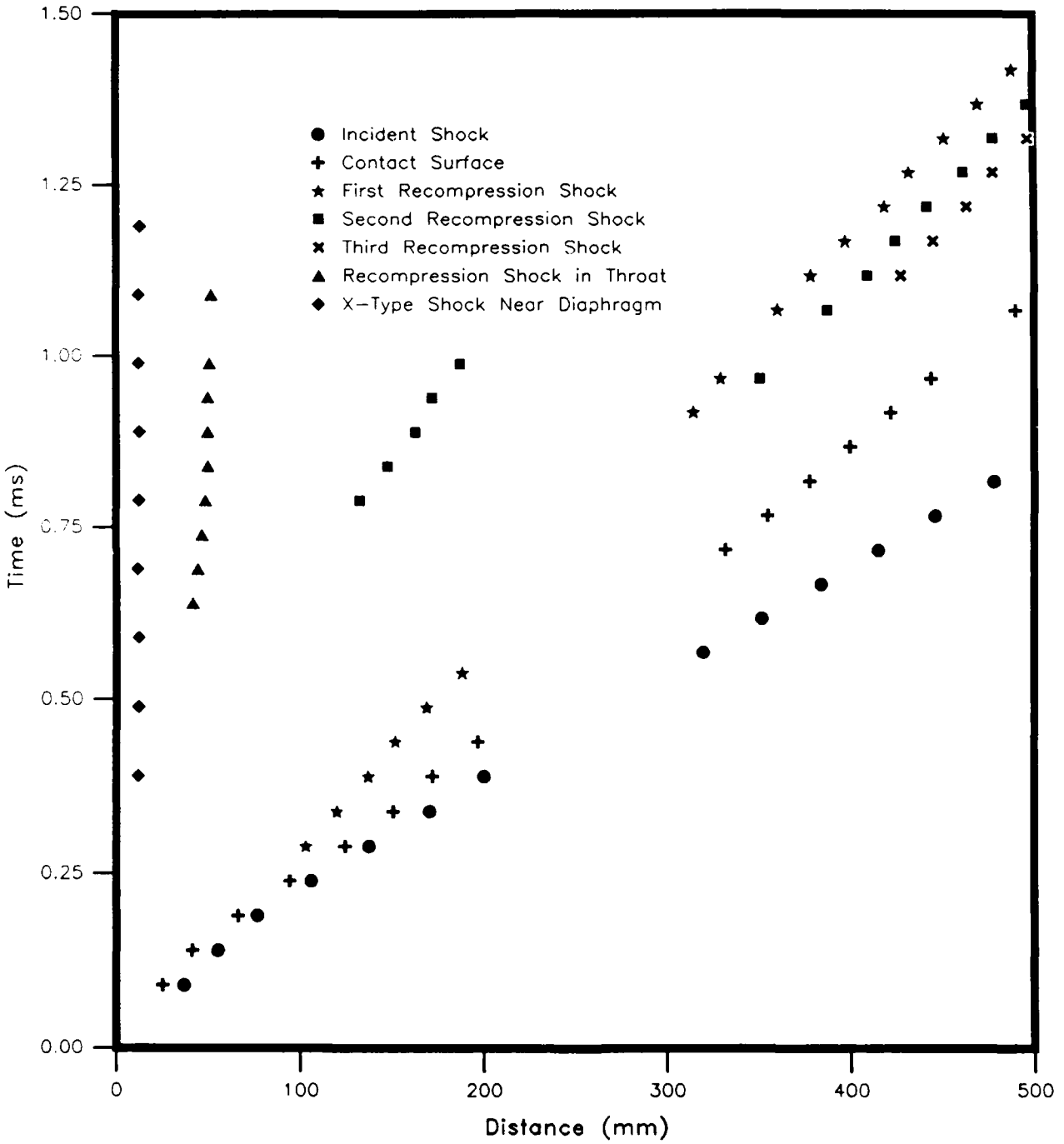

90° & 6° Nozzles

Driver Pressure Ratio 188